DEVELOPMENT AND QUANTIFICATION OF AN ATLAS-BASED METHOD FOR MODEL-UPDATED IMAGE-GUIDED NEUROSURGERY

By

Prashanth Dumpuri

Dissertation

Submitted to the Faculty of the

Graduate School of Vanderbilt University

in partial fulfillment of the requirements

for the degree of

DOCTOR OF PHILOSOPHY

in

Biomedical Engineering

December, 2007

Nashville, Tennessee

Approved by:

Benoit M. Dawant

Robert L. Galloway

Michael I. Miga

Robert J. Roselli

Reid C. Thompson

ACKNOWLEDGEMENTS

First and foremost, I would like to thank my advisor and mentor Dr. Michael I. Miga. This work and my Ph.D. career would not have been possible but for his continued support. I would also like to thank him for being patient with my mistakes over the last few years. He continues to be a source of encouragement.

I would also like to thank my other committe members: Dr. Bob Galloway, Dr. Reid Thompson, Dr. Benoit Dawant and Dr. Robert Roselli. I would like to thank Dr. Bob, Dr. Dawant and Dr. Thompson for always keeping their doors open for my questions. I would like to thank Dr. Roselli for agreeing to be a part of my committee at the last minute. I really appreciate all the time, efffort and inputs they have provided me over the course of my research.

Acknowledgements are also due to the operating room staff and nurses at the Vanderbilt University Medical Center for assisting me in data collection.

This work would not have been possible without the help of various members of the SNARL and BML labs (past and present). Many of them have been the sounding board for my ideas over the past few years. I would like to thank them for their help and friendship. I would also like to thank my friends outside school.

I would like to thank my family for supporting my decision to go to graduate school. I would not be here but for their past and continuing support.

Last but not the least, I would like to thank my brother and sister for their undying love and support. I would like to thank them for being there and for comforting me in times of need. I'm forever indebted to you guys.

TABLE OF CONTENTS

LIST OF TABLES

LIST OF FIGURES

CHAPTER I

PURPOSE AND SPECIFIC AIMS

In the past several years, the importance of knowing intraoperative brain shift during image-guided neurosurgical procedures has been well documented. Also known as post-imaging brain distortion or brain deformation, the shift can be caused by a variety of factors such as surgical manipulation, gravitational forces, clinical presentation of the patient, pharmacological responses etc. Systematic studies have demonstrated that the fidelity of image-guided systems can be seriously compromised by brain deformations if left unchecked. To correct for this deformation, various imaging techniques such as computed tomography (CT), magnetic resonance (MR) imaging, ultrasound(US) have been used for intraoperative image-guided neurosurgery. While CT and MR procedures are cumbersome and have been questioned for their cost-effectiveness, US lacks the image clarity that CT and MR scans produce.

As a cost-effective and efficient method, computational modeling is a procedure that can translate complex surgical events into accurate estimates of tissue response and thereby compensate for intraoperative brain shift. This method provides the umbrella under which the goals of this dissertation are outlined. *The hypothesis is to create a computational framework to update preoperative images using an atlas-based method and sparse intraoperative data.*[1] Specifically, the goals of this research proposal involve: removing the uncertainities posed by the existing computational model with the aid of an atlas-based method, decreasing the computational cost and time associated with the model-updating framework; and enhancing the existing computational model by more accurately capturing the mechanics of brain deformation. These hypotheses will be tested by the following specific aims:

Specific Aim 1. *Predict intraoperative brain shift using an atlas-based method.*

- Develop an algorithm to predict the brain shift from displacement data sets gen-

[1]Sparse data in this context, is defined as data with limited intraoperative deformation or extent.

erated by a computational model and measured sparse data.

- Verify the robustness and accuracy of the algorithm in phantom, simulation and *i*n-vivo studies.

Specific Aim 2. *Demonstrate that the atlas-based computational framework meets the real-time constraints of neurosurgery.*

- Develop a parallel algorithm for the existing computational model.
- Decrease the computational cost associated with the intraoperative component of the algorithm developed for Specific Aim 1.
- Verify the robustness and accuracy of the optimized computational framework in phantom, simulation and *i*n-vivo studies.

CHAPTER II

BACKGROUND

Ever since its advent, medical imaging has played a significant role in surgical planning and treatment because it provides valuable information about anatomical structures and function. This has been particuraly helpful for neurosurgical procedures where, the neurosurgeon has to remove tumor without damaging the healthy brain tissue surrounding it. In order to take advantage of image guidance during a neurosurgical procedure (also known as image-guided neurosurgery, IGNS), preoperative tomograms of the patient must be registered to the patient's anatomy in physical space. While image-to-patient rigid alignment is relatively straight-forward, recent clinical studies in IGNS have exposed limitations to this approach. The work presented in this dissertation attempts to compensate for the inaccuracies presented by IGNS.

A brief introduction to image-guided surgery and image-guided neurosurgery

[1] Image-guided surgery can be defined as the quantitative use of preoperative images during surgery, or in other words using the spatial parameters of the preoperative images during surgery to provide guidance to the surgeon[3]. The basis of any image-guided procedure is the establishment of a reference coordinate system common to both the diagnostic information provided by the images (*image-space*) and the patient's space (*surgical-space*). This process of establishing a transformational relationship between two three-dimensional spaces is known as *registration*. Initial attempts at determining a quantitative registration were provided using stereotactic frames for surgical guidance and a detailed review of stereotaxy can be found in [4, 5]. A common theme in the classic stereotaxy designs was the flow of information from image-space to physical-space.

The advent of advanced imaging-modalities such as computed tomography (CT) and

[1] It should be noted here that image-guided surgery has been discussed in the context of neurosurgery

magnetic resonance (MR) imaging brought about a shift in the direction of information flow, giving birth to frameless stereotaxy or interactive-image guided neurosurgery. A reversal from classic strereotaxy, these methods were based on the principle of tracking the surgical position in physical space and displaying the position in image-space. A detailed review of the process and development of image-guided procedures can be found in [3].

Roberts et al. [6] were the first[2] to design a frameless-streotactic system. In that system, an operating microscope was retrofitted with an acoustical localization system and information from the system was used to provide feedback to the surgeon. Roberts et al. reported a registration error as low as 0.8mm in a patient and an error of 2mm or less in phantom studies. Ever since, other frameless stereotactic systems have been developed based on alternative localization systems such as optical and magnetic localization systems. It is beyond the scope of this dissertation to discuss all the frameless stereotactic systems that have been developed for neurosurgery. Current *state-of-the-art* IGNS systems use either optical or magnetic localizers, a rigid-registration between physical- and image-space and a combination 2D/3D computer graphics for feedback.

Brain shift and current IGNS systems

As stated before, IGNS systems require that the image-space be registered to physical-space. While image-to-patient rigid alignment is relatively straight-forward, recent clinical studies in IGNS have exposed limitations to this approach. Systematic studies discussed in detail below, have reported that the brain is capable of deforming during surgery for a variety of reasons, including pharmacologic responses, gravity, edema, surgical manipulation and respiration[7, 8, 9] and that the brain can shift a centimeter or more in a non-rigid fashion [10].

[2]the first system that was reported in press

Quantification of Brain shift

Nauta [11] was one of the first to quantify brain shift during neurosurgery using "frameless" stereotaxy. Using two stereotactic localization systems (CRW frame and ISG wand) and intraoperative CT scans, Nauta quantified the brain shift to be approximately 5mm in a 43 yr old man undergoing tumor resection therapy and demonstrated in three other cases the advantages of intraoperative image-guided surgery in (i) assessing the completeness of a cyst aspiration (ii) confirming the site of tumor biopsy and (iii) to guide a biopsy needle in physical space using updated introperative images.

Hill et al. in a preliminary report in 1997 [12], reported a median shift from 0.3mm to 7.4mm in 5 patients using the ACUSTAR I surgical navigation system. In a follow-up and more detailed study, Hill et al. [13] measured the deformation of the dura and the brain surfaces between the time of imaging and the start of surgical resection in 21 patients using the same ACUSTAR I navigation system. They reported a mean displacement of 5.6mm with a mean volume reduction of 29cc. A finding common to Hill et al. and Nauta is that gross brain shift mainly occurs in the direction of gravity.

Maurer et al. [14] were among the first to investigate the effects of intraoperative brain shift using an intraoperative MR (iMR) scanner. Though mostly qualitative, they also presented preliminary results obtained using a non-rigid registration algorithm to quantify deformation. Maurer et al. suggest that the shift can be caused by hyperosmotic drugs that reverse the blood-brain barrier and alter the cerebro-spinal fluid (CSF) volume.

Hartkens et al. [10] extended the work presented by Maurer et al. and quantified the brain shift retrospectively using a deformable volumetric image registration algorithm. Contrary to the earlier findings Hartkens et al. suggest that the principal direction of displacement does not always correspond with the direction of gravity.

Dorward et al. [15] reported a prospective study conducted in 48 patients using iMR to quantify brain shifts during surgery and to determine correlations between the shifts and the patient characteristics. For all 48 cases, Dorward et al. quantified shift for points on the

brain surface and for deep tissue points. Dorward's results of deep tissue shift complement the findings of Hartkens et al. who also reported shift at deeper brain structures. However unlike Hartkens et al., Dorward et al. suggest that the shift can be caused by a variety of factors including gravity and patient positioning in the operating room (OR). Dorward et al. also correlate the observed shift to patient characteristics such as the presence of edema, lesion volume, distance of the lesion below the skin surface and the nature of the tumor.

Bucholz et al. were one of the first to measure brain shift using intraoperative ultrasound (iUS) [16] An optically tracked and calibrated ultrasound probe was used to capture cross-sectional images of the brain and corresponding features in serial ultrasound images, such as the depths of sulci, were measured to quantify shift. Bucholz et al. also demonstrated an increasing trend in shift over the duration of surgery, similar to the findings of Dorward's and Hill et al..

Roberts et al. [7] used a tracked surgical microscope to localize points on the surface of brain during surgery in 28 patients. For three dimensional shift measurements, a laser focus system was used to localize surface points during the course of surgery. The results of both 3D and 2D measurements suggested that the largest direction of shift was parallel to the gravitational vector. Roberts et al. hypothesized that the inadvertent loss of CSF fluid casued the brain to sag/sink in the direction of gravity. The time-course analysis of shift reported by Roberts et al. supported the findings of Hill and Dorward et al. by demonstrating increasing shift over the duration of surgery.

The results of these papers indicate brain shift can be caused by a variety of factors such as patient positioning in the OR, gravitational forces acting on the brain surface, drainage of CSF during surgery, hyperosmotic drugs such as mannitol, elevated intracranial pressure in the edema. Although the individual measurements of brain shift vary from paper to paper, the general trend is that the surface shift is on the order of centimeters and deep tissue shifts on the order of 5mm with expansive shifts near the resection boundary bulging towards the surgical site. Also, sub-surface structures such as the lateral ventricles have been known to collapse due to brain shift. Furthermore, the shift phenomena is time dependent

and the gravitational sag generally increases over the course of surgery with the rate of increase tapering towards the end of surgery. The specific methods of each paper suggest that the solution to the brain shift problem will not have generic properties, as the underlying phenomena are quite intricate and patient-specific.

Intraoperative brain shift compensation methods

The previous section demonstrated the need for brain shift correction and as a result of these findings, current research has been focussed towards providing a more accurate representation of the brain during surgery. Patrick Kelly was one of the first to describe a qualitative compensation for neurosurgery [17]. Kelly placed 1mm stainless steel balls, 5 millimeters apart, along the surgeon's viewing axis of the craniotomy and would then acquire projective images normal to the viewing axes during surgery. Any positional shifts of the balls seen in the projection images was attributed to brain shift and was accounted for. In 1991, Hassenbusch et al.. demonstrated a marker based method to account for brain shift and to assist in tumor resection[18]. Hassenbush et al. used surgical micropatties with string tails tethered to them and these micropatties were placed under stereotactical guidance around the tumor margin. Gross tumor edges were determined from positions of actual patties or catheter tips. The following sections describe more "automatic" methods currently under heavy investigation as possible strategies for brain shift compensation. These automatic shift compensation methods can be split into two categories: intraoperative imaging and computational methods. Each method has its own advantages and disadvantages and they are presented in detail below.

Intraoperative Imaging-based shift compensation methods

Shalit et al. [19] was probably the first to demonstrate the benefits of having updated images during neurosurgery. Shalit et al. used an intraoperative CT scanner to locate the tumor margins during surgery and to assess the extent of brain tumor resection intraoperatively. Though they do not state it explicitly, using an intraoperative CT scanner helped

account for brain shift. This work is significant because brain shift was not even recognised as a source of error in IGNS at that time.

Dade Lunsford an important contributor in the field of intraoperative CT (iCT) helped in the development of a clinical OR around the CT scanner and also developed CT compatible stereotactic frames [20, 21, 22]. In a more recent article [23], they reported the findings of a 4000 patient study over a 20-year interval using iCT. A limitation of Lunsford's protocol was that the surgeon was required to perform surgery on the CT gantry.

Noting the limitations of Lunsford et al.'s system and the excessive labor involved in iCT Okedura et al. [24] developed an iCT system with (i) a mobile gantry based CT scanner and (ii) head fixation devices to assist in the head positioning during surgery. Even with the remarkable advancements made by Okudera, Lunsford, and Shalit , a common limitation in all of the iCT systems is the dedication of an entire OR suite to the intraoperative imaging system.

Butler et al. [25] circumvented this problem by developing a mobile CT scanner in which the scan plane is selected by means of gantry translation rathen than by translation of the patient table. This adapation made it possible for the CT scanner to be wheeled into the OR when needed and made it possible for the scanner to be used across multiple operating rooms.

Despite all the advantages, general adoption of iCT as a method to correct for brain shift has not occurred probably due to dose considerations, both to the patient and the OR staff related to repeated exposure to X-ray radiation.

Over the past decade, industry and neurosurgeons have also attempted to extend surgical visualization again by bringing MRI into the operating room and many different approaches have been researched to compensate for intraoperative brain shift. The first approach to interventional magnetic resonance imaging (iMR)-guided neurosurgery was developed by Ferenc Jolesz and Peter Black [26, 27]. Subsequently a number of research groups demonstrated the technical and practical solutions needed to implement iMR during neurosurgery [28, 29, 30, 31, 32, 33, 34, 35, 36, 37, 38, 39, 40]. Based on the imaging technique and the MRI

infrastructure, these iMR based shift compenstation methods can be broadly classified into three categories: (i) Category I: the surgical field is within the magnetic field around the magnetic isocenter and the OR must be equipped with "MRI-compatible" surgical equipments thereby limiting the surgeon's options in patient positioning and approach (ii) Category II: neurosurgical procedures are performed in the weak magnetic fringe fields surrounding a open MRI system and (iii) Category III: the surgical space is separated from the imaging-space and the patient is transported to the imaging suite for imaging. Also with the advent of efficient and more accurate image-registration and image-processing algorithms, several research groups have demonstrated that iMR based shift compensation methods meet the real-time constraints of neurosurgery. Though promising, there are still many concerns with iMR such as: field inhomogeneities during scanning and their causes, false-positive readings caused by the leaking contrast agents and bleeding, the logistical requirements of surgery within or near an MR system, and the total cost of operation (TCO) of an iMR system.

In light of the TCO concerns of current iMR systems, intraoperative ultrasound (iUS) has gathered attention as a cheap and safe alternative to both iMR and iCT [41, 42, 43, 44, 45, 46, 47, 48, 49]. However current iUS systems suffer from low signal-to-noise ratio (SNR), limiting their effectiveness in demarcating tumor regions during surgery. iUS based shift compensation methods therefore do not present themselves as a complete intraoperative solution to the brain shift phenomena.

To summarize, the intraoperative imaging based shift compensation methods do not provide quantitative compensation for brain shift by themselves. In light of this fact, Roberts et al. suggested a computational model [50] as a cost-effective and an efficient method to compensate for intraoperative brain shift.

Model-updated Image-guided Neurosurgery (MUIGNS)

To compensate for intraoperative brain shift, MUIGNS systems use a computational model that can translate complex surgical events into accurate estimates of tissue response.

A schematic of MUIGNS is shown in Figure 1

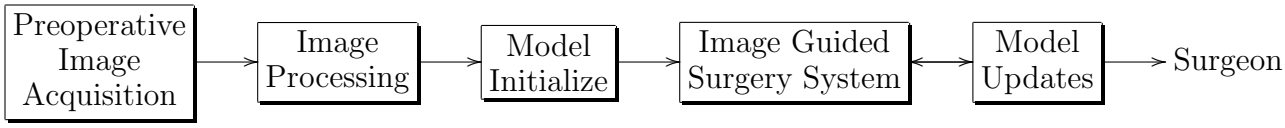

Figure 1: Schematic for model updated image guided neurosurgical procedures (MUIGNS).

A spectrum of computational models ranging from less physically plausible but very fast models through to extremely accurate biomechanical models requiring hours of compute time to solve have been presented in the literature [51, 52, 53, 54, 55, 56, 57].

Bro-Nielsen reported a fast surgery simulation method in [58] built using finite-element models for linear elastic materials. The reported method achieved speed by converting a volumetric finite-element model into a model with only surface nodes, i.e., nodes that are visible during surgery. This work had the goal of achieving interactive graphics speeds at the cost of accuracy of the simulation and is therefore applicable for computer graphics oriented visualization tasks and not during neurosurgical interventions where the focus is robustness and high accuracy.

Edwards et al. reported a two-dimensional three-component model [55, 59] to predict intraoperative deformation. This work used a simplified material model: $Min.(E_{total} - (E_{model} + \alpha E_{sample}) = 0)$ with the goal of achieving higher speed. E_{model} represented the total energy associated with the deformation and the edge strength measure, E_{sample} acted as a smoothing constraint. Their goal was not to model the physics of brain tissue deformation, but to interpolate across soft tissues incorporating constraints such as the rigidity of skull and fluidity of CSF. The initial multigrid implementation on 2D images of 128x128 pixels converged to a solution in 120-180 minutes when run on a Sun Microsystems Sparc 20. Though this model was patient specific and extracted from preoperative scans, it was a two-dimensional model and it did not capture the physics of soft tissue deformation. In other words, this model is not based on continuum mechanics and does not conserve the volume of the deformed brain.

Skrinjar et al.. [60, 61] presented a model for real-time intraoperative brain shift capture. Skrinjar et al. used the model for epilepsy neurosurgery where brain shift is rather slow.

Brain surface points were tracked to indicate surface displacement and to validate the model predictions. They used a simplified homogeneous brain tissue material model - a Kelvin solid model since "it is a rather simple approach, which is a desirable property since the model deformation should be computed in real time" since it must be utilized during the surgery. In [60], on a Hewlett Packard 9000 (C110) machine they reported a solve time of approximately 10 minutes for the Kelvin model. They also reported a computational time of 4 hours for a 2D numerical model (with 176 brain nodes, 57 skull nodes and 496 connections) and a 3D model (with 1093 nodes and 4855 connections) respectively. In [61] their numerical model had 2088 nodes, 11733 connections and 1521 brick elements, and required "typically less than 10 minutes" on an SGI Octane R10000 workstation with one 250MHz processor. Based on these findings they concluded that "this model can potentially be used during the surgery". Though a modest improvement over the Edwards et al. model, this model had the same drawback that it did not capture the physics of brain deformation during surgery.

Warfield et al. [40], presented a finite-element model for real-time intraoperative brain shift capture. Warfield et al. treated the brain as a homogeneous linear elastic material and established the boundary conditions via surface matching of the intraoperative and the preoperative MR tomograms. A brief description of the linear elastic model is given below.

The stress state at point P can be represented by an *infinitesimal* cube with three stress components on each of its six sides (one normal and two shear components).

Since each point in the body is under static equilibrium (no net force in the absence of any body forces or external forces), applying Newton's second law of motion results in the following equation:

$$\nabla \cdot \sigma = 0 \tag{1}$$

In linear elasticity, the deformation is proportional to the applied load and is more widely known as the Hooke's law of elasticity. The relationship between stress and strain for a linear

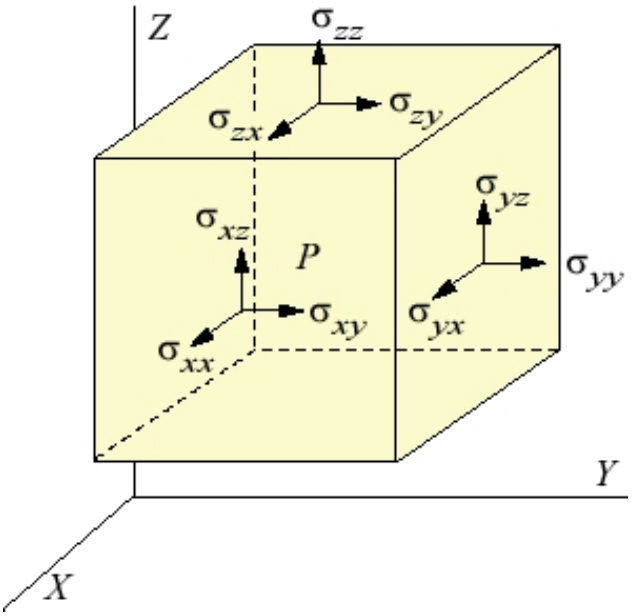

Figure 2: Stresses acting on a 3D solid.

elastic isotropic [3]material is given by

$$\begin{Bmatrix} \epsilon_{xx} \\ \epsilon_{yy} \\ \epsilon_{zz} \\ \epsilon_{xy} \\ \epsilon_{yz} \\ \epsilon_{xz} \end{Bmatrix} = \begin{Bmatrix} \frac{\sigma_{xx}}{E} - \frac{\nu}{E}(\sigma_{yy} + \sigma_{zz}) \\ \frac{\sigma_{yy}}{E} - \frac{\nu}{E}(\sigma_{xx} + \sigma_{zz}) \\ \frac{\sigma_{zz}}{E} - \frac{\nu}{E}(\sigma_{xx} + \sigma_{yy}) \\ \frac{\sigma_{xy}}{2G} \\ \frac{\sigma_{yz}}{2G} \\ \frac{\sigma_{xz}}{2G} \end{Bmatrix} \tag{2}$$

where "E" is the Young's Modulus, ν the Poisson's ratio, "G" the shear modulus, ϵ_{ij} the strains and σ_{ij} the stresses. σ_{ij} and ϵ_{ij} are second order tensors wherein the first subscript refers to the direction of the surface normal on which the stress/strain is acting and the second subscript refers to the direction of the stress/strain component and i,j = x,y,z the 3 Cartesian axes. The shear modulus "G" is related to the Youngs's modulus "E" by $G = \frac{E}{2(1+\nu)}$ thereby indicating that the material can be defined by two elastic constants, i.e., the Young's modulus and the Poisson's ratio. It should be noted that the shear stresses and the shear

[3]Isotropy: material properties are independent of direction

strains across the diagonal are identical (i.e., $\sigma_{xy} = \sigma_{yx}$). In [40] Warfield et al. used the small deformation theory [4] to relate the strains to the displacement along the cartesian axes x,y,z wherein the strain components are defined as

$$\begin{Bmatrix} \epsilon_{xx} \\ \epsilon_{yy} \\ \epsilon_{zz} \\ \epsilon_{xy} \\ \epsilon_{yz} \\ \epsilon_{xz} \end{Bmatrix} = \begin{Bmatrix} \frac{\partial \vec{u}}{\partial x} \\ \frac{\partial \vec{v}}{\partial y} \\ \frac{\partial \vec{w}}{\partial z} \\ \frac{1}{2}(\frac{\partial \vec{u}}{\partial y} + \frac{\partial \vec{v}}{\partial x}) \\ \frac{1}{2}(\frac{\partial \vec{v}}{\partial z} + \frac{\partial \vec{w}}{\partial y}) \\ \frac{1}{2}(\frac{\partial \vec{u}}{\partial z} + \frac{\partial \vec{w}}{\partial x}) \end{Bmatrix} \tag{3}$$

where $\vec{u}$, $\vec{v}$ and $\vec{w}$ are the displacement vectors along the three cartesian axes.

Using Equations 3 and 2, Equation 1 transforms to

$$\nabla \cdot G\nabla\vec{u} + \nabla\frac{G}{1-2\nu}(\nabla \cdot \vec{u}) = 0 \tag{4}$$

Warfield et al. solved the above equation using the finite-element method. Using a Sun Microsystems Sun Fire 6800 with 12 750MHz UltraSPARC-III CPUs, for a 43584 node, 214035 element mesh with three DOF at each node, Warfield et al. reported a run time of 15 seconds.

In [62], the same group extended the linear elastic finite element model by allowing for inhomogeneity and anisotropy in the material properties according to the diffusion tensor data. Diffusion Tensor MRI (DT-MRI) is a technique that allows for non-invasive quantification of diffusion of water *in* vivo. The directional dependence of water diffusion rates can be closely related to the anisotropy of the structure. Therefore, DT-MRI can be used to infer the anisotropic material properties. In [62], Kemper treated the brain as a special case of the tranversely orthotropic material [5]. Similar to Equation 2, Hooke's law for a tranversely

[4] Simply put, small deformation theory assumes that the strains are "small" for both normal and shear strain.

[5] Transversely isotropic materials are those that have the same properties in one plane (e.g. the x-y plane) and different properties in the direction normal to this plane (e.g. the z-axis).

isotropic material with isotropy/symmetry in the x-y plane and anisotropy in the z-plane can be written as:

$$\begin{Bmatrix} \epsilon_{xx} \\ \epsilon_{yy} \\ \epsilon_{zz} \\ \epsilon_{xy} \\ \epsilon_{yz} \\ \epsilon_{xz} \end{Bmatrix} = \begin{Bmatrix} \frac{\sigma_{xx}}{E_p} - (\frac{\sigma_{yy}\nu_p}{E_p} + \frac{\sigma_{zz}\nu_{zp}}{E_z}) \\ \frac{\sigma_{yy}}{E_p} - (\frac{\sigma_{xx}\nu_p}{E_p} + \frac{\sigma_{zz}\nu_{zp}}{E_z}) \\ \frac{\sigma_{zz}}{E_z} - (\frac{\sigma_{xx}\nu_{zp}}{E_p} + \frac{\sigma_{yy}\nu_{zp}}{E_p}) \\ \frac{\sigma_{xy}(1+\nu_p)}{E_p} \\ \frac{\sigma_{yz}}{2G_{zp}} \\ \frac{\sigma_{xz}}{2G_{zp}} \end{Bmatrix} \tag{5}$$

The above equation demonstrates that the transversely isotropic material can be represented by the following 5 elastic constants: Young's modulus and Poisson's ratio in the x-y symmetry plane, E_p and ν_p and the Youngs's modulus, Poisson's ratio and shear modulus in the anisotropic direction/z-direction, E_{zp}, ν_{zp} and G_{zp} respectively. Kemper assumed that $\nu_p = \nu_{zp}, G_{zp} = G_p = \frac{E}{2(1+\nu)}$, thereby reducing the number of constants used to describe the material properties. Using landmarks identified on preoperative and intraoperative MR tomograms, Kemper demonstrated that the difference in displacements predicted by modeling the brain as a linear elastic isotropic and linear elastic anisotropic model was between 1 and 3mm. Though the difference was small, the anisotropic model showed improvement over the isotropic model.

Miller et al. and Wittek et al. modeled the brain as a hyperelastic material [63, 52, 64] undergoing large deformations. Hyperelasticity refers to materials which can experience large elastic strain that is recoverable. Also, hyperelastic materials are often referred to as being incompressible (volume is conserved during deformation). The constitutive behavior of hyperelastic materials are usually derived from the strain energy potentials. Based on the experiments conducted in [65, 63], Miller et al. suggested a constitutive law based on Mooney-Rivlin laws.

$$\mathbf{W} = \frac{2}{\alpha^2} \int_0^t [\mu(t-\tau) \frac{\partial}{\partial \tau} (\lambda_1^\alpha + \lambda_2^\alpha - 3)] \partial \tau \tag{6}$$

where $\mathbf{W}$ is a potential function, $\lambda' s$ the principal stretches, μ the shear modulus, τ the relaxation time and α is a material constant. The Mooney-Rivlin equation was developed by Rivlin and Saunders to describe the deformation of highly elastic bodies which are incompressible (volume is conserved during deformation) and isotropic (the material has the same mechanical properties in all directions at a material point). They formulated the material law as a strain energy function in terms of the first and second principal invariants (quantitative information on the deformation) of the deformation. The formulation is called a strain energy function as the energy is conserved during deformation of these materials under constant temperature. The material constants described in Equation 6 are usually obtained from the load-extension curves that describe the material. Miller et al. conducted *i*n-vitro experiments on porcine brain tissue and reported the values for the material constants in [65, 63]. Using the hyperelastic model described above to capture intraoperative brain shift Wittek et al. in [52] reported shift recaptures of 92.1% at the ventricles and 80% at the tumor region. They also reported a computation time of around 15-16 mins on personal computer with a 2.8 GHz Pentium processor to achieve the accuracy stated. Wittek et al. also note that the model cannot be applied to events that change the topology of the brain such as tumor resection.

Although powerful, lack of fluid compartment and the pressure component detract the linear elastic model and the nonlinear/hyperelastic models from their usefulness. Hakim et al. [66] showed that the transmission of intraventricular pressure throughout the brain parenchyma created a stress distribution that varied in magnitude and direction and made the observation that the "brain acts like a sponge". Doczi [67] reported that the gray matter and white matter can increase their water content due to the difference in the number of capillaries and also pointed out that when the blood brain barrier is compromised interstitial pressure drives the fluid movement in the brain. These findings highlight the need for a pressure component and a fluid compartment in the model. In light of this fact, David Roberts and his research group at Dartmouth developed a 3D computational model based on Biot's theory of soil consolidation. In short Biot's consolidation theory gives a complete and

general description of the mechanical behaviour of a poroelastic medium [6] based on equations of linear elasticity for the solid matrix, Navier-Stokes equations for the fluid compartment and Darcy's law for the flow of fluid through the porous matrix.

Equations 7 and 8 were originally developed by Biot [68] to represent biphasic soil consolidation, but were later used by Nagashima et al. [69] and Paulsen et al. [70] to model the deformation behavior of brain tissue.

$$\nabla \cdot G\nabla\vec{u} + \nabla\frac{G}{1-2\nu}(\nabla \cdot \vec{u}) - a\nabla p = -(\rho_t - \rho_f)g \tag{7}$$

$$a\frac{\partial}{\partial t}(\nabla \cdot \vec{u}) + \frac{1}{S}\frac{\partial p}{\partial t} + k_c(p - p_c) = \nabla \cdot k\nabla p \tag{8}$$

where

$\vec{u}$ displacement vector

p interstitial pressure

G shear modulus

ν poisson's ratio

a ratio of fluid volume extracted to volume change of the tissue under compression

ρ_t tissue density

ρ_f fluid density

g gravitational unit vector

$1/S$ amount of fluid which can be forced into the tissue under constant volume

t time

k_c capillary permeability

p_c intracapillary pressure

k hydraulic conductivity

[6] A porous medium is one where a solid matrix is permeated by an interconnected network of pores filled with a fluid

Equation 7 reflects the equations of mechanical equilibrium and have been derived for a Hookean linear elastic material undergoing small deformations. Within this description, deformations can be caused by surface forces and displacements, the existence of interstitial fluid pressure gradients, and changes to tissue buoyancy forces. Additionally, this expression assumes that the continuum consists of a porous solid tissue matrix infused with an interstitial fluid whereby the matrix deforms as a linear elastic solid while the fluid flows according to Darcy's law. Equation 8 relates the time rate of change of volumetric strain to changes in interstitial hydration.

First reported within the context of gravity-induced brain shift by Miga et al. [71], the right-hand-side of Equation 7 is used to represent the effect of gravitational forces acting on the brain. The effect of gravitational forces on the brain can be modeled as a difference in density between tissue and surrounding fluid. Intraoperative CSF drainage reduces the buoyancy forces which serve to counteract gravity forces thus causing the brain to sag.

The last term on the left-hand-side of Equation 8 represents the hydrodynamic forces that act on the brain due to fluid capillary exchange. The term $k_c(p - p_c)$ represents the fluid exchange between capillary and interstitial spaces and can be used to simulate the effects of hyperosmotic drugs or swelling on the brain. Hyperosmotic drugs such as mannitol are administered to decrease the effect of elevated intracranial pressure due to edema. These drugs have the effect of reversing flow through the blood-brain osmotic barrier, drawing water from the extracellular brain space, thereby decreasing brain volume. This decreased capillary pressure pulls interstitial fluid from the extracellular brain space causing a decrease in tissue volume. Conversely, elevated capillary pressures increase local tissue volume, resulting in tissue stress and distortion. Intraoperative events such as tissue resection can also be modeled by decoupling the nodes corresponding to the preoperative tumor volume when assembling the stiffness matrix.

Miga et al. solved Equations 7 and 8 using the Galerkin weighted residual method. Finite element treatment of these equations coupled with a weighted time-stepping scheme results in an equation of the form $[\mathbf{A}]\,U_{n+1} = [\mathbf{B}]\,U_n + C_{n+\theta}$ where $[\mathbf{A}]$ and $[\mathbf{B}]$ represent

the stiffness matrices for the *n+1* and n^{th} time step respectively, C represents boundary condition information and known force distributions, and U represents the solution vector (3 displacements and pressure) at the node. The detailed development of these equations can be found in [70, 51].

In [71], Miga et al. reported that the computational model recaptured 79% of the error induced by intraoperative brain shift. Miga et al. [72, 73] demonstrated that the biphasic model can accurately predict deformations induced by surface loading conditions such as tissue retraction and resection. Also, for a 23000 node, 123500 element mesh with four degrees of freedom (DOF) at each node on a single central processing unit (CPU) Silicon Graphics Indigo workstation, Miga et al. [73] reported a run time of 8.5 minutes to simulate gravity-induced deformations, 6.5 minutes to simulate retraction, 5.5 minutes to simulate excision and 6.0 minutes to simulate unretraction for the first time step, and 5.75-7.0 minutes for every subsequent time step. Though the biphasic model is better suited to capture intraoperative events such as tissue resection and tissue deformations related to the intracranial pressure distribution, computation time and the assumption of linear elasticity are two of its major drawbacks.

To summarize, though fast and efficient the linear elastic and hyperelastic models do not account for intracranial pressure distributions and resulting tissue deformations. The biphasic model on the other hand accounts for the hydrated nature of the brain, but fails to capture the nonlinear deformation behavior of the brain tissue and is reportedly slower than the other models. This highlights the need for a "best of both worlds" scenario. In other words, this calls for a biphasic model that can capture the nonlinear deformation effects of the brain tissue and at the same time is fast enough to meet the real time constraints of neurosurgery.

Sparse intraoperative data in MUIGNS

While non-guided prediction is desirable, there is little doubt that the accuracy of brain shift models can be increased by integrating feedback from sparse intraoperative data [50].

Sparse, in this context, means data with limited information and/or spatial extent. A schematic of MUIGNS using sparse intraoperative data is shown in Figure 3

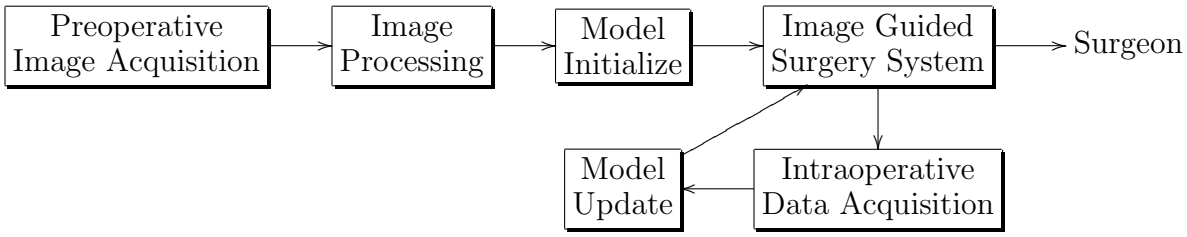

Figure 3: Schematic for using sparse intraoperative data in model updated image guided neurosurgical procedures (MUIGNS).

Sparse intraoperative data is typically used as displacement or stress boundary conditions to constrain the computational model. Using the measured sparse displacements, Ferrant et al. [74], Skrinjar et al. [54], Wittek et al. [52, 64] rigidly constrained their computational model to exactly match the measured displacements, as if they were known boundary conditions. Though this method is relatively easy to implement, it faces the potential limitation that since boundary displacements are constrained to match measured surface displacements, artificial forces can be introduced at the measured points which by observation are stress-free. More specifically, in this framework, all deformations result from the application of contact forces when the force environment is considerably more complex and could involve a myriad of contact and distributed loading conditions. Also, it should be noted that time taken to compute the displacements using the computational model and the time taken to integrate the sparse data with the computational model, must meet the real-time constraints of neurosurgery. Skrinjar et al.. define real-time for MUIGNS as being faster than the rate of brain deformation [54]. Thus the incorporation of sparse measurements must not only improve accuracy, but also significantly reduce the time required to update the preoperative images.

In [75], Lunn et al. introduced a strategy for integrating sparse intraoperative displacement data with the computational model. It should be noted that this work was based on the computational model developed by the research group at Dartmouth. The computational model was solved for a series of boundary conditions and these basis solutions were weighted

in accordance with a minimization procedure that reduced the error between the observed and predicted displacement fields. Lunn et al. demonstrated that with a good set of basis solutions the full volume displacement field can be predicted accurately and efficiently. This work however was restricted to *i*n-vivo porcine studies.

Extending their earlier work, Lunn et al. [76] presented a novel method that corrected brain shift by combining a best prior estimate(BPE) with a force perturbation correction technique to better match sparse data to model output. The reported method cast the model correction with a nonlinear optimization framework which uses the method of Lagrange multipliers to rapidly correct their BPE of brain deformations. They call the method the adjoint equation method (AEM) and have had encouraging preliminary results. While the mathematical approach is quite elegant, it still represents a challenging optimization framework that is significantly under-determined. Also in addition to the computational cost, the AEM reduces modeling efforts to solve for the optimal distribution of forcing functions rather than concentrating on generating a more deterministic model. For the sole purpose of shift correction, this is quite appropriate but the framework relies on using models to regularize data rather than model deformation events.

In [77], Davatzikos et al. presented a framework for modeling and predicting anatomical deformations from precomputed training samples using (i) a shape based estimation method (SBE) and (ii) a force based estimation method (FBE). In SBE, Davatzikos et al. use the principal modes of co-variation between shape and deformation to predict the most likely deformation corresponding to the novel shape that is presented to the training set. In FBE, they use the principal modes of co-variation between shape and forces to predict the most likely force acting on the novel shape that is presented to the training set. These forces can then be used to calculate the deformation of the object using a biomechanical model. The authors used elements of principal component analysis (PCA) to capture the statistical properties of the training set and to predict the most likely shape/force. Though the authors did not describe these methods in the context of predicting intraoperative brain shift, this work is significant because it introduced a novel concept of predicting as much as possible

of the intraoperative deformation using a precomputed training set.

Lunn et al. [75] and Davatzikos et al. [77] demonstrated that it is feasible to compute anatomical deformations using precomputed model solutions in a fast and accurate manner. Given these findings, it is worth exploring alternative approaches for integrating sparse intraoperative data with computational modeling.

CHAPTER III

MANUSCRIPT 1 - Model-updated Image-guidance: A statistical approach to gravity-induced brain shift

Original form of manuscript appears in Lecture Notes in Computer Science: Medical Image Computing and Computer Assisted Intervention: 2003, Vol. 2879:1, 375-382.

Abstract

Compensating for intraoperative brain shift using computational models has been used with promising results. Since computational time is an important factor during neurosurgery, a prior knowledge of a patient's orientation and changes in tissue buoyancy force would be valuable information to aid in predicting shift due to gravitational forces. Since the latter is difficult to quantify intraoperatively, a statistical model for predicting intraoperative brain deformations due to gravity is reported. This statistical model builds on a computational model developed earlier. For a given set of patient's orientation and amount of CSF drainage, the intraoperative brain shift is calculated using the computational model. These displacements are then validated against measured displacements to predict the intraoperative brain shift. Though initial results are promising, further study is needed before the statistical model can be used for model-updated image-guided surgery.

Introduction

In the past several years, the importance to account for intraoperative brain shift during image-guided neurosurgical procedures has been well documented. Also known as post imaging brain distortion or brain deformation, the shift can be caused by a variety of factors such as surgical manipulation, gravitational forces, clinical presentation of the patient, pharmacological responses, etc. Systematic studies have demonstrated that the fidelity of image-guided systems can be seriously compromised by brain deformations if left unchecked [78, 7]. One important statistically significant finding common to these studies is that the

direction of brain shift has a predisposition to move in the direction of gravity [78, 7]. To correct for deformations, various imaging techniques such as computed tomography (CT), magnetic resonance imaging (MRI), and ultrasound (US) have been used for intraoperative image-guided surgery, and each imaging procedure has its inherent advantages and disadvantages [79, 80, 16]. While CT and MR procedures have been labeled cumbersome and have been questioned for their cost-effectiveness, US lacks the image clarity that CT and MR scans produce.

As a cost-effective and an efficient method, computational modeling is a procedure that can translate complex surgical events into accurate estimates of tissue response and thereby compensate for intraoperative brain shift. Various computational models based on different physical and biomechanical principles have been developed [60, 71]. The biphasic model used by Miga et al.. has been shown to compensate for 70-80% of the intraoperative brain shift. In a study on gravity induced brain deformations[71], Miga et al.. report a reduction of error from 6mm to 1mm. However the amount of intraoperative CSF drainage (which determines the gravitational force in the biphasic model) and the patient's orientation in the OR with respect to gravity cannot be ascertained. Although the preoperative surgical plan can provide an estimate of the patient's orientation a priori, estimates for the degree of change in buoyancy forces acting on the brain are somewhat more elusive. Since computational time is an important factor in model updated image-guided surgery, prior knowledge of a patient's orientation and amount of CSF drainage would increase the effectiveness of model updated image-guided surgery.

The work presented here attempts to remove the uncertainties by combining a simple statistical model with that of the biphasic model reported in [71]. Although limited, the use of statistical models to compensate for tissue motion does have some precedent. Davatzikos et al.. [77] report a framework for modeling and predicting anatomical deformations with an emphasis on tumor induced deformations. Their statistical models were based on analyzing the principal modes of covariation between deformed and undeformed anatomy within the context of two separate methods: (1) a shape-based estimation (SBE) and, (2) a force-

based estimation using a biomechanical model. The results from these studies suggested that statistical models could be used to represent deformations from positional changes and tumor growth.

In this paper, a computational model is used to generate displacement data sets for a range of patient orientations and CSF drainage states. The statistical model combines these displacements using a nonlinear least squares approach. The rationale for this approach is provided by recent work reported by Miga et al.. [81]. In this study, a high-resolution laser-range scanner (LRS) was used to spatially characterize the patient's exposed cortical surface during neurosurgery. As a result, information regarding the nature of deformations during neurosurgery are derived and could be used as input for the statistical model reported in this paper. In addition, the statistically reconstructed displacement values are compared against independently measured displacements to assess accuracy. Simulations are also provided which are more closely related to data acquired by the LRS system used in [81].

Methods

Computational Model

This section briefly discusses the computational model used in this study. Equations 9 and 10 were originally developed by Biot [68] to represent biphasic soil consolidation, but were later used by Nagashima et al.. [69] and Paulsen et al.. [82] to model the deformation behavior of brain tissue. The last term on the left-hand-side in equation 9 represents the effect of gravitational forces acting on the brain. Intraoperative CSF drainage reduces the buoyancy forces which serve to counteract gravity forces thus causing gravitational forces to deform the brain. The effect of gravitational forces on the brain can be modeled as a difference in density between tissue and surrounding fluid. Figure 4 demonstrates the deformation effects of CSF drainage on the brain as modeled by equations

$$\nabla \cdot G\nabla u + \nabla \frac{G}{1-2\nu}(\nabla \cdot u) - \alpha \nabla p = -(\rho_t - \rho_f)g \tag{9}$$

$$\alpha \frac{\partial}{\partial t}(\nabla \cdot u) + \frac{1}{S}\frac{\partial p}{\partial t} - (\nabla \cdot k\nabla p) = 0 \tag{10}$$

where

$\vec{u}$ displacement vector

p interstitial pressure

G shear modulus

ν poisson's ratio

a ratio of fluid volume extracted to volume change of the tissue under compression

ρ_t tissue density

ρ_f fluid density

g gravitational unit vector

$1/S$ amount of fluid which can be forced into the tissue under constant volume

t time

k_c capillary permeability

p_c intracapillary pressure

k hydraulic conductivity

The partial differential equations can be solved numerically using the Galerkin weighted residual method. Finite element treatment of these equations coupled with a weighted time stepping scheme results in an equation of the form

$[\mathbf{A}]\,U_{n+1} = [\mathbf{B}]\,U_n + C_{n+\theta}$ where $[\mathbf{A}]$ and $[\mathbf{B}]$ represent the stiffness matrices for the *n+1* and n^{th} time step respectively, C represents boundary condition information and known force distributions, and U represents the solution vector (3 displacements and pressure) at the node. The detailed development of these equations can be found in previous publications [70, 51].

The boundary conditions used in the model are illustrated in Figure 5. Although the actual boundary conditions are patient specific, the highest elevations in the brain are stress-

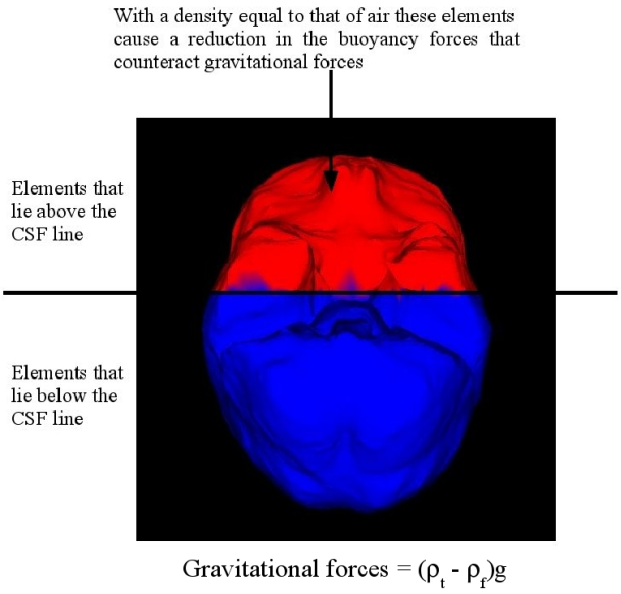

Figure 4: Effect of gravitational forces on the brain.

free and allow drainage to the surface; the mid elevations slide along the cranial wall and can experience partial drainage and the lowest elevations allow movement along the cranial wall but do not allow fluid drainage. The assumed level of intracranial CSF determines the fluid drainage boundary condition for the highest and mid elevations in the brain.

Statistical Model

As discussed above, the amount of intraoperative CSF drainage and patient's orientation in the OR which determines orientation of gravitational acceleration vector in equation 9 are two important variables in predicting intraoperative brain shift. A statistical based model has been developed to compensate for these uncertainties. As shown in Figure 6, the model begins by building a deformation atlas based on the patient's preoperative MR images. Equations 9 and 10 are solved assuming a range of patient orientations and degrees of intraoperative CSF drainage based on preoperative surgical planning. This series of model solutions serves as a statistical data set that can be used to characterize intraoperative deformations under varying surgical presentations. Having built the deformation atlas, a least squares regression analysis is performed with non-negativity constrains (provided by

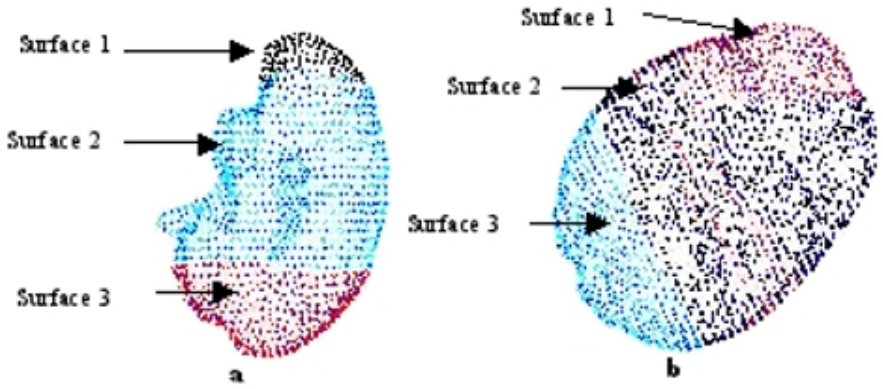

Figure 5: Boundary condition template for (a) neutral head orientation and (b) patient's head turned 60◦ in the OR.Surface 1 is stress-free at atmospheric pressure; Surface 2 slides along the cranial wall but not along the normal direction and surface and Surface 3 is fixed at atmospheric pressure. The amount of intraoperative CSF drainage determines the drainage boundary condition.

MATLAB (Mathworks Inc.)) using the objective function below:

$$Minimize||Ex - f||subject\ to\ x \geq 0 \tag{11}$$

where f is a vector of n measured displacements, E is a matrix where E_{ij} is the displacement value for ith nodal position on the surface at the jth orientation and CSF drainage level. E also contains a requirement that the regression coefficients must add to unity. The unknown coefficients associated with the regression analysis are x and they are used to calculate the intraoperative brain shift as shown below.

$$Intraoperative\ brain\ shift = X_l * x \tag{12}$$

where X_l is the matrix containing the displacement field vectors for all points in the brain at the various orientations/CSF drainage levels and x is a vector of coefficients obtained from solving equation 11.

The findings of Miga et al.. [71] were used to validate the combined statistical and biphasic model. The values reported in Table 1, columns 1-4 are reproduced from their work

published in IEEE Transactions of Medical Imaging, Vol. 18, No. 16, 1999. In their paper, they simulate the intraoperative brain shift for four different human cases using the computational model and also measure the intraoperative brain shift for four points on the cortical surface in the direction of gravity. These measured displacements are used in equation 11 as the basis for determining the regression coefficients. After calculating the coefficients, results from the statistical model are compared to measured data and performance is reported in Table 1.

Although the above intraoperative data is sparse, a laser range scanner significantly improves the number of measured data points and hence should constrain and aid the statistical model. To simulate this, for each patient, a specific orientation and CSF level were selected which were not to be part of the statistical solution set. In all cases, the computational model was executed for a range of patient orientations and CSF drainage states. The coefficients were then calculated using the statistical model and intraoperative brain shift was compared to the model solution not included within the statistical set. The results are presented in the following section.

Results

Comparison of statistical model with measured displacements reported by Miga et al.

The results of the statistical model are compared with the measured displacements in Table 1. The values in column 3 and column 4 are based on the findings of Miga et al. [71]. Column 5 shows the statistical model prediction on a point-by-point basis. Point 3 in Patients 3 and 4 was on bone and hence experienced no shift.

Averaging over all points in the four human cases, the statistical model produces an absolute error of 1.1±0.9mm. For the computational model, Miga et al. report an average error of 1.2±1.3 mm. The statistical model predicts approximately 75-80% of the intraoperative brain shift.

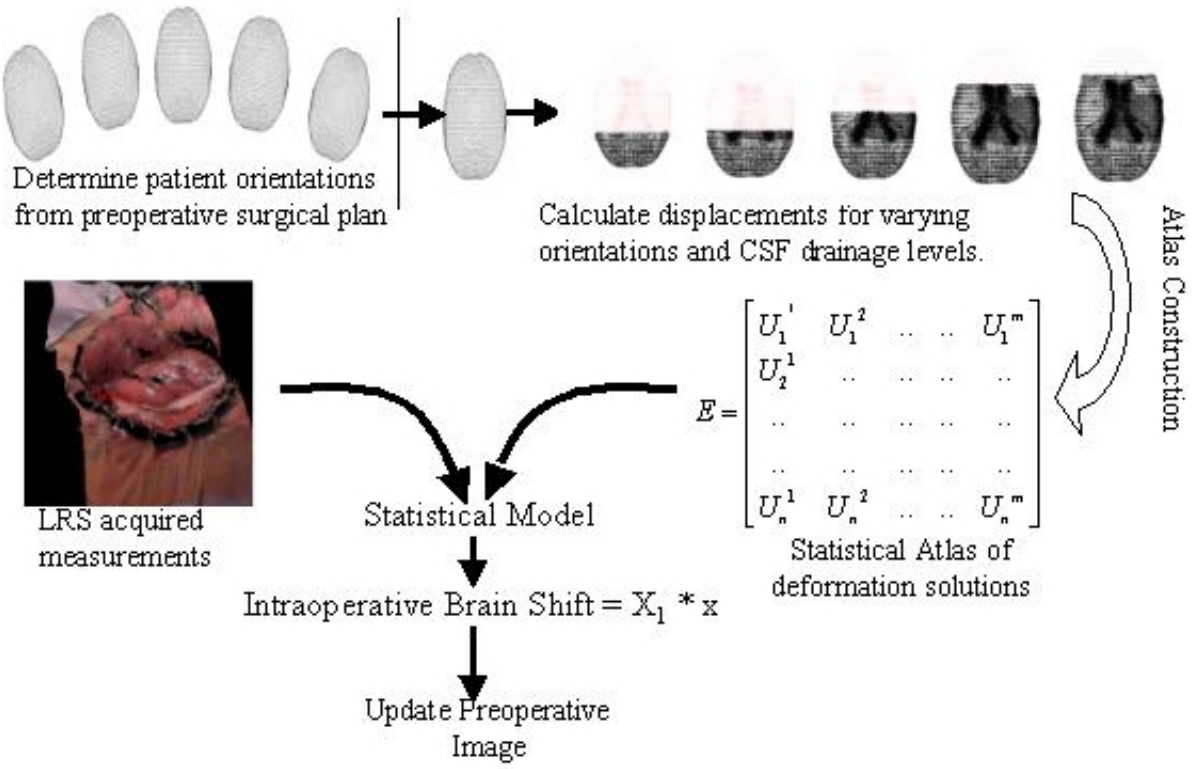

Figure 6: Proposed Statistical Model.

Comparison of statistical model with the simulated intraoperative data acquisition case

The results of the statistical model for the simulation are shown in Table 2. The values in column 2 report the maximum difference between the measured intraoperative displacements and those predicted by the statistical model. In a similar fashion the values in column 3 represent the mean error. Averaging over all points in the four human cases, the statistical model produces an absolute maximum error of 0.7±0.8mm and a mean error of 0.1mm±0.08mm. Relative to the average cortical displacement of 2.4 mm, the statistical model predicts an average error of 0.1 mm, indicating that it recaptured 96% of the simulated intraoperative brain shift.

Discussion

The statistical model performed comparably to published results and was able to compensate for 75-80% of brain deformation. To increase the accuracy, simulations suggest that

Subject	Point #	Measured Displ. (mm)	Computational model Displ. (mm)	Statistical Model Displ. (mm)
Pt. 1	1	6.7	4.9	4.7
	2	4.6	5.4	5.1
	3	4.2	5.8	5.4
	4	3.5	3.4	3.6
Pt. 2	1	10.4	5.7	7.4
	2	6.2	6.3	7.2
	3	5.9	6.2	7.8
Pt. 3	1	6.1	5.2	4.8
	2	5.0	6.5	6.2
	3	7.5	6.1	5.9
Pt. 4	1	4.4	4.8	4.5
	2	3.5	3.8	3.4

Table 1: Comparison between measured shift, computational and statistical model based shift with respect to gravity.

Subject	Max. Error (mm)	Mean Error (mm)
Patient 1	1.9	0.2
Patient 2	0.3	0.006
Patient 3	0.4	0.07
Patient 4	0.3	0.07

Table 2: Maximum and mean errors generated by the statistical model for the simulated intraoperative data acquisition.

dense intraoperative cortical shift measurements may be appropriate. In the simulation case reported, the statistical model results in an average error of 0.1 mm displacement error and predicts approximately 96% of the intraoperative brain shift. With the advent of cheap and efficient intraoperative data acquisition techniques such as laser range scanning [81], the statistical model can prove to be a useful tool for model updated image guidance. Furthermore, the statistical model should significantly reduce intraoperative computational time since perturbations of patient orientation and the state of CSF drainage can be precomputed.

Conclusions

A statistical based approach has been outlined for image-guided surgery. The statistical model was compared with measured intraoperative data and with a simulated intraoperative

case. These simulations showed a good match between the brain shifts predicted by the computational model and that predicted by the statistical model. Given the prominent role that gravity takes in the development of brain shift, it is encouraging that a relatively simple statistical model increases the model-updating speed by providing a framework to pre-compute the early stages of brain shift and can also be used to compensate for this motion.

Acknowledgements

This work has been supported by the Vanderbilt University Discovery Grant Program. Also, special acknowledgement to Dr. Keith Paulsen and Dr. David Roberts of Dartmouth Colleges Thayer School of Engineering (Hanover, NH) and Dartmouth Hitchcock Medical Center (Lebanon, NH), respectively, who provided the clinical data for this paper.

CHAPTER IV

MANUSCRIPT 2 - An Atlas-Based Method to Compensate for Brain Shift: Preliminary Results

Original form of manuscript appears in Medical Image Analysis, Vol. 11:2, 128-145.

Abstract

Compensating for intraoperative brain shift using computational models has shown promising results. Since computational time is an important factor during neurosurgery, *a priori* knowledge of the possible sources of deformation can increase the accuracy of model-updated image-guided systems. In this paper, a strategy to compensate for distributed loading conditions in the brain such as brain sag, volume changes due to drug reactions, and brain swelling due to edema is presented. An atlas of model deformations based on these complex loading conditions is computed preoperatively and used with a constrained linear inverse model to predict the intraoperative distributed brain shift. This relatively simple inverse finite-element approach is investigated within the context of a series of phantom experiments, two in vivo cases, and a simulation study. Preliminary results indicate that the approach recaptured on average 93% of surface shift for the simulation, phantom, and in vivo experiments. With respect to subsurface shift, comparisons were only made with simulation and phantom experiments and demonstrated an ability to recapture 85% of the shift. This translates to a remaining surface and subsurface shift error of 0.7 ± 0.3mm, and 1.0 ± 0.4mm, respectively, for deformations on the order of 1 cm.

Introduction

Ever since its advent, medical imaging has played a significant role in surgical planning and treatment because it provides valuable information about anatomical structures and function. This has been particularly helpful for neurosurgical procedures where often the surgeon has to remove a tumor without damaging the healthy brain tissue surrounding it.

In order to take advantage of image guidance during a neurosurgical procedure (also known as image-guided neurosurgery, IGNS), preoperative tomograms of the patient must be registered to the patient's anatomy in physical space. While image-to-patient rigid alignment is relatively straight-forward, clinical studies in IGNS have exposed limitations to this approach. Systematic studies have reported that the brain is capable of deforming during surgery for a variety of reasons, including pharmacologic responses, gravity, edema, surgical manipulation and respiration [7, 8, 9] and that the brain can shift a centimeter or more in a non-rigid fashion [10].

To correct for deformations, various imaging techniques such as computed tomography (CT) [25], magnetic resonance imaging (MRI) [9], and ultrasound (US) [83] have been investigated for intraoperative image-guided surgery. CT procedures have been questioned for their dose exposure, while MR procedures are considered cumbersome and have been questioned for their cost-effectiveness. Current US systems suffer from low soft-tissue contrast and lack image clarity as compared to CT and MR imaging methods. Therefore, in their current state intraoperative imaging systems do not present a complete solution for guidance correction of the brain shift phenomenon.

As a cost-effective and efficient method, computational modeling is a procedure that can translate complex surgical events into accurate estimates of tissue response and thereby compensate for intraoperative brain shift. In model-updated image-guided neurosurgery (MUIGNS), a biomechanical model of brain shift is driven with sparse data[1] to accurately deform preoperative images to their current intra-operative position. Several groups have investigated the potential value of physical/biomechanical models underpinned by various biomechanical concepts [51, 52, 53, 54, 55, 56, 57]. Towards this end, Paulsen et al. [70] reported a 3-D biomechanical model governed by consolidation mechanics. Additional development of the equations and their solutions can be found elsewhere [70, 51]. In this work, a patient-specific mesh is created and case-specific boundary data such as tumor resection and/or tissue retraction is imposed to generate updates of the preoperative images over the

[1]Sparse data is defined as data with limited intraoperative extent or information

entire course of surgery. Despite previous success with the model approach [71, 72, 73, 84, 85], there are several remaining challenges discussed below that need addressing.

One of the greatest challenges presented by MUIGNS is that the computational time associated with the model does not meet the real-time constraints of neurosurgery. For a 23000 node, 123500 element mesh with four degrees of freedom (DOF) at each node on a single central processing unit (CPU) Silicon Graphics Indigo workstation, Miga et al. [73] reported a run time of 8.5 minutes to simulate gravity-induced deformations, 6.5 minutes to simulate retraction, 5.5 minutes to simulate excision and 6.0 minutes to simulate unretraction for the first time step, and 5.75-7.0 minutes for every subsequent time step. These run times can be significantly improved with use of parallel processing and more powerful computers, as demonstrated by Warfield et al. [40]. Using a Sun Microsystems Sun Fire 6800 with 12 750MHz UltraSPARC-III CPUs, for a 43584 nodes, 214035 element mesh with three DOF at each node, Warfield et al. reported a run time of 15 seconds. These performance improvements are encouraging and will only add to the impetus to bring complex models to the operating room.

Another critical component of MUIGNS is the accurate translation of boundary conditions during the course of surgery. For example, the amount of cerebrospinal fluid (CSF) loss during surgery and the head orientation of the patient in the operating room (OR) may be two important factors in determining the degree of shift from gravitational forces [71]. Although the preoperative surgical plan can provide an estimate of the patient's orientation *a priori*, estimates for the degree of change in buoyancy forces acting on the brain are somewhat more elusive. Related to the hydrated nature of the brain, intracranial pressure from the edematous tissue surround tumors can cause the brain to swell within the craniotomy region. Models that are biphasic in nature may be better suited to capture these brain shift effects. In addition, deformations from retractor blades and internal strain energy changes that occur during tumor exposure and resection can also contribute to brain shift during surgery. Each of these factors present a challenge with respect to prescribing boundary and internal forcing conditions. While non-guided prediction is desirable, there is little doubt

that the accuracy of brain shift models can be increased by integrating feedback from sparse intraoperative data [50]. These sparse displacement measurements can be obtained from a number of sources [11, 10, 86, 87, 2, 88]. Sparse intraoperative data is typically used as displacement or stress boundary conditions to constrain the computational model. Using the measured sparse displacements, Ferrant et al. [74] and Skrinjar et al. [54] rigidly constrained their computational model to exactly match the measured displacements, as if they were known boundary conditions. Though this method is relatively easy to implement, it faces the potential limitation that since boundary displacements are constrained to match measured surface displacements, artificial forces can be introduced at the measured points which by observation are stress-free. More specifically, in this framework, all deformations result from the application of contact forces when the force environment is considerably more complex and could involve a myriad of contact and distributed loading conditions. Given this, it is worth exploring alternative approaches for integrating sparse intraoperative data with computational modeling. Also, it should be noted that time taken to compute the displacements using the computational model and the time taken to integrate the sparse data with the computational model, must meet the real-time constraints of neurosurgery. Thus the incorporation of sparse measurements must not only improve accuracy, but also significantly reduce the time required to update the preoperative images.

In recent developments, Lunn et al. [76] presented a novel method that corrects brain shift by combining a best prior estimate(BPE) with a force perturbation correction technique to better match sparse data to model output. The reported method casts the model correction with a nonlinear optimization framework which uses the method of Lagrange multipliers to rapidly correct their BPE of brain deformations. They call the method the adjoint equation method (AEM) and have had encouraging preliminary results. While the mathematical approach is quite elegant, it still represents a challenging optimization framework that is significantly under-determined. Also in addition to the computational cost, the AEM reduces modeling efforts to solve for the optimal distribution of forcing functions rather than concentrating on generating a more deterministic model. For the sole purpose

of shift correction, this is quite appropriate but it focuses the framework at using models to regularize data rather than model deformation events.

In the work presented here, a constrained linear inverse model is combined with a biomechanical tissue model to best fit the measured sparse intraoperative data. Initially presented in [89], the method reported here extends the earlier framework by incorporating a smoothing constraint to improve the efficiency and accuracy of solution. In order to account for the degree of uncertainty associated with all the sources of deformation, the computational model is run multiple times and these multiple model solutions are combined with the help of a inverse model to predict the intraoperative brain shift. It should also be noted that a considerable amount of the framework can be pre-computed and that at this time the inverse approach is a direct solution. With this technique, the model solutions act as training samples for the inverse model and the sparse intraoperative data act as control points, thereby removing the degree of uncertainty associated with MUIGNS. The framework proposed herein has some specific distinctions from the work of others: (1) the atlas of deformations is constructed from simulations based on physiological events, therefore the framework moves beyond the role of image interpolator to one that provides quantitative estimates of deformation-related properties (e.g. stresses, interstitial pressure dynamics, etc.), (2) the atlas of solutions generated is of more considerable breadth and attempts to include all the forces causing intraoperative brain shift and the varying surgical presentations of the patient (e.g. mannitol induced deformations, gravity-induced sag, and resection), (3) the inverse model is linear, and takes advantage of pre-processing, (4) the framework introduces a simple weighting scheme to constrain the atlas, and (5) presents a semi-automatic boundary condition generator to translate the boundary conditions encountered in the OR and should allow for the easy reproduction by others.

In this study, the fidelity of a constrained linear inverse model approach is demonstrated in a phantom experiment, two in vivo cases and a simulation study. It should be noted that though the sparse intraoperative data can include both pressure and displacement measurements, displacement data was chosen to test the accuracy of the proposed inverse model.

In this study a laser-range scanner (LRS) is used to acquire sparse data measurements [2, 90]. The laser-range scanner used in [2] is capable of generating a three-dimensional point cloud corresponding to (x,y,z) cartesian coordinates and two-dimensional texture coordinates (u,v). In [2, 90] the LRS was modified by the attachment of 12 infrared light emitting diode (IRED) markers, allowing for the scanner to be tracked in physical-space. The approach to measuring brain shift using LRS is as follows: LRS is used to scan the cortical surface, the initial scan is registered to the patient's preoperative images thereby establishing a correspondence between image-space and physical-space [81], the brain then deforms during surgery, and LRS is used to acquire a serial scanning dataset of the cortical surface after deformation. The shift acquired is then transformed to physical-space coordinates with the aid of a calibration phantom. The shift-tracking protocol using LRS has been described in detail in [2]. These sparse intraoperative measurements are used to constrain the linear inverse model. Also to meet the real-time demands of neurosurgery a parallel implementation of the computational model on a multiprocessor architecture is considered.

Methods

Computational Model

Equations 13 and 14 were originally developed by Biot [68] to represent biphasic soil consolidation, but were later used by Nagashima et al. [69] and Paulsen et al. [70] to model the deformation behavior of brain tissue.

$$\nabla \cdot G\nabla\vec{u} + \nabla\frac{G}{1-2\nu}(\nabla\cdot\vec{u}) - a\nabla p = -(\rho_t - \rho_f)g \tag{13}$$

$$a\frac{\partial}{\partial t}(\nabla\cdot\vec{u}) + \frac{1}{S}\frac{\partial p}{\partial t} + k_c(p - p_c) = \nabla\cdot k\nabla p \tag{14}$$

where

$\vec{u}$ displacement vector

p interstitial pressure

G shear modulus

ν poisson's ratio

a ratio of fluid volume extracted to volume change of the tissue under compression

ρ_t tissue density

ρ_f fluid density

g gravitational unit vector

$1/S$ amount of fluid which can be forced into the tissue under constant volume

t time

k_c capillary permeability

p_c intracapillary pressure

k hydraulic conductivity

Equation 13 reflects the equations of mechanical equilibrium. Within this description, deformations can be caused from surface forces and displacements, the existence of interstitial fluid pressure gradients, and changes to tissue buoyancy forces. Additionally, this expression assumes that the continuum consists of a porous solid tissue matrix infused with an interstitial fluid whereby the matrix deforms as a linear elastic solid while the fluid flows according to Darcy's law. Equation 14 relates the time rate of change of volumetric strain to changes in interstitial hydration.

First reported within the context of gravity-induced brain shift by Miga et al. [71], the right-hand-side of Equation 13 is used to represent the effect of gravitational forces acting on the brain. The effect of gravitational forces on the brain can be modeled as a difference in density between tissue and surrounding fluid. Intraoperative CSF drainage reduces the buoyancy forces which serve to counteract gravity forces thus causing the brain to sag.

The last term on the left-hand-side of Equation 14 represents the hydrodynamic forces that act on the brain due to fluid capillary exchange. The term $k_c(p-p_c)$ represents the fluid exchange between capillary and interstitial spaces and can be used to simulate the effects

of hyperosmotic drugs or swelling on the brain. Hyperosmotic drugs such as mannitol are administered to decrease the effect of elevated intracranial pressure due to edema. These drugs have the effect of reversing the blood-brain osmotic barrier, drawing water from the extracellular brain space, thereby decreasing brain volume. This decreased capillary pressure pulls interstitial fluid from the extracellular brain space causing a decrease in tissue volume. Conversely, elevated capillary pressures increase local tissue volume, resulting in tissue stress and distortion. A pressure elevation of 20-30mmHg has been measured in experimental brain edema and shown to be capable of driving edema fluid through the brain [91] (for this work, a value of 27 mmHg was used). The term $k_c(p - p_c)$ is intended to model these fluid exchanges. It should be noted that the effects of mannitol are modeled as a volumetric force with decreased pressures acting on the whole brain, whereas tissue swelling is modeled as a local force with elevated pressures acting in the edematous region alone. Material properties reported in the Appendix are based on values in the literature as well as those deduced through optimization in experiments by Miga [51]. As reported in the appendix, a heterogenous distribution of k_c is assumed to account for the different structural and biomechinal characteristics of the gray and white matter, tumor and edema.

Equations 13 and 14 are solved numerically using the Galerkin weighted residual method. Finite element treatment of these equations coupled with a weighted time-stepping scheme results in an equation of the form $[\mathbf{A}]\,U_{n+1} = [\mathbf{B}]\,U_n + C_{n+1}$ where $[\mathbf{A}]$ and $[\mathbf{B}]$ represent the stiffness matrices for the *n+1* and n^{th} time step respectively, C represents boundary condition information and known force distributions, and U represents the solution vector (3 displacements and pressure) at the node. The detailed development of these equations can be found in previous publications [70, 51].

The boundary conditions used in the model are illustrated in Figure 7 and was first reported in [85]. Although the actual boundary conditions are patient specific, the highest elevations in the brain are stress-free, the mid-elevations are permitted to move along the cranial wall, while the brain stem is fixed. The amount of intraoperative CSF drainage determines the fluid drainage boundary condition for each of these elevations. Elements and

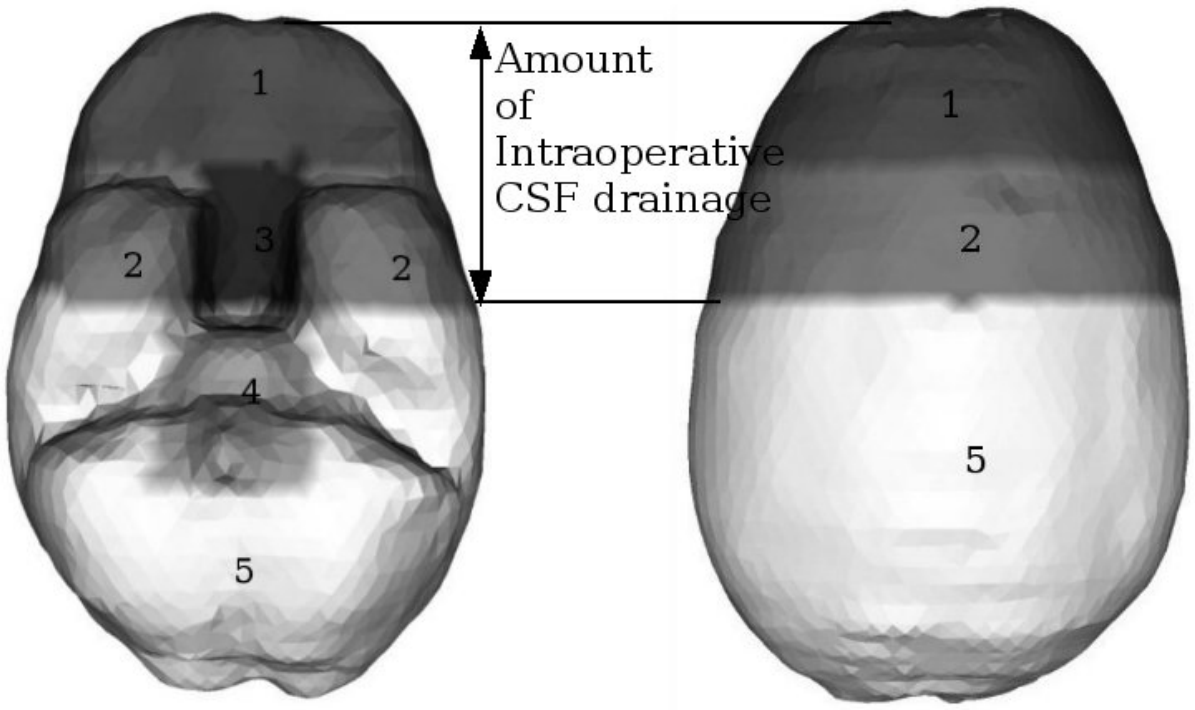

Figure 7: BC set for a supine patient with neutral head orientation in the OR. Displacement BCs : Surface 1 is stress-free at atmospheric pressure. Surfaces 2 and 5 are permitted to move along the cranial wall but not along the normal direction. Surfaces 3 and 4 are fixed for displacements. Interstitial pressure BCs : Surfaces 1,2 and 3 lie above the assumed level of intraoperative CSF drainage and therefore reside at atmospheric pressure. Surfaces 4 and 5 lie below the assumed level of intraoperative CSF drainage and therefore allow no fluid drainage.

hence the corresponding nodes in the mesh lying above the assumed level of intraoperative CSF drainage are assumed to reside at atmospheric pressure, while elements lying below the CSF drainage level do not allow fluid drainage. These boundary conditions were used to validate the accuracy of the computational model in [92, 85, 93]. The results reported suggest that these boundary conditions compare well to those encountered in the OR.

Parallel Computation of the Finite Element Model

As described earlier, the volumetric deformation of the brain is determined by solving the three displacements (x,y and z) and pressure (p) at each node of the finite element mesh. Each node thus gives rise to four degrees of freedom. The elements in the finite element mesh matrix are divided equally amongst the processors available for computation. The boundary

conditions are then applied in a similar manner (divided amongst available processors). It should be noted that though the rows of the matrix and the boundary condition nodes are divided equally amongst the processors, some processors do more work than others due to the irregular connectivity of the mesh. The Portable, Extensible Toolkit for Scientific Computation(PETSc) package [94, 95, 96] is used to assemble the stiffness matrix and to solve the biphasic brain model.

Inverse Model

As discussed above, computation time is an important factor in MUIGNS. By incorporating *a priori* knowledge about the sources of deformation, it may be possible to improve efficiency of a MUIGNS system by decreasing the computational time and it may also be possible to increase the accuracy of a MUIGNS system. With respect to the accuracy, certain aspects of the brain shift problem can be difficult to predict within the OR environment regardless of available data acquisition. For example, in the practical OR setting, it is very difficult to differentiate shift due to changes in CSF volume and from fluid-depleting drugs such as mannitol. Even something as simple as knowing the patient orientation in the OR, i.e., the direction of gravity with respect to the brain can be challenging. For example, in frameless stereotactic procedures, the reference emitter is commonly attached to the patient's fixation. This allows tracked instruments to be directly related to the patient's image volume once the patient has been registered. This has the advantage that as the patients bed is lowered and/or rotated, the reference frame is rotated with the patient. However, in so doing, the absolute reference to the OR (the reference frame of gravity) can be lost unless a second reference emitter is attached to OR space (not commonly done). Without a second reference emitter, the direction of gravity relative to the patient is lost. One approach to addressing this uncertainty is to generate an atlas of deformation solutions based on a range of possible surgical presentations. This has the added benefit to efficiency by allowing for precomputation of the deformation atlas.

In this paper, a realization to the brain shift compensation problem is proposed using a

precomputed deformation atlas. Operationally, Equations 13 and 14 are solved for a range of possible factors causing brain shift. Let the deformation atlas, **E**, be the matrix obtained by assembling these model solutions whereby **E** is of size (nx3)$\times m$, where n is the number of nodes in the finite element mesh, 3 is the number of Cartesian displacement components at each node, and m the number of model solutions. In general, nx3 is significantly larger than m, so **E** is a rectangular matrix. The model-data misfit error between a linear combination of precomputed displacement solutions and the actual displacements can be written as,

$$\varepsilon_{volume} = [\mathbf{E}]\{\alpha\} - \{U\} \tag{15}$$

where U is the measured volumetric intraoperative shift, i.e., shift at all nodes and is (nx3)x1 vector, and α is the mx1 vector of regression coefficients. This can then be expressed as the least squared error objective function,

$$G_{volume}(\alpha) = ([\mathbf{E}]\{\alpha\} - \{U\})^T([\mathbf{E}]\{\alpha\} - \{U\}) \tag{16}$$

As noted above, the measurements U are often incomplete or sparse. As a result, model solutions within **E** are interpolated to the specific measured intraoperative data points and these interpolated solutions are assembled in an intraoperative sparse deformation atlas, **M**. Thus **M** is of size (n_sx3)xm, where n_s is the number of points for which sparse intraoperative data has been measured. The displacement data sets in **M** serve as the training samples for the inverse model and reduce the model-data misfit error, and objective function to

$$\varepsilon_{sparse} = [\mathbf{M}]\{\alpha\} - \{u\} \tag{17}$$

$$G_{sparse}(\alpha) = ([\mathbf{M}]\{\alpha\} - \{u\})^T([\mathbf{M}]\{\alpha\} - \{u\}), \tag{18}$$

respectively. Here, u is the sparse intraoperative shift measured at n_s points in the brain. This, however, can transform the problem into an undetermined system because there are

usually more regression coefficients than measurement points (i.e. $m > n_s$). While minimum norm solutions can produce perfect fitting of the data they are often unsatisfying with respect to volumetric shift prediction due to the measurements being confined to a small spatial region (e.g. craniotomy in this case). This is addressed by introducing an extra constraint, which has the effect of encouraging a spatially smooth displacement field that is confined within the cranial extents. The modified objective function can be written as,

$$G_{sparse}(\alpha) = ([\mathbf{M}]\{\alpha\} - \{u\})^T([\mathbf{M}]\{\alpha\} - \{u\}) + \phi[W]^T\{\Upsilon\}\{\alpha\} \tag{19}$$

The second term in this expression is a function of the mechanical strain energy at each point within the model and serves to constrain the regression coefficients to values that would also minimize the elastic energy across the deformation atlas. In this expression, the term Υ refers to the linear elastic strain energy matrix, described by $\Upsilon_{i,j} = 1/2\{\epsilon_{i,j}\}^t[S_{i,j}]\{\epsilon_{i,j}\}$, where $S_{i,j}$, $\epsilon_{i,j}$ is the elastic stiffness tensor, and Cartesian strain tensor in vector form, respectively, for the i^{th} node of the j^{th} solution from the atlas (material properties are in Appendix). With the development of any multi-term objective function (Equation 19), care must be taken to allow proper scaling of terms such that the data is matched optimally while also retaining the beneficial effects of constraints. This process of regularization is often problem specific. With this in mind, a distance based weighting factor vector $W^T = [W_1, W_2, W_3, ...]$ is introduced that is similar to that in [97], and is used with the strain energy matrix described above. The weighting vector is constructed as,

$$W_i = \frac{1}{(1 + r_i/l)e^{-r_i/l}} \tag{20}$$

where r_i is the distance between the centroid of the measurement nodes and the i^{th} node in the brain volume. The l is a characteristic length that specifies the domain over which measurement nodes should have influence. With that, the form of Equation 20 reduces the strain energy constraint within the region of measurements nodes, i.e. the craniotomy in this case. While displacements tend to be small in areas remote from the craniotomy, they

will have increased strain energy and increased weighting. When Equation 19 is optimized for the regression coefficients, the net effect of the constraint term is to enforce a minimal elastic energy state on remote regions of the domain while selecting coefficients that best match the shift in the cranial and tumor regions. ϕ in Equation 19 provides a scaling role such that the solution is not biased by the strain energy constraint term. The values for l and ϕ were found empirically and are 0.125 and 1/2700, respectively.

Finally, setting the partial derivative to zero, the optimum for Equation 19 has a direct solution for $\{\alpha\}$. Once the regression coefficients are determined, these are used to calculate the full volume displacements using

$$\{U^*\} = E\alpha \tag{21}$$

where $\{U^*\}$ is the predicted volumetric brain shift.

Figure 8 shows a schematic of the MUIGNS system using the inverse finite-element model approach.

Automatic Boundary Condition Generator and Atlas Formation

In order to predict intraoperative brain shift using the inverse model based on a precomputed deformation atlas, a number of training samples/displacement data sets are required. Additionally, for increased accuracy, it is important that the model represent the degree of uncertainty associated with all the sources of deformation. For example, a deformation atlas for predicting gravity-induced brain deformations should contain displacement data sets for a range of possible patient orientations in the OR and varying degree of buoyancy force changes for each patient orientation. The surgeon's preoperative plan can be used to approximate the patient's orientation in the OR and subsequently used to generate multiple boundary condition sets (BCs), to sample all possible patient orientations. This underscores the need for a template BC that is accurate so as to facilitate automatic BC generation.

Based on the BC representation shown in Figure 7, a patient-specific automatic bound-

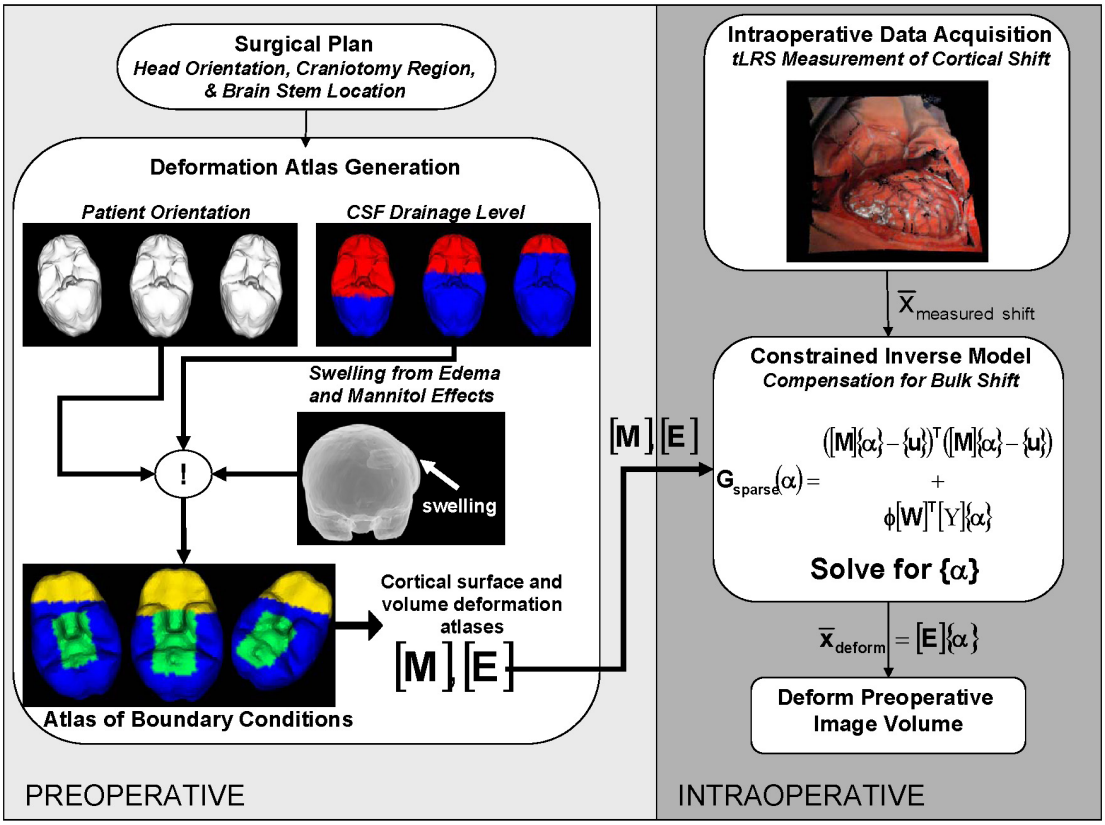

Figure 8: Framework for MUIGNS using the constrained linear inverse model.

ary condition generator has been developed. The only necessary inputs are the approximate patient orientation in the OR as predicted by the neurosurgeon's preoperative surgical plan, an anticipated region/size for the craniotomy, the computational mesh based on the preoperative image volume, and the location of the patient's brain stem in the preoperative image study. Based on this information, all possible patient orientations in the OR are assumed and BCs for the patient-specific mesh domain are generated. The automatic BC generator algorithm is as follows:

1. For a given preoperative patient-orientation estimate (PPoE), the node normals for all nodes on the boundary are calculated and the following operation is performed over all boundary nodes : $\vec{e}_g \cdot \vec{e}_{n_i} \leq \xi$, i = 1,2,3,...,$n$ boundary nodes, where $\vec{e}_g$ is the gravitational unit vector, $\vec{e}_{n_i}$ is the unit vector associated with the nodal normal to

the brain surface for the i^{th} boundary node and ξ is a scalar tolerance specified by the user[2]. Boundary nodes that satisfy this condition are assigned stress-free boundary conditions (Neumann condition), while those that do not are allowed to slide along the cranial cavity but not in the direction of the surface normal. However in cases where tissue swelling, due to elevated intracranial pressure, is to be taken into account, the nodes in craniotomy region are identified and assigned stress-free boundary conditions while other boundary nodes are allowed to slide along the cranial cavity but not in the direction of the surface normal.

2. The brainstem is identified from the patient's preoperative images and nodes within a given radius are classified as fixed (Dirichlet condition), which overrides the conditions determined in Step 1.

3. The interstitial pressure BCs are determined by: $\vec{d_i} \cdot (-\vec{e_g}) \geq h_j; h_{min} \leq h_j \leq h_{max}$, j = 1,2,3,...,$m$ elevations, where $\vec{d_i}$ is the Cartesian coordinate of the i^{th} boundary node and h_j is an elevation distribution. Based on previous experience in the OR, it has been determined that the upper (h_{max}) and lower bound (h_{min}) for the elevation distribution is 65% and 15% of the total elevation, respectively. Boundary nodes that satisfy the above expression are considered to be at atmospheric conditions (Dirichlet condition in pressure), while those that do not are the non-draining regions of the brain (Neumann condition in pressure).

4. Elements in the domain with reduced buoyancy forces are identified based on the following expression : $\vec{D}_k \cdot (-\vec{e_g}) \geq h_j; h_{min} \leq h_j \leq h_{max}$, j = 1,2,3,...,M elevations, where $\vec{D}_k$ is the Cartesian position of the k^{th} tetrahedral element centroid. Elements satisfying this condition are considered to have a complete reduction in their buoyancy forces and are assumed to have a surrounding fluid density equal to that of air (ρ_f as shown in Equation 13). Elements that do not satisfy the above condition are assumed to have a surrounding fluid density equal to that of the tissue density (ρ_t as shown in

[2]We found that a threshold value between $\xi = -0.2$ and $\xi = -0.3$ worked best for all patient orientations

Equation 13).

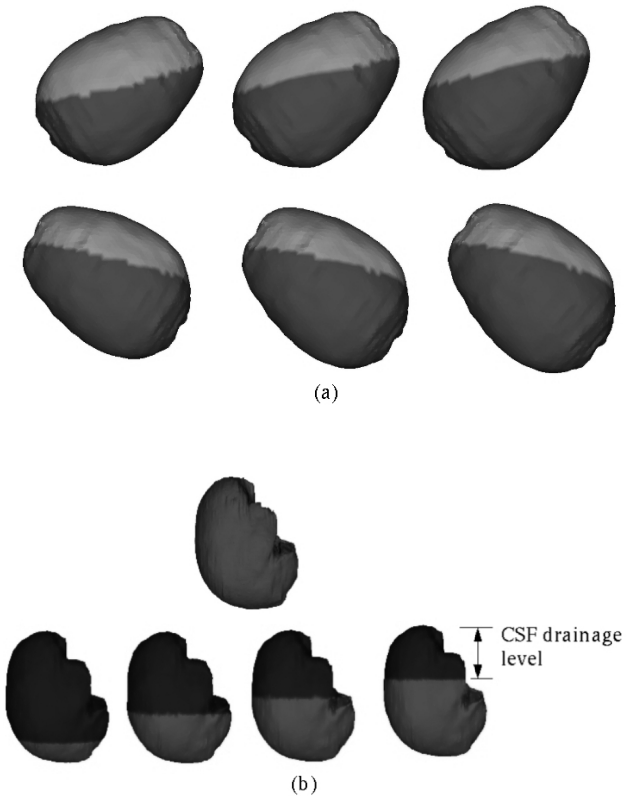

Figure 9: BC atlas developed using the automatic BC generator algorithm. (a) Displacement BCs generated for varying patient orientations based on PPoE. Nodes in the light gray regions of the figure are assigned stress-free BCs and those in the dark gray regions are allowed to slide along the cranial cavity but not in the direction of the surface normal. (b) Pressure BCs for varying levels of intraoperative CSF drainage, for a given patient orientation. Nodes above the CSF drainage level (black region) are assumed to be at atmospheric conditions and nodes below the CSF drainage level (gray region) are assumed to be the non-draining regions of the brain. Also, elements in gray are submerged in CSF and are assumed to have a surrounding fluid density equal to that of the tissue density and elements in black are assumed to have a surrounding fluid density equal to that of air. For brevity and clarity, only a few BC sets are shown here

Figure 9-(a) shows a sampling of the BC atlas as generated by the automatic BC generator algorithm for the displacement/stress BCs. Figure 9-(b) shows a sampling of the BC atlas for the interstitial pressure BCs.

Phantom Studies

Phantom experiments were conducted to quantify the fidelity of the constrained linear inverse model and to simulate gravity-induced brain shift. Figure 10 shows the experimental set up.

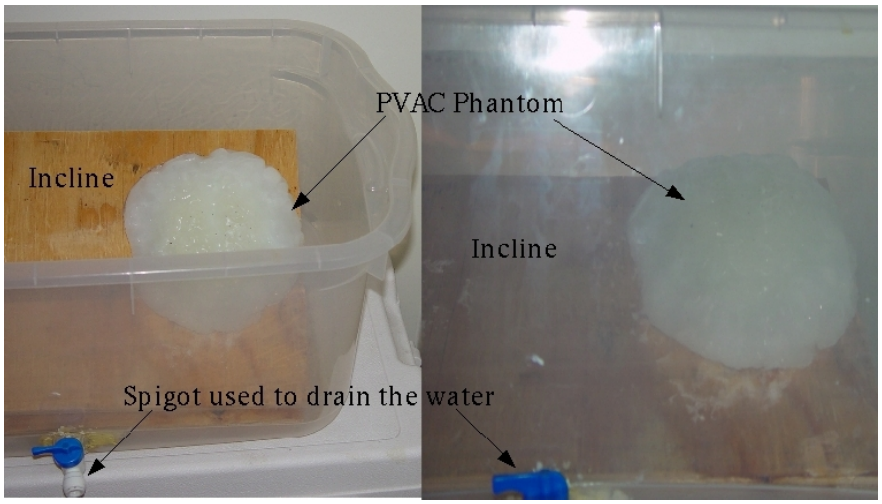

Figure 10: Phantom experiment set up used to simulate gravity induced deformations and assess the accuracy of the proposed constrained linear inverse model. For picture clarity, the tank is shown with no water in it.

The phantom was made of polyvinyl alcohol(PVA) (Flinn Scientific, Inc., Batavia IL). A 7% solution of PVA with one freeze-thaw cycle was used to construct the brain phantom. The phantom was fixed on an incline and submerged in a water-filled tank and a baseline CT scan was acquired. To simulate the loss of CSF drainage during neurosurgery, water was drained to two different levels and CT scans were acquired for each drainage level. Twelve $1mm$ diameter stainless steel bearings(http://www.bocabearings.com) were fixed on the surface of the phantom and used to track the motion of the phantom surface during all CT scans. It is worth noting the following two limitations of these phantom experiments : (i) in surgery, the brain is confined within the skull thereby constraining the brain shift, whereas no such confinements existed for the phantom, (ii) the brainstem is assumed not to shift in this framework whereas in these experiments the entire bottom surface of the brain

phantom was fixed to the incline. While the phantom experiment is not exactly analogous to surgical conditions, the goal was to simulate the scale of gravity-induced deformations in an experimental setup and validate the fidelity of the constrained linear inverse model. The CT images were acquired in a fixed experimental setup so that any discrepancies between image sets after drainage were solely due to deformation. Examples of phantom deformations can be seen in Figure 11.

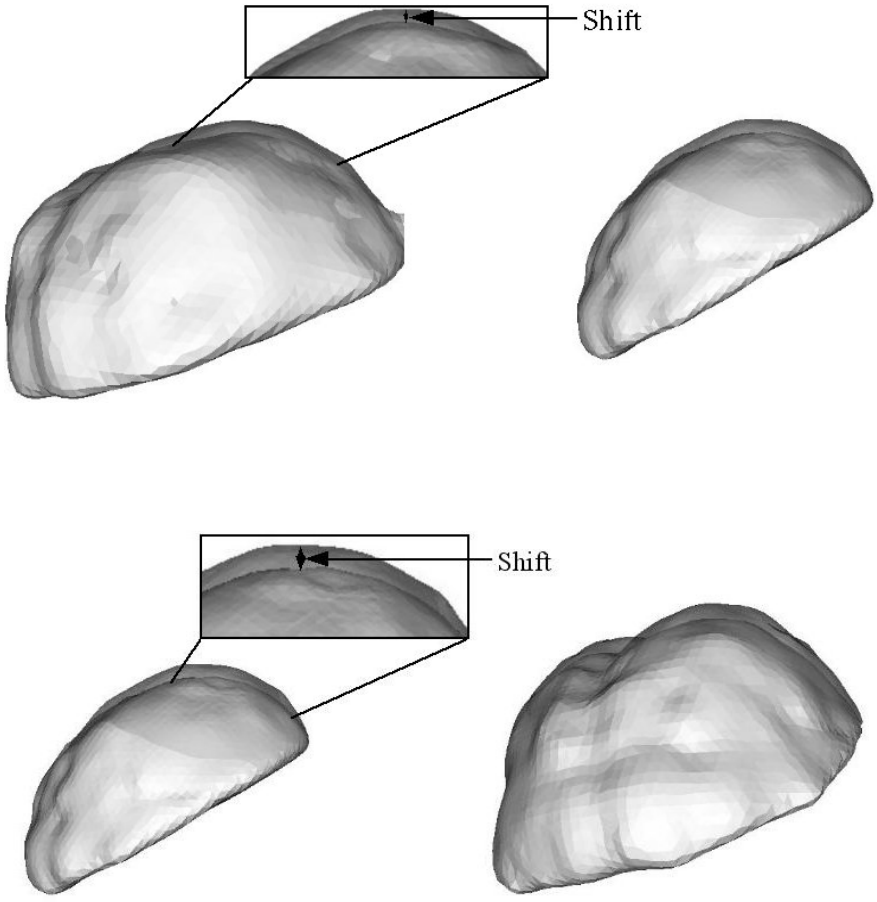

Figure 11: Phantom deformation results of the RBF surfaces of the segmented brain phantom from CT image volumes. Two different views have been shown for each water drainage level to assist in depth perception. (a) Resulting shift when water in the tank was drained to half the original level. (b) Resulting shift when water in the tank was drained to about 90% of the original level. Regions have been highlighted and zoomed in to show the shifts at a finer scale.

The starting point for the framework begins with the generation of the subject-specific model in the "preoperative" state in this case, a geometric model of the phantom in its fully submerged state. From the imaging data, a marching cubes algorithm [98] was used on the segmented CT data to generate an initial approximation of the surface of the brain phantom. FastRBF Toolbox (Farfield Technologies, http://www.farfieldtechnology.com) was then used to define a parametric version of the marching cubes surface. A tetrahedral mesh generator [99] was then used to create a volumetric tetrahedral mesh using the patch description obtained from the FastRBF toolbox. The angle of inclination was used for the phantom PPoE. Twenty-seven different orientations with 3 different drainage levels were used to create the displacement data sets/training samples using a 3D linear elastic model. Material properties used in the computational model have been reported in the Appendix. Also, the model was reduced to an isotropic elastic material model and hence Equation 13 was used with a=0. Displacements obtained using the stainless-steel bearings were used to constrain and to assess the accuracy of the constrained linear inverse model. To estimate the accuracy of the constrained linear inverse model in predicting full volume displacements, six $1mm$ stainless steel bearings implanted at a depth of 1-2cm inside the phantom were used as targets and the magnitude of target registration errors (TRE)[3] of the sub-surface bearings were examined. Additionally, displacements of the surface and the sub-surface bearings were predicted using the forward model open-loop manner to determine its accuracy with respect to modeling sag. In this case, boundary conditions i.e., drainage levels, and the inclination of the phantom were known *a priori* and therefore the gravity forces causing shift were ascertained. These forces were then applied to the computational model and the displacements were compared to those predicted using the constrained linear inverse model. Results have been presented in the following section.

[3]Target Registration Error (TRE) in this context is defined as the error between the measured shifted position and the predicted shifted position of the sub-surface bearings.

Clinical Studies

Two patients undergoing tumor resection [1, 2] were used to validate the constrained linear inverse model. In both cases, an optically tracked LRS system was used to track the cortical surfaces during neurosurgery. Upon opening the dura, the tracked LRS unit was used to capture the brain surface. After tumor resection, the process was repeated. Corresponding cortical features were identified in both scans and used as measures of displacement. Previous work has shown that serial brain shift measurements using a tracked LRS were in agreement with those measured independently by an optically tracked stylus (i.e. a *gold standard* in measurement).

Patient 1 was a 65 year old male with a history of esophageal cancer and had an associated $3cm$ area abnormal enhancement in the left frontal lobe. He underwent a stereotactic left frontal craniotomy for microsurgical resection of the tumor.

Patient 2 was a 36 year old male with a $6\times8cm$ tumor mass originating in the left frontal lobe and crossing across the midline in the corpus collosum to the collateral frontal lobe.

In each case, mannitol was administered and no initial shift was observed after opening the dura. It is important to note that the absence of initial shift post dural opening is not commonplace. Findings by Doward et al. [15], Nimsky et al. [100], and Sun et al. [88] have reported shift after opening the dura in many cases. Intraoperative cortical surfaces (after dura opening but before tumor resection, and after tumor resection) of each patient were acquired by the tracked LRS unit. Figure 12 shows the LRS surfaces overlaid on the textured preoperative MR volume.

A patient-specific model was generated for each patient. The brain, falx cerebri, tumor and edema were segmented from the patient's preoperative MR data set and the tetrahedral mesh was generated in a manner similar to the brain phantom. Tissue mechanical properties were based on previous experiences and have been reported in Appendix. For each patient, brain shift was simulated with five different atlases that reflected different assumptions about the surgical presentations of the patient: (I) tumor was assumed to be stiffer than the brain tissue [73] and was not resected from the brain volume. Mannitol was not administered

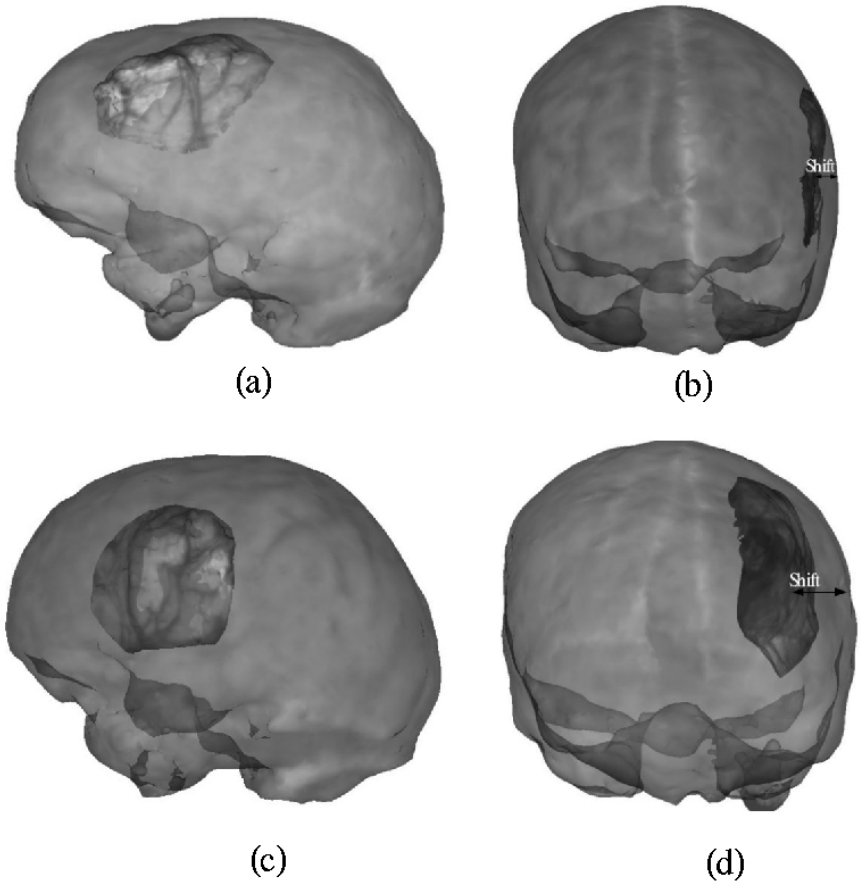

Figure 12: Pre- and Post-resection LRS surfaces overlaid on the preoperative MR volume. (a) and (b) respectively show the pre- and post-LRS surfaces overlaid on Patient 1's preoperative MR volume. (c) and (d) respectively show the pre- and post-LRS surfaces overlaid on Patient 2's preoperative MR volume. [1, 2].

and gravity was the solitary factor causing shift, (II) tumor was resected from the volume. As in the previous atlas, mannitol was not administered and gravity was the solitary factor causing shift, (III) tumor was assumed to be stiffer than the brain tissue. Mannitol was administered and was the solitary factor causing shift, and (IV) tumor was resected from the brain volume. As in the previous atlas, mannitol was the solitary factor causing brain shift (V) all four aforementioned atlases were concatenated into one large deformation atlas. Atlas I and II employed 64 different orientations with 5 different CSF drainage levels for each orientation, resulting in 320 displacement data sets/training samples for each deformation atlas for a total of 640 among Atlas I and II. Atlas III and IV used three different capillary permeability values for each of the 64 patient orientations, thus resulting in 192 displacement

data sets for each atlas for a total of 384 among Atlas III and IV. Atlas V thus consisted of 1024 deformation data sets. Tissue resection was simulated by identifying the model elements that coincide with the preoperative tumor volume and decoupling the corresponding nodes [73].

With respect to the driving sparse data, twelve corresponding points between the serial LRS scans were identified manually by an experienced user. These points are transferred to physical-space coordinates as described in the Introduction and [2]. The registration results reported in [1, 2] are used to establish correspondence between the initial LRS scan (physical-space) and the finite element mesh (image-space). Nodes on the brain surface closest to the twelve corresponding points identified on the initial LRS scan are then identified using a closest-point algorithm and these nodes are used to compute the intraoperative deformation atlas $[\mathbf{M}]$ described in the methods section. Also, the difference in position between the twelve corresponding points in physical space, i.e., the difference in physical-space coordinates between the twelve points identified on the initial LRS scan and post-resection scan, was used to constrain and validate the accuracy of the five deformation atlases using the inverse approach. Sub-surface measurements were not available for the clinical studies. Therefore, a "leave one out" technique was employed for the surface points to validate the accuracy of the constrained linear inverse model. In other words, the inverse model is challenged 12 times, each time leaving out one of the corresponding points from the intraoperative deformation atlas $[\mathbf{M}]$ and the measured shift u. Error is then computed using only the omitted point, thereby resulting in 12 error measurements for each deformation atlas. Mean, standard deviation and maximum values across these 12 error samples have been reported in the following section.

Simulation Studies

To test the fidelity of the approach in a controlled manner and to validate sub-surface shifts predicted by the inverse model, brain shift was compensated for using two different deformation atlases that reflected different assumptions about the surgical presentations of

the patient. A finite element mesh representative of a human brain was generated in a manner similar to the one used for phantom experiments. Twelve nodes on the brain surface closest to the tumor were picked to simulate the sparse intraoperative measurement points. Nodes belonging to the brain stem are fixed and in cases where tumor is resected, nodes corresponding to the tumor volume are decoupled when assembling the stiffness matrix. As a result, brain stem, tumor and measurement nodes were excluded when assessing the accuracy of the proposed framework. Shift error for all the other surface and sub-surface nodes served as unbiased error estimates and results have been presented in the following section.

Atlas I is a concatenated deformation atlas reflecting brain shift due to gravity, mannitol and tumor resection, while Atlas II additionally included shift caused by tissue swelling. It should be noted that Atlas I as defined here is analogous to Atlas V used in the clinical experiments. In order to account for the brain shift due to increased intracranial pressure from the edematous tissue, brain shift was simulated due to increased intracranial pressure using the $k_c(p - p_c)$ in Equation 14. Three different craniotomy sizes (2cm radius, 2.5cm radius and 3cm radius) were assumed and for each craniotomy size, three different edematous tissue regions were assumed. The edematous tissue was subjected to an elevated intracranial pressure of 27mmHg and three different k_c values were assumed, thus resulting in a total of 27 different scenarios. The displacement data sets resulting from these 27 scenarios were used to build the aforementioned deformation atlas II. Atlas II the concatenated deformation atlas, thus consisted of 1051 deformation data sets

Six different displacement data sets, not part of the atlases mentioned above, were used to validate the accuracy of two aforementioned atlases using the constrained linear inverse model. The forces causing shift in these different displacement sets are as follows : (A) Gravity-induced deformations with tumor *not* being resected from the tissue volume (B) Mannitol-induced shift with tumor being resected from the tissue volume (C) Brain shift resulting from tissue swelling being the solitary factor causing shift (D) Brain shift resulting from tissue swelling with mannitol being administered (E) Brain shift from tissue swelling

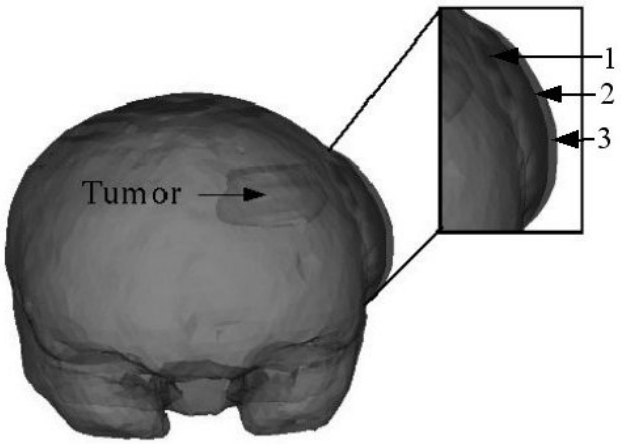

Figure 13: Two frontal views of the volume rendered brain with an increase in tissue volume simulated at the craniotomy region, simulated using two different kc values. The craniotomy region is highlighted and zoomed in to show the increase in tissue volume on a finer scale. 1 in the figure refers to the undeformed mesh. 2 refers to the increase in tissue volume simulated using k_{c1}. 3 refers to the increase in tissue volume simulated using k_{c2}. k_{c1} and k_{c2} values have been reported in the Appendix. Though the falx cerebri was modeled, it has not been shown in the figure.

with gravity-induced deformations and (F) Gravity and mannitol-induced deformations with tumor resected from the tissue volume. It should be noted that although mannitol and gravity-induced sag were used to neutralize the effect of tissue swelling in (D), and (E) respectively, the net displacements on the surface still reflected a swelled brain within the craniotomy region. Also the robustness of the constrained linear inverse model was tested by adding random noise to displacement vectors contained in Atlases I and II. The random noise level was assigned to have a maximum of 3% of a given displacement magnitude and incurred a maximum random angular error of 4°. This ensured that the perturbed displacement data sets were still contained within the atlases.

Results

Parallel implementation of the Finite Element Model

Table 3 illustrates the computational time necessary to solve the biphasic model on a finite element mesh containing 19468 nodes and 104596 elements, using 16 processors (2.8GHz,

Intel Pentium4, 1GB RAM).

No. of processors	Total time (secs)	Precondition + Iterative solution for first time step (secs)	Succesive time steps (#5) (secs)
2	853.7	154.3	623.4
4	392.2	51.7	212.5
6	202.6	32.2	117.0
8	140.0	23.9	86.0
10	138.3	23.3	85.1
12	117.5	19.0	70.5
14	130.2	16.6	81.8
16	116.7	20.7	67.5

Table 3: Computational times associated with parallel implementation of the finite element model.

With four degrees of freedom this requires the solving of a total of 77872 equations. Also the biphasic model is time dependent and a total of five time-steps were used to solve the system reported here. The second column in the table is the total computational time taken to solve the system and includes file I/O, communication across processors, stiffness matrix assembly, application of boundary conditions, and solution of the matrix system for all the five time steps. The total times reported assume the patient-specific finite element mesh has already been prepared. The third column in the table reports the time taken to precondition the matrix of equations and solve for the first time increment. The fourth column in the table reports the time required to complete all subsequent time-step calculations. The table shows that using 2 processors the total computational time required to solve the system takes 853.7 seconds and using all 16 processors it takes 116.7 seconds to solve the system.

Phantom Studies

Figure 14(a) shows the mean error between the measured and predicted shift for the phantom experiments using the constrained linear inverse model. Measured shift is defined as the displacement of the bearings as measured during subsequent CT scans.

In addition, simulation results using the model in a purely predictive mode are presented.

I and *II* in the figure represent water drainage levels of 50% and 90%, respectively. *Surface* represents the beads on the phantom surface and were used to constrain the inverse model, while *Target* is associated with the sub-surface beads that represent novel points for assessing unbiased prediction errors. Shift error refers to the magnitude error between the measured and predicted shifted positions of the bearings. Figure 14(b) shows the angular error θ, which represents the directional accuracy between the measured and the predicted shift. Averaging over both the drainage levels, the constrained linear inverse model recaptured 95.9% of the mean deformation on the surface and 88.5% of the average shift at subsurface targets while the purely predictive computational model recaptured 92% of the mean deformation on the surface and 85.3% of the average shift at subsurface targets. The formula for % shift recapture has been reported in Appendix.

Clinical studies

Figure 15(a) shows the mean shift error and the mean angular error between the predicted and the measured intraoperative brain shift for Patient 1 and Patient 2 reported in clinical experiments computed using the constrained linear inverse model. As in Figure 15(b), predicted shift error in the figure refers to the error in the magnitude between the measured and the predicted intraoperative brain shift, while angular error, θ, represents the inaccuracies in the direction of propagation. The deformation atlases used to simulate the predicted shift have been described in detail in the clinical experiments section.

In order to visualize the shift vectors predicted using the constrained linear inverse model for Patient 1, (shown in Figure 16), the measured and predicted shifts of the corresponding points were added to their respective initial positions and were projected on to the LRS surface acquired after resection. Shift vectors predicted using displacement data sets in Atlas IV were used to generate the figure shown.

Similarly for Patient 2, Figure 17 shows the measured and predicted shift vectors projected onto the LRS surface acquired after resection. Shift vectors predicted using displacement data sets in Atlas V were used to generate the figure shown.

Averaging over all five atlases for Patient 1, the constrained linear inverse model produces a mean displacement error of 0.7mm ± 0.3mm and a mean angular error of 5.8° ± 3.6° with respect to a mean cortical shift of 6.1 ± 2.4mm. Similarly for Patient 2, the constrained linear inverse model produces a mean displacement error of 0.7mm ± 0.4mm and a mean angular error of 3.2° ± 0.4° with respect to a mean cortical shift of 10.8 ± 3.7mm.

Simulation studies

As stated earlier, in the simulation studies, the constrained linear inverse model was challenged by using a deformation field that was novel to the training atlas. The six different displacement sets that were used to validate the accuracy have been presented in detail in the following section. Also noise was added to the displacement data sets in the atlas to test the robustness of the constrained linear inverse model. Figure 18 shows the mean error between the predicted and the total shift using the constrained linear inverse model for the atlases with and without the noise added to them.

Atlas I did not include tissue swelling and hence behaved poorly when challenged with displacements resulting solely due to tissue swelling, i.e., displacement data set C. It is worth noting that though the accuracy of Atlas I improved when presented with displacements resulting from a combination of tissue-swelling and gravity and mannitol-induced deformations, i.e., displacement data sets D and E, Atlas II which included the displacement data sets due to tissue swelling, significantly outperformed Atlas I. The figure also demonstrates that the constrained linear inverse model is relatively insensitive to the noise added to the displacement data sets contained in the Atlases.

As stated earlier, nodes other than the measurement nodes and the zero displacement nodes were used as targets to quantify the accuracy of the constrained linear inverse model and the shift error of these targets across the volume of the brain is shown in Figure 19. Shift predicted by Atlas II when challenged with displacement data set A was used to calcuate the shift error shown in the figure. Figure 28(a) presents the total shift at a slice passing through the tumor and Figure 19(c) shows the shift error at approximately the same slice

through the brain volume, while Figure 28(b) shows the error distribution on the surface in the vicinity of the measurement nodes. As seen in the figures, though the error increases as one moves farther away from the measurement nodes, the inverse approach performs well in the vicinity of the tumor, producing a mean shift error of 1.3 ± 0.7 mm, a mean angular error of 9.7 ± 2.3° and a maximum shift error of 2.8mm with respect to a mean shift of 5.9 ± 2.8mm and a maximum shift of 11.7mm. It should be noted that the tumor was being modeled as *not* being resected from the tissue volume. Though the figure depicts error distribution for a single displacement data set, similar error distributions were observed for all the displacement data sets that were used to validate the inverse model.

Summary of Results

To summarize the performance of the constrained linear inverse model for all the experiments reported herein, the % shift recaptured and shift error and directional error (angular error) of the constrained linear inverse model for all experiments is reported in Table 4. For a given water drainage level in the phantom experiments, the predicted surface and subsurface deformations were averaged and was used to calculate the % recapture and the shift and angular error reported in the Table. For the in vivo cases, shift predicted using Atlas V, the concatenated deformation atlas was used to calculate the amount of shift that was recaptured and the error characteristics reported here. For the simulation study, shift recapture, directional accuracy and shift error was calculated from the results of the averaged over all six distributed loading condition simulations using Atlas II.

Discussion

The integration of sparse intraoperative data into MUIGNS is not a trivial task. As stated in Miga et al.. [101], sparse intraoperative data applied in an interpolative/extrapolative sense cannot capture the entire range of deformation. They also note that the sparse intraoperative displacement data must be applied in a manner that is consistent with the forces causing those displacements. The constrained linear inverse modeling approach proposed

	Measured/Total Shift mm	% shift recaptured		Angular Error degrees	Shift Error mm
		min.	mean		
Phantom					
Level I	7.9±3.3(17.3)	91.4	91.8	4.2±2.4(6.9)	0.6±0.4(1.5)
Level II	16.3±6.8(32.3)	81.9	92.6	6.9±2.9(12.5)	1.2±0.6(5.8)
Clinical					
Patient 1	6.1±2.4(10.3)	84.4	89.4	6.0±3.8(12.6)	0.6±0.5(1.6)
Patient 2	10.8±3.7(16.3)	88.9	96.3	2.9±1.5(5.7)	0.6±0.5(1.8)
Simulation					
Atlas II	8.4±2.1(15.6±7.2)*	76.8	85.9	2.8±0.7(4.4)	1.2±0.4(3.7)

Table 4: % shift recaptured, angular error and the mean±standard deviation(max.) shift error using the deformations predicted by the constrained linear inverse model. Mean±standard deviation(maximum) of the Measured/Total shift have been reported.
* Six different displacement sets were used to constrain and test the fidelity of constrained linear inverse model. Therefore average maximum total shift and the standard deviation of the shift over the six different displacement sets has been reported.

here achieves this integration in an efficient manner. Although it may seem time consuming to build an atlas of deformations, results reported here indicate that using a multiprocessor environment significantly reduces the amount of time taken to generate atlases. As stated in Section IV, using 16 processors it takes approximately 117 seconds to calculate one basis solution/training sample in the deformation atlas. Therefore for a deformation atlas with 320 basis solutions, using 16 processors it required approximately 10 hours to build each atlas used for the clinical experiments. It should be noted that a sensitivity analysis has not been performed which may indicate that the level of detail in the atlases presented here may not be necessary to achieve meaningful shift corrections during surgery. The results here are encouraging given this relatively modest atlas; and perhaps similar results may be achieved with sparser training sets. This awaits further study.

The in vivo cases reported in this work were treated as unknown systems, i.e. the surgeon did not generate the PPoE but rather retrospective estimates based on operation notes were used. Ultimately, the PPoE will be provided by the surgeon using an ordinary graphical user interface (GUI) one day prior to the surgery. The information provided will reflect the anticipated patient orientation, craniotomy size, and location of the brain

stem in reference to the preoperative image volume. Once these have been designated, the automatic BC generation is performed to sample the possible deviations from the PPoE. This boundary condition atlas and the model is then submitted to the multi-processor cluster which returns a deformation atlas several hours later. This strategy has several distinct advantages: (1) it accounts for the uncertainty in distributed surgical loads, such as the gravitational sag and the physiological parameters like the amount of mannitol that will be administered, in a real-time sense (2) the method relies on relatively inexpensive small-scale computer clusters, (3) the time-consuming calculations are performed preoperatively, and (4) all forms of data (e.g. fMR, PET, SPECT, etc.) can be mapped within each solution and either combined through the inverse model or they can be actively computed based on the displacement fields predicted using the constrained linear inverse model. It should also be noted that the compensation for distributed loading conditions is only the first stage in this compensation strategy. The second stage is to monitor the more direct interactions such as retraction, and resection. These actions are more representative of surface loading conditions as opposed to distributed ones. We hypothesize that direct predictive modeling approaches with these should deliver the required accuracy. Previous experience with animal systems supports this tenet[72, 84]. Surface loadings resulting from tissue retraction and the resulting deformations can be modeled as a multistep process[73] and this has been demonstrated previously [72, 84, 73]. This paper represents an approach to the more difficult distributed loading conditions.

The results from the Phantom experiments are important on two distinct levels. The first level is in validating the model approximation reported by Miga et al.. for modeling brain sag [71], i.e. using the $(\rho_t - \rho_f)$g term in Equation 13. In [71], gravitational sag in four clinical cases was compensated for using this term and encouraging results were presented. The data reported in [71] used the same mechanism for simulating sag but only represent surface measurements. In the work presented here, surface and subsurface beads were tracked in a phantom under controlled gravitational loading conditions. As stated in the results section, the computational model recaptured approximately 88.7% of the surface

and subsurface shift. The second level of significance for the phantom experiments is in validating the proposed constrained linear inverse model approach for distributed surgical loads. Table 4 indicates an approximate 92% compensation capability when only using sparse surface data to guide the inverse model. One interesting aspect to observe in the phantom results is that the constrained linear inverse model outperformed the forward-based computational model that used the known boundary conditions. Undoubtedly the inaccuracies in the forward model are from inappropriate small-strain approximations, nonlinear material effects. Despite these inaccuracies and the lack of explicit drainage/incline information, the constrained linear inverse model delivered a modest improvement over the computational model by synthesizing a better match through the combination of a simpler pre-computed set of model basis solutions.

For the clinical studies, it was interesting to note that in both the patient cases, the atlas with mannitol-induced deformations recaptured most of the measured shift. Atlas III, mannitol-induced deformations with non-resected tumor recaptured most of the shift for Patient 1, while for Patient 2, Atlas IV, mannitol-induced deformations with resected tumor recaptured most of the measured shift. While no statistical significance can be inferred, it is interesting that mannitol was administered in both patients and that when comparing the results among the atlas', the predictions by mannitol induced shift are better than the gravity-induced shift. Although anecdotal, this may suggest that mannitol-induced shift may have a more prominent role in compensation strategies than previously reported. While these thoughts are intriguing, unfortunately, more detailed validation with subsurface measurements in a bigger patient population will be required to assert any conclusions. Nevertheless, the results among the experiments are markedly consistent and indicate that the constrained linear inverse modeling approach is a viable method for the compensation of distributed loading conditions.

The simulation results concerned with brain swelling were of comparable accuracy to the phantom and clinical experiments. In addition, the reported swelling shift magnitudes were comparable to those found in the literature [15, 100, 88]. One common criticism of

the MUIGNS systems is that tissue swelling cannot be accounted for. Initial results of the sensitivity of the inverse model to noise (as shown in Figure 18) shows that the model is relatively insensitive to noise, as long as the displacement data are still contained by the atlas. The results shown here suggest that swelling conditions encountered in the OR can be simulated using computer models. Figure 19(c) shows the distribution of the shift error recaptured in the tumor region. Though the error increased when compared to the error distributions on the surface containing the measurement nodes (shown in Figure 28(b)), the constrained linear inverse model still recaptured 83.6% of the mean shift in the vicinity of the tumor. These results combined with the target/sub-surface validations from the phantom experiments suggest that the constrained linear inverse model is a good framework for predicting sub-surface displacements using sparse intraoperative measurements.

While the work presented here is encouraging, the following issues need to be addressed before implementing this approach in a MUIGNS system: (i) more detailed validations with intraoperative imaging modalities such that the accuracy of the technique in predicting full volume displacements can be achieved; though validating the accuracy of the model has been reserved for a future study, the phantom results shown here and the simulation study results reported in [89] suggest that the model will behave in a similar fashion when predicting full volume displacement fields from sparse intraoperative data; (ii) sensitivity analysis of the inverse model to the particular selection of the boundary conditions and the consistency of the atlas; (iii) more detailed understanding of the internal structures affecting brain shift, e.g. the falx cerebri has been shown to inhibit cross-hemisphere movement; (iv) new studies focused on the improvement from subsurface data such as from co-registered ultrasound; and, (v) more studies regarding the sensitivity of the methods to the number and spatial distribution of sparse intraoperative data points. With respect to this last point, the results presented here have yielded a potentially important finding. In both the phantom and clinical experiments, the constrained linear inverse model was guided with a relatively modest number of points (12-15 points) spatially distributed on the area of observation. The level of model-fit in these cases is remarkable and makes it evident that assumptions

regarding the extent, i.e. amount of data necessary for model-updating can and should be challenged as these new systems are developed.

Previous work has demonstrated that modeling can predict deformations induced by surface loading conditions such as tissue retraction [72, 73]. Although detailed clinical studies have not been presented, the results suggest that the inverse model has the capability to predict intraoperative brain shift resulting from distributed loading conditions. These preliminary results indicate that the inverse model when combined with the approach reported in [72, 73] has the ability to predict intraoperative brain shift resulting from surface loads and distributed loads, thereby completing the MUIGNS framework.

Conclusions

In is interesting to note early reports dismissing methodologies to correct for intraoperative shift that did not involve traditional intraoperative imaging (specifically, iMR, and iCT) [102]. These early reports believed that conditions such as swelling and brain volume changes due to hyperosmotic drugs could not be predicted or practically modeled. In the experiences shown here and by others, these conclusions continue to be challenged and the potential for computer modeling within the OR environment is only now being realized. There is a growing acceptance that predicting brain shift at scales relevant to surgical interventions through computer models is very possible when proper approximations to forcing conditions are understood and when sufficient data is present to guide predictions. Albeit for surface displacements, the results presented in this work show that with a good set of basis-solutions/training-samples, the constrained linear inverse model can be used to predict cortical shift. In future work, the accuracy of this approach in predicting full volume displacement fields from sparse intraoperative data sets will be achieved using a comprehensive digitization approach. Further approach enhancements are being pursued and will include more anatomical constraint information and possibly a non-linear optimization framework.

Acknowledgements

This work was supported by the NIH-National Institute for Neurological Disorders and Stroke - Grant # R01 NS049251-01A1. The authors would also like to thank Dr. Tuhin K. Sinha and Dr. Philip Q. Bao [4], for their assistance in data processing. The authors would also like to thank Jao J. Ou and Logan W. Clements for their help in phantom experiments. The authors would also like to thank the PETSc maintenance staff for their assistance with the parallelization of the computational model. Most of the visualization was performed using Visualization ToolKit (http://www.vtk.org).

[4]Vanderbilt Department of Surgery

Appendix

The symbols used for the material properties have been described in the methods section.

Material Properties used for the Phantom Experiments

Symbol	Value	Units
E	1875	N/m^2
ν	0.45	(no units)
$G = \frac{E}{2(1+\nu)}$		

Material Properties used for the in vivo and simulation studies

Symbol	Value	Units
E,white and gray	2100	N/m^2
E,tumor	100000	N/m^2
E, falx	210000	N/m^2
ν	0.45	(no units)
ρ_t	1000	kg/m^3
ρ_f	1000	kg/m^3
g	9.81	m/s^2
a	1.0	(no units)
$1/S$	0.0	(no units)
k_{white}	1x10^{-10}	m^3s/kg
k_{gray}	5x10^{-12}	m^3s/kg
$k_{c1}, white^*$	9.2x10^{-9}	Pa/s
$k_{c2}, white^*$	4.6x10^{-9}	Pa/s
$k_{c3}, white^*$	2.3x10^{-9}	Pa/s
$k_{c1}, gray^*$	45.9x10^{-9}	Pa/s
$k_{c2}, gray^*$	22.9x10^{-9}	Pa/s
$k_{c3}, gray^*$	11.5x10^{-9}	Pa/s

p_c, mannitol	-3633	Pa
p_c, swelling	3633	Pa

* 3 different values used for the simulation experiments in to simulate tissue swelling due to elevated intracranial pressures.

Shift Recapture

$$\% \, shift \, recapture = (1 - \frac{shift \, error}{total \, shift}) \, * 100$$

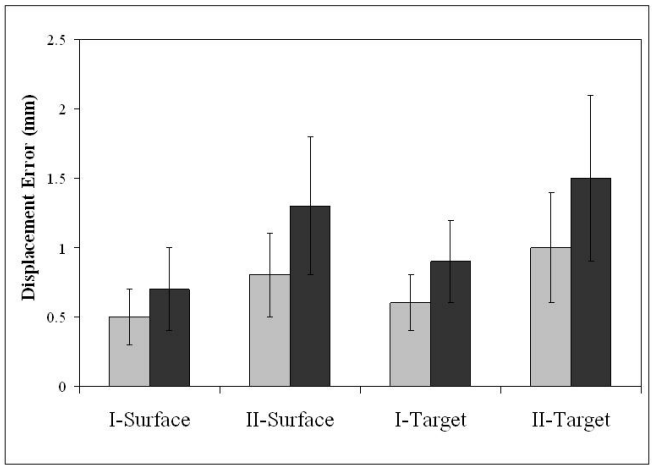

(a)

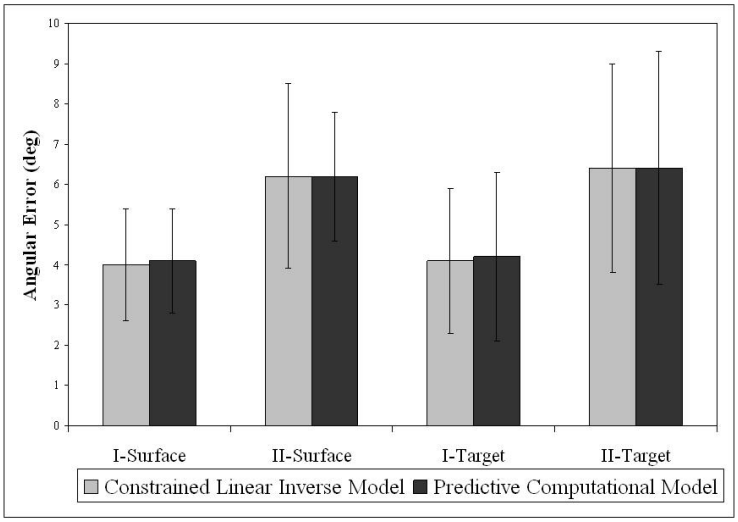

(b)

Figure 14: Phantom Experiment Results. (a) Mean Shift error in *mm*, between the measured and predicted shift. Measured shift is defined as the displacement of the bearings as measured during subsequent CT scans. (b) Mean Angular(θ) Error in *degrees* between the measured and predicted shift. *I* and *II* represent water drainage levels of 50% and 90% respectively. *Surface* represents displacements of the bearings fixed on the phantom surface and were used to constrain the inverse model whereas *Target* represents the displacements of bearings implanted inside the phantom and were used as unbiased error estimators.
The average measured surface shift of the phantom was 10.1±4.5mm, and 21.2±9.3mm for drainage conditions I, and II respectively. The average measured target shift of the phantom was 5.6±2.1mm, and 11.3±4.3mm for drainage conditions I, and II respectively.

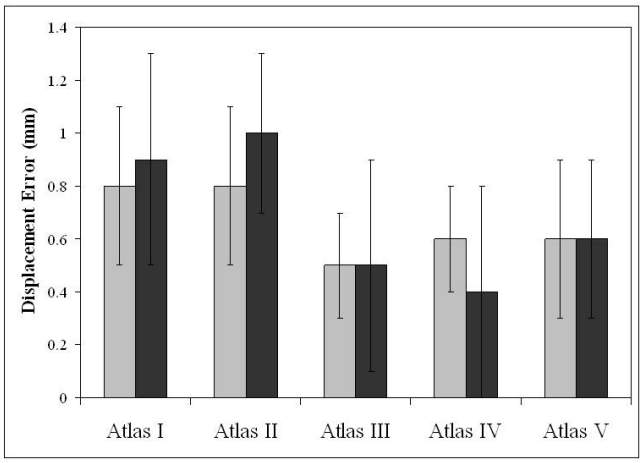

(a)

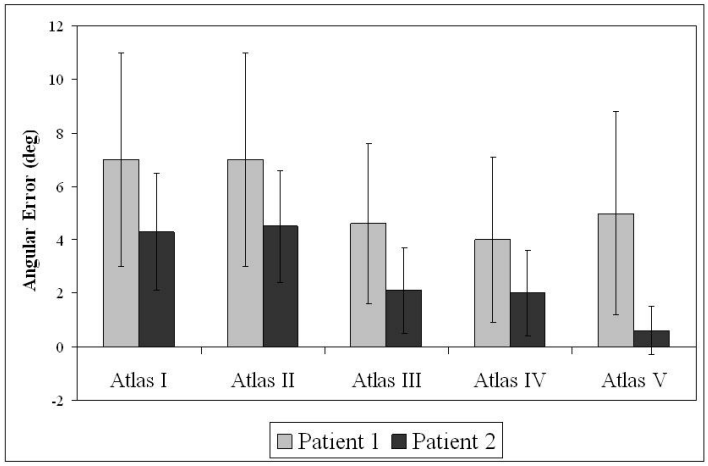

(b)

Figure 15: Patient 1 and 2 Results. (a) Mean Shift error between the measured and predicted shift. Measured Shift for *Patient 1* : 6.1±2.4mm with a maximum displacement of 10.3mm. Measured Shift for *Patient 2* : 10.8±3.7mm with a maximum displacement of 16.3mm. (b) Mean Angular(θ) Error in *degrees* between the measured and predicted shift.
Atlas I : Tumor was not resected from the brain volume and gravity was the solitary shift-causing factor. Atlas II : Tumor was resected from the brain volume and gravity was the solitary shift-causing factor. Atlas III : Tumor was not resected from the brain volume and mannitol was the solitary shift-causing factor. Atlas IV : Tumor was resected from the brain volume and mannitol was the solitary shift-causing factor. Atlas V : All four aforementioned atlases were concatenated into one deformation atlas.

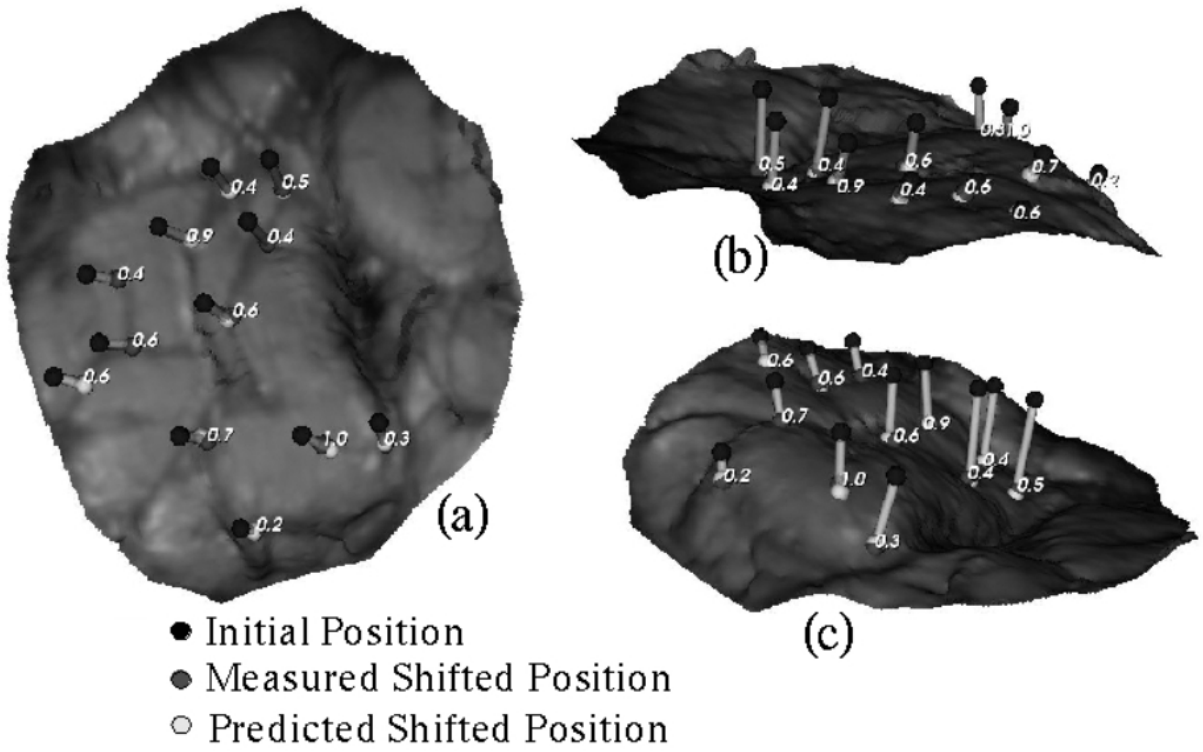

Figure 16: Measured and shift vectors predicted using the constrained linear inverse model (shown as line segments) overlaid on the post-resection LRS surface for Patient 1. Shift predicted using Atlas IV (mannitol being the solitary shift causing factor, tumor resected from the tissue volume) has been shown here. The numbers in the figures represent the absolute error between the measured and predicted shift. Each figure, (a), (b) and (c) demonstrates the overlay from a different camera angle to assist with depth perception.

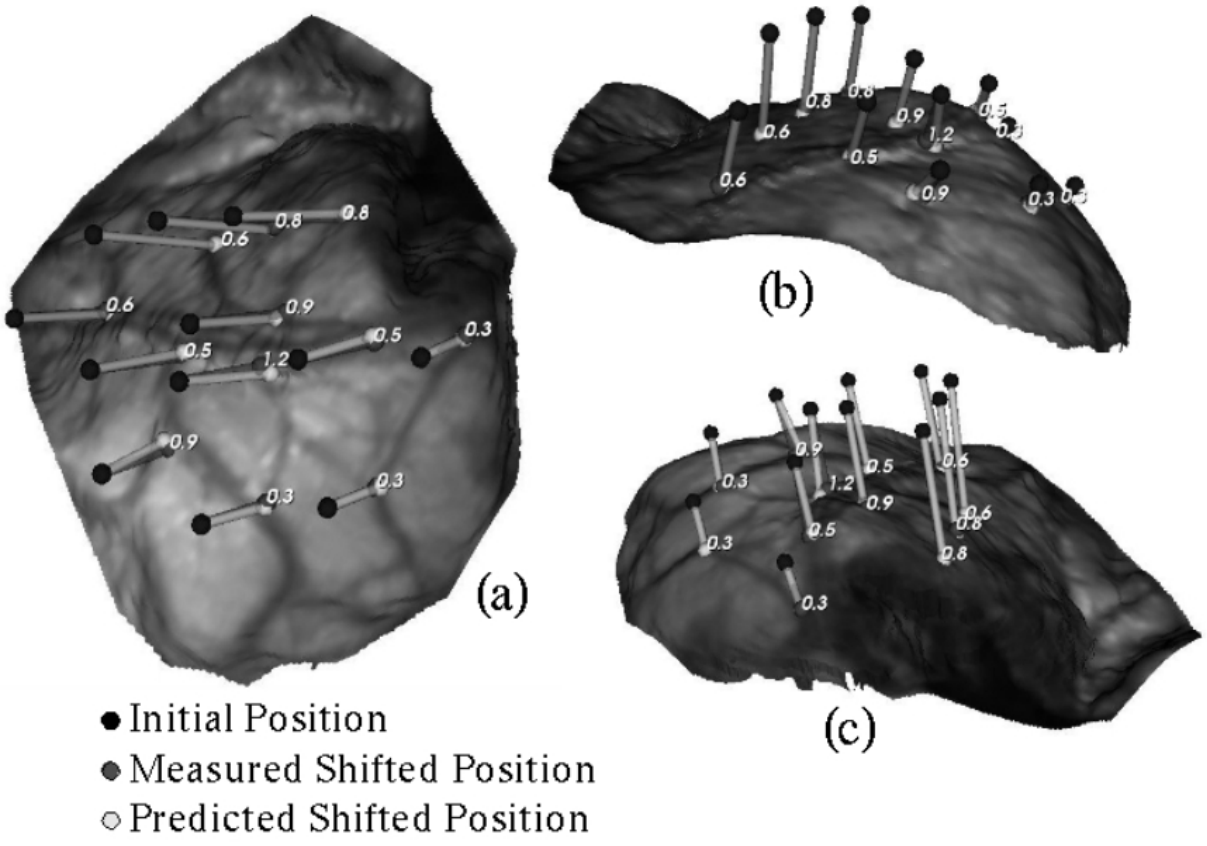

Figure 17: Measured and shift vectors predicted using the constrained linear inverse model (shown as line segments) overlaid on the post-resection LRS surface for Patient 2. Shift predicted using Atlas V (concatenated deformation atlas) has been shown here. The numbers in the figures represent the absolute error between the measured and predicted shift. Each figure (a), (b) and (c), demonstrates the overlay from a different camera angle to assist with depth perception.

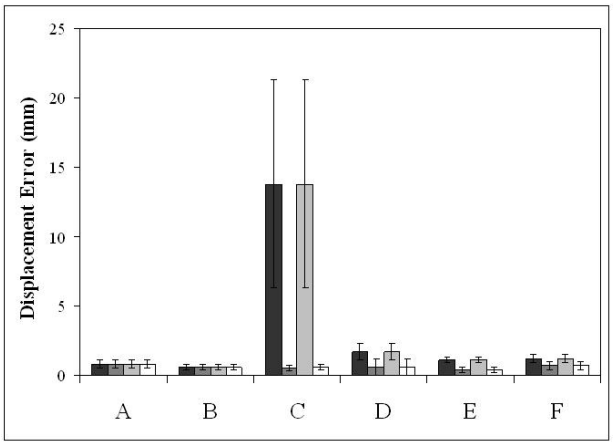

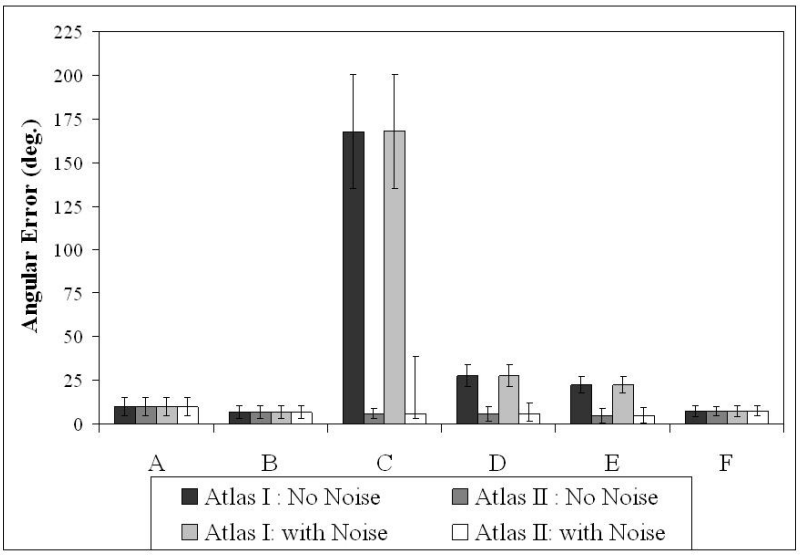

Figure 18: Simulation Study Results. (a) Mean Shift error between the total and predicted shift. (b) Angular Error between measured and predicted shift. Atlas I is a concatenated deformation atlas reflecting brain shift due to gravity, mannitol and tumor resection, while Atlas II additionally included shift caused by tissue swelling. Detailed description of the figure can be found in the manuscript.

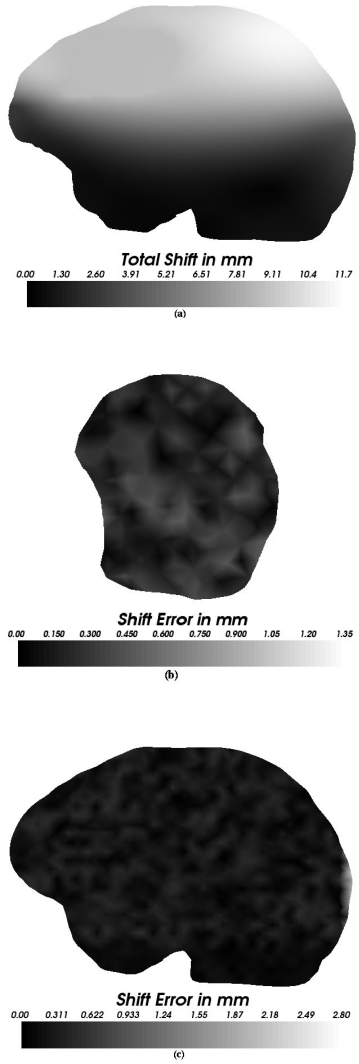

Figure 19: Shift error computed using Atlas II when challenged with the displacement data set A. (a) Magnitudes of the shift in mm, for a slice passing through the tumor (b) Shift (magnitude) error at the surface in the vicinity of the measurement nodes (c) Shift (magnitude) error at approximately the same slice as (a).

CHAPTER V

MANUSCRIPT 3 - A fast and efficient method to compensate for brain shift during surgery

Abstract

Objective: To present a methodology that predicts brain shift on a time frame that is compatible with tumor resection therapies.

Methods: A priori knowledge of the possible sources of brain shift has been shown to increase the accuracy of model-updated image-guided systems. Therefore the computational model is run multiple times in a forward manner to account for all possible sources of deformation and these model solutions are combined linearly using an inverse model to predict the distributed shift. This simple linear inverse model is investigated within the context of 8 patients.

Results: The proposed framework recaptures 85% of the mean sub-surface shift. This translates to a sub-surface shift error of 0.4mm±0.1mm for a measured shift of 3.1mm±0.6mm. The patient's preoperative tomograms are deformed using the volumetric displacements predicted using the proposed framework and results are also presented in a qualitative fashion as difference images between these image volumes and the postoperative tomograms.

CONCLUSION: This study demonstrates the accuracy of the proposed framework in predicting full volume displacements from sparse shift measurements. It also shows that the proposed framework can be used to update preoperative images on a time scale that is compatible with surgery.

Introduction

Image-guided surgical systems rely on establishing a relationship between the physical space in the operating room (OR) and the patient's preoperative image tomograms. Tissue deformation and shift that occurs during neurosurgery during removal of a tumor

results in a loss of the aforementioned spatial relation thereby compromising the accuracy of neruonavigation-based procedures. Reports have indicated that the brain can deform a centimeter or more in a non-uniform fashion throughout the brain [10] and that brain shift occurs due to a variety of reasons including pharmacologic responses, gravity, edema, hyperosmotic drugs and pathology [100, 9, 7]. In an effort to compensate for intraoperative brain shift, researchers have used techniques ranging from intraoperative image-guided surgery [25, 100, 83] to model-updated image-guided surgery (MUIGS) [50]. Intraoperative image-guided systems have been predominantly limited to intraoperative magnetic resonance (iMR) imaging and intraoperative ultrasonography (iUS). While iMR techniques have been labeled cumbersome and have been questioned for their cost-effectiveness, the images produced by iUS systems lack the same clarity as their iMR counterparts. Therefore in their current state, intraoperative imaging systems do not present a complete solution for brain shift. As a cost-effective and efficient method computational models have been used successfully in MUIGS to correct for intraoperative brain shift.

Typically a patient-specific model is used in MUIGS, thereby taking advantage of the high-resolution preoperative images. This model is used to deform the patient's preoperative images to display the current intraoperative position and the displacements predicted by the computational model are used to deform the preoperative images. Invariably, the computational model is a critical component of any MUIGS system and a spectrum of computational models ranging from less physically plausible but very fast models through to extremely accurate biomechanical models requiring hours of compute time to solve have been presented in the literature [51, 52, 53, 54, 55, 56]. Warfield et al. [57] were among the first to demonstrate that computational models can be used in a time frame that is consistent with the demands of neurosurgery. The results reported in [57, 103] are encouraging and suggest that more complex models can be used in MUIGS. Another critical component of MUIGS is the integration of sparse intraoperative data which serves to control the computational model. Sparse, in this context, means data with limited information and/or spatial extent. The integration of sparse intraoperative data should not only increase the accuracy of the

system but it should also meet the real time constraints of neurosurgery. Towards this end, we reported a framework [103] that combined a computational model with a linear inverse model and was used to predict intraoperative brain shift. In this framework, a series of model deformations based on complex loading conditions such as brain shift due to gravity, volume changes due to drug reactions, tissue swelling due to edema was computed preoperatively and these model solutions were used to construct an atlas of deformations. Sparse intraoperative surface measurements were then used to constrain the model and volumetric brain shift was predicted using a linear inverse model. The computational model and the inverse model have been discussed in brief in the following section. This framework was investigated within a series of phantom experiments, two in-vivo cases and a simulation study. Results reported in [103] indicated that the framework recaptured on an average 93% of surface shift for all the experiments and 85% of the subsurface shift for the phantom and simulation experiments. Sub-surface shift measurements were not available for the two in-vivo cases that were reported in [103].

In the work presented here, we use the aforementioned framework to validate sub-surface shift measurements in 8 in-vivo cases. More specifically, surface and sub-surface shift measurements were obtained by registering postoperative magnetic resonance (MR) tomograms to the patient's preoperative MR tomograms. Patient-specific models and deformation atlases were generated for each of the 8 cases and sub-surface shifts predicted by the combined linear inverse and computational model were validated against the measured shift. Shift error and Angular error between the measured and predicted positions of the sub-surface points have been presented in Section 4. Also, the patient's preoperative MR image volumes were deformed using the volumetric shift predicted using the inverse model and qualitative comparisons with the postoperative MR image volumes have been presented in the results section.

Systematic studies have shown that the accuracy of brain shift models can be increased by integrating feedback from sparse intraoperative data [50]. A schematic of model-updated image-guided neurosurgery (MUIGNS) is shown in Figure 20. As seen in the figure, the computational model and the integration of sparse intraoperative data with the model are two important features of a MUIGNS system and these have been discussed in brief below.

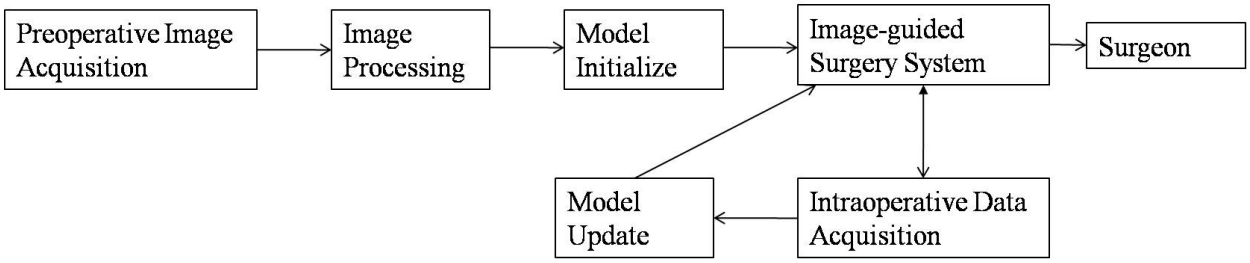

Figure 20: Schematic for Model-Updated Image-guided Neurosurgery (MUIGNS).

Computational Model

Hakim et al. [66] showed that the transmission of intraventricular pressure throughout the brain parenchyma created a stress distribution that varied in magnitude and direction and made the observation that the "brain acts like a sponge". Doczi [67] reported that the gray matter and white matter can increase their fluid content due to the difference in vascular availability and also pointed out that when the blood brain barrier is compromised interstitial pressure drives the fluid movement in the brain. These findings highlight the need for a fluid compartment in the model. In light of this fact, David Roberts and his research group at Dartmouth [70, 71]developed a 3D computational model based on Biot's theory of soil consolidation. In short Biot's consolidation theory [68] gives a general description of the mechanical behaviour of a poroelastic medium [1] based on equations of linear elasticity for the solid matrix and Darcy's law for the flow of fluid through the porous matrix. According to this model, the brain is biphasic in nature and the volumetric strain rate depends on the

[1] A porous medium is one where a solid matrix is permeated by an interconnected network of pores filled with a fluid.

changes in interstitial pressure and hydration. Extensive validation studies have been conducted by the group at Dartmouth [104, 71, 84, 73]. They reported that the computational model can capture 70% to 80% of the subsurface deformation in animal experiments.

Figure 21 shows the template boundary condition (BC) set used for predicting brain shift due to gravity-induced deformations. Surface 1 is assumed to be stress-free. i.e., free to deform. Surfaces 3 and 4 (the brain stem region) is fixed for displacements, i.e., they do not move and Surfaces 2 and 5 are permitted to move along the cranial wall. The amount of intraoperative cerebrospinal fluid (CSF) drainage is assumed for each patient orientation and this level determines the drainage or the pressure boundary conditions in the model. Parts of the brain above the CSF drainage level are assumed to reside at atmospheric pressure and parts below it do not allow fluid drainage. It should be noted that the boundary condition template shown in the figure is patient-specific and depends on the patient's head orientation in the operating room (OR).

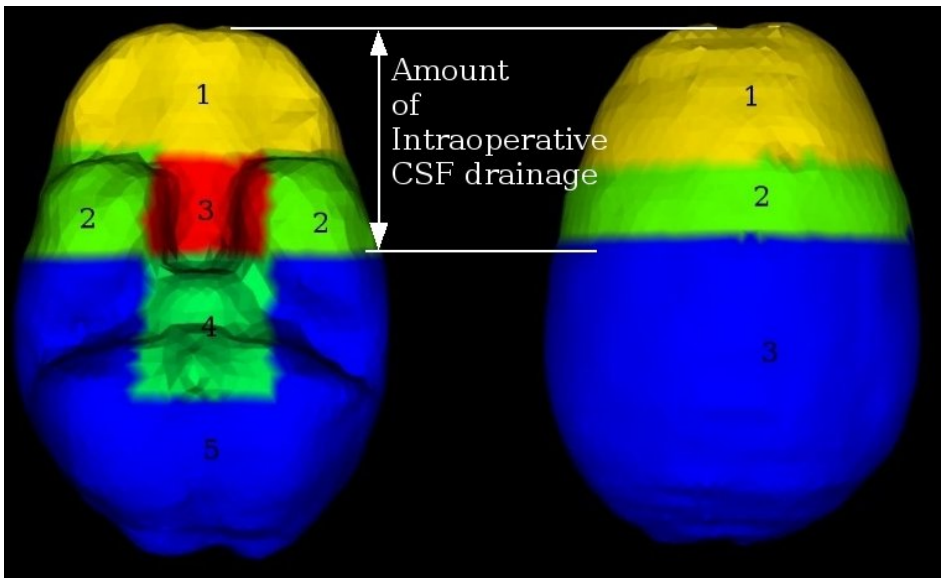

Figure 21: Boundary condition (BC) template set for a supine patient with neutral head orientation in the OR. Displacement BCs: Surface 1: Stress-free , i.e., free to deform, Surface 2 and 5: move along the cranial wall, Surfaces 3,4 and 5: Fixed, i.e., cannot move. Pressure BCs: Surfaces 1, 2 and 3 reside at atmospheric pressure, Surfaces 4 and 5 are still submerged in CSF and therefore do not allow fluid drainage.

Inverse Model

It can be difficult to determine brain shift within the OR environment using the computational model. For example, when predicting gravity-induced brain deformations, the patient head orientation and the amount of intraopreative CSF drainage must be ascertained. The surgeon's preoperative plan can be used to approximate the patient's orientation in the OR, but it is difficult to measure the amount of fluid drainage. Also, in cases where mannitol is administered it is difficult to differentiate the shift due to mannitol and gravity. In order to account for this degree of uncertainty associated with the computational model, the computational model is run multiple times to account for all possible sources of intraoperative deformation. For example, a range of patient orientations/surgical presentations is assumed based on the preoperative plan and for each orientation a range of fluid drainage levels are assumed. Boundary conditions are generated for each surgical presentation and deformation solutions are predicted using the computational model. These solutions are then assembled in a matrix **E**, also referred to as the deformation atlas. In a similar fashion, deformation atlases due to hyperosmotic drugs such as mannitol and tissue swelling due to edema can be generated. The deformation atlas **E** is of size (n x 3) x m, where n is the number of nodes in the finite element mesh and m the number of model solutions. As noted above, the measurements are not obtained for all points in the brain and therefore the model solutions within **E** are interpolated to the specific measurement points and these interpolated solutions are assembled in the intraoperative deformation atlas, **M**. **M** is of size (n_s x 3) x m, where n_s is the number of sparse measurement points. The interpolated model solutions in **M** serve as training samples for the inverse model which is given below:

$$G_{sparse}(\alpha) = ([\mathbf{M}]\{\alpha\} - \{u\})^T([\mathbf{M}]\{\alpha\} - \{u\}) + \phi[W]^T\{\Upsilon\}\{\alpha\} \tag{22}$$

where U is the sparse measured shift, **W** the weighting vector, υ is the strain energy matrix and α the regression coefficients. The first term in the equation serves to minimize the error between the predicted model solutions and measured shift, while the second term

minimizes the elastic energy across the deformation atlas and produces a spatially smooth displacement field. The vector of regression coefficients are determined from the above equation and intraoperative brain shift is calculated using [E]α. It should be noted that all the deformation atlases are computed preoperatively. The measured sparse data then act as control points and are used to constrain the inverse model and sub-surface points are used as unbiased error estimates to validate the accuracy of volumetric brain shift predicted by the model. The inverse model is a direct solution and therefore the framework should meet the real time constraints of neurosurgery. A more detailed description of the inverse model can be found in [103].

Image Updating

The last and an equally important step in a MUIGNS framework is the updating of preoperative images based on the volumetric brain shift predicted by the combined computational and linear inverse model. Since the finite element mesh for each patient is built using the patient's preoperative images and the displacements predicted by the linear inverse model are defined in a continuum manner over the finite element mesh, these displacements can be used to deform the preoperative images. An image-updating algorithm was initially presented in [71]. In [71], Miga et al.. used a backcasting technique to deform the patient's preoperative images using displacements predicted by the model. We parallelized this image-deformation algorithm in order to meet the real time constraints of neurosurgery. This algorithm eliminates the problem of holes/tears in the updated image, produces a contiguously deformed image that is based on the governing equations for the forward model and translates the volumetric brain shift predicted by the model into images that can be recognized by the neurosurgeon. Figure 22 shows a schematic of the image-updating algorithm used in this framework.

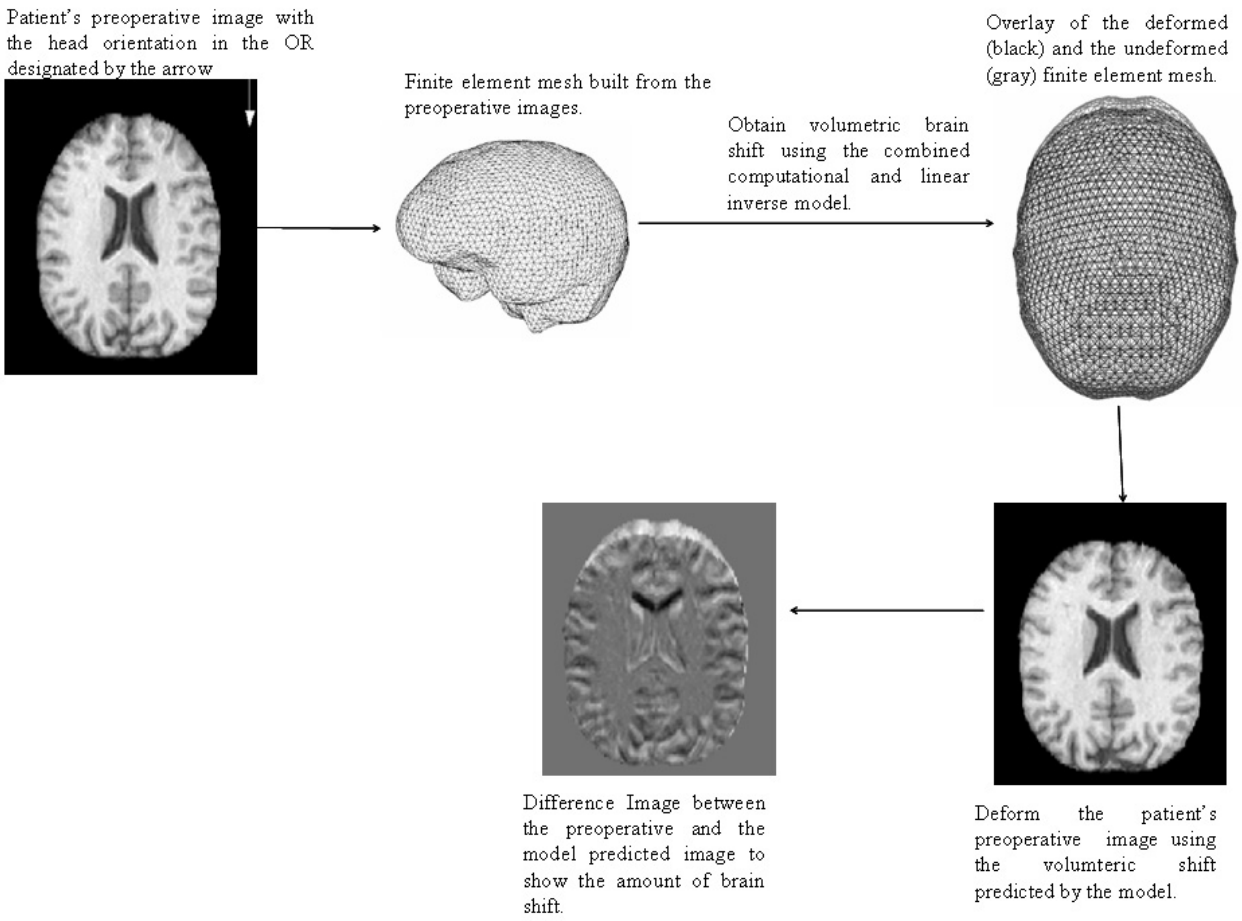

Figure 22: Image-updating algorithm based on volumetric brain shift predicted by the combined computational and linear inverse model.

Illustrative Cases

8 patients (mean age of 51.4yrs with 2 men) with brain tumors (primary or metastatic) were included in this study (shown in Table 1). All patients were enrolled after obtaining written informed consent for participation in this study, which was approved by the Institutional Review Board of the Vanderbilt University School of Medicine. After anesthetic induction, the patients were positioned on the operating room table and were secured to the table using a Mayfield clamp. All patients received diuretics (mannitol, 0.5-1.0 g/kg) and steroids (dexamethasone) immediately before incision. All patients underwent craniotomy for tumor resection and no side effects related to participating in this study were noted. Preoperative and postoperative MR tomograms were acquired as 1.5T, T1-weighted, 3D-

Pt. #	Age, /Sex	Tumor Type	Craniotomy (diameter) (cm)	Orientation (deg)	Location	Lesion size (cm)
1	22,F	Gr(II) Olig.	7.7	IS 90d rot	L,F	5.2x6.2x6.0
2	52,M	Astro.	8.3	IS 90d rot	L,F	4.9x5.6x5.0
3	60,F	Mening.	5.5	IS 90d rot	R,F/T	4.5x6.4x4.3
4	77,M	Gr(IV) GBM	5.0	IS 90d rot.	L, T	3.4x3.6x2.0
5	56,F	Met.	4.5	-	L,F	4.7x3.2x4.0
6	75,F	Gr(II) GBM	6.1	IS 15d rot	L,T	5.0x5.0x5.0
7	23,F	Gr(II) Astro.	6.4	Neutral	R,F	4.0x3.0x3.0
8	46,F	Gr(IV)GBM	4.3	IS90d rot.	R,T	3.0x3.0x3.0

Table 5: Patient Information. Tumor Types: Gr - Grade, Olig. - Oligodendroglioma, Mening. - Meningioma, Asto. - Astrocytoma, GBM - Glioblastoma Multiforme, Met. - Metastatic Tumor. Orientation: IS - refers to rotation about inferior-superior axis (e.g., IS 90d rot reflects patient's head parallel to the OR floor). Location: L:left, R: right, F:frontal, T: temporal, P:parietal.

SPGR, 1x1x1.2mm voxel, gadolinium-enhanced and non-enhanced image volumes. It should be noted that the preoperative image volumes were acquired a day before or on the morning of the surgery and the postoperative images were acquired a day after surgery. The preoperative and postoperative MR volumes were registered using mutual information registration algorithms developed at Vanderbilt [105].

The brain region is then segmented from these registered volumes using an atlas based segmentation method [106]. Textured brain surfaces are generated from these segmented MR tomograms and corresponding cortical features (vessel bifurcations, sulcal and gyri patterns) identified manually on these surfaces are used as measures of brain shift. A patient-specific model was generated for each patient. The brain and falx cerebri, tumor and edema were segmented from the patient's preoperative MR data set and the tetrahedral mesh was generated in a manner similar to the one reported in [103]. For each patient, brain shift was simulated with four different atlases that reflected different assumptions about the surgical presentations of the patient: (I) Tumor was resected from the brain. Mannitol was not administered and gravity was the solitary factor causing shift, (II) Tumor was resected from the brain. Mannitol was administered and was the solitary factor causing shift, (III) Tumor was present and shift was induced by tissue swelling in the tumor and edematous region and

with mannitol being administered to the patient, and (IV) all three aforementioned atlases were concatenated into one large deformation atlas. Atlas I employed 60 different patient orientations with 4 levels of intraoperative CSF drainage for each orientation, resulting in 240 displacement solutions in Atlas I. Atlas II used three different capillary permeability values for each of the 60 patient orientations, thus resulting in a total of 180 different displacement solutions. In order to simulate displacement solutions for Atlas III, three different craniotomy sizes were assumed and for each craniotomy size, three different edematous tissue regions were assumed. For each edematous region, three different capillary permeability values and three different intracranial pressures were assumed. This resulted in a total of 81 different scenarios. Atlas IV thus consisted of 501 deformation data sets. With respect to the driving sparse data, twelve to fifteen corresponding points were identified manually for each patient between the registered textured brain surfaces.

Differences in position between the postoperative and preoperative corresponding points were used as measures of brain shift and these displacements were used to constrain the inverse model. Nodes on the finite element mesh corresponding to these points are identified using a closest point algorithm and these nodes were used to compute the intraoperative deformation atlas. Also, six to eight corresponding sub-surface points were identified on the registered MR tomograms and these points were used to validate sub-surface shifts predicted by the inverse model. Given the uncertainties in measurements due to segmentation and registration errors surface shifts lesser than 3mm and sub-surface shifts lesser than 2mm were not included in this study and the sub-surface points were spatially distributed over the entire brain volume. Figure 23 shows the surface and sub-surface points for Patient 1 used in this study. It should be noted that the surface points were used to constrain the inverse model and the sub-surface points served as unbiased error estimates. Also, the sub-surface points shown in the figure are not co-planar, but are distributed over the entire brain volume.

Shift error which refers to the magnitude error between the measured and predicted shifted positions of the sub-surface points and angular error which refers to the directional

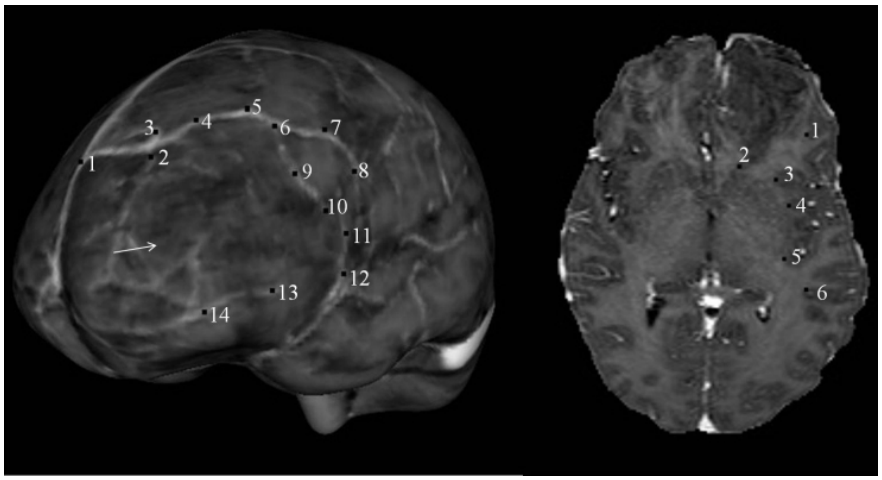

Figure 23: Surface (left) and sub-surface (right) points for Patient 1 that were used in the model. The arrow in the surface point distribution figure (left) points to the location of the tumor. Sub-surface points 1 and 2 are located superior (at a higher elevation) to the tumor, points 3,4 and 5 were located in plane with the tumor and point 6 is located inferior to the tumor. Surface points were used to constrain the linear inverse model and sub-surface points were used to validate the accuracy of the the model.

accuracy between the measured and predicted shifted positions of the sub-surface points have been presented in the following section. Also, the patient's preoperative MR image volumes were deformed using the volumetric shift predicted using the inverse model and qualitative comparisons with the postoperative MR image volumes have been presented in the following section.

Results

Anatomical fiducials (such as ear lobes, eye sockets, and corresponding points in the brain stem region) were chosen between the preoperative and postoperative MR tomograms to assess the accuracy of the mutual information algorithms that were used to register these image volumes. The mean difference in position between these points was found to be 1.0±0.3mm. It should be noted that this does not represent a registration error and detailed error analyses of the algorithms can be found in [105].

Shift Error predicted using the linear inverse model for all eight patients has been reported in Table 6. The second and third columns in Table 6 represent the measured shift for surface and sub-surface points obtained using the registered preoperative and postoperative

MR volumes. It should be noted that the surface shift was used to drive/constrain the inverse model and the sub-surface points served as unbiased error estimates. As shown in the table, Atlas IV the concatenated deformation atlas performed the best for all eight patients. Averaging over all eight patients, using Atlas IV the constrained linear inverse model produced a mean shift error of 0.4±0.1mm and a mean angular error of 9.5±1.1° with respect to a mean sub-surface shift of 3.1±0.6mm.

% shift recaptured with the constrained linear inverse model using Atlas IV has been reported in Table 7. Averaging over all eight patients, the constrained linear inverse model recaptured 85% of the mean measured sub-surface shift.

A "leave one out" technique was also employed for the surface and sub-surface points to validate the accuracy of the combined computational and constrained linear inverse model. In other words for Patient 1, the inverse model is challenged 17 times, each time leaving out one of the corresponding points from the intraoperative deformation atlas [**M**] and the measured shift U. Error is then computed using only the omitted point, thereby resulting in 17 error measurements for each deformation atlas. Mean and maximum values of the % shift recaptured across these 17 error samples for all eight patients have been reported in the Table 8. Similar to Table 7 Atlas IV was used to compute the values reported in the table shown below.

Also, volumetric displacements predicted using the combined computational and linear inverse model were used to deform the patients' preoperative images. These images are then visually compared with the patient's postoperative image volume and the results have been presented in Figures 24 and 25. For the sake of brevity and clarity, only three patients (Patient 1, 7 and 8 reported in Table 1) have been shown in the figures. The first column in Figure 24 shows the preoperative MR slice, the second column shows the corresponding postoperative MR slice and the third column the deformed MR slice obtained using displacements predicted using the combined computational and linear inverse model. It should be noted that though the tumor was removed from the brain tissue when building the deformation atlases, tumor was not removed from the brain volume when the preoperative images

Patient #	Measured Surface Shift (mm)	Measured Sub-Surface Shift (mm)	Shift Error (mm)				Angular Error (deg)			
			Atlas I	Atlas II	Atlas III	Atlas IV	Atlas I	Atlas II	Atlas III	Atlas IV
1	8.2±2.2 (12.2)	2.6±1.6 (5.8)	0.6±0.5 (1.5)	0.7±0.4 (1.5)	0.7±0.4 (1.5)	0.4±0.4 (1.2)	8.4±1.3 (10.9)	8.4±1.3 (10.9)	9.4±1.6 (12.6)	8.1±1.3 (10.9)
2	9.2±1.3 (11.6)	4.0±1.2 (6.3)	0.8±0.4 (1.6)	0.6±0.5 (1.6)	0.6±0.4 (1.3)	0.6±0.4 (1.3)	9.6±1.2 (12.0)	9.4±2.2 (13.8)	9.6±1.2 (11.9)	9.6±1.2 (12.0)
3	8.8±1.9 (12.6)	3.7±0.9 (5.5)	0.7±0.5 (1.6)	0.8±0.4 (1.5)	0.8±0.3 (1.3)	0.4±0.4 (1.1)	10.4±2.0 (13.9)	10.1±2.2 (14.5)	10.1±2.2 (14.5)	10.4±2.0 (13.9)
4	5.4±0.9 (7.0)	2.6±1.6 (5.7)	0.6±0.5 (1.6)	0.7±0.5 (1.8)	0.7±0.5 (1.9)	0.4±0.4 (1.2)	9.6±1.2 (12.0)	8.4±1.3 (10.9)	8.4±1.3 (10.9)	8.1±1.3 (10.7)
5	10.6±2.4 (15.1)	3.1±1.6 (6.2)	0.8±0.3 (1.4)	0.9±0.3 (1.5)	0.6±0.3 (1.1)	0.4±0.4 (1.3)	11.4±1.3 (14.0)	11.2±1.8 (14.8)	11.2±1.8 (14.8)	11.4±1.3 (14.0)
6	5.3±0.8 (6.8)	2.4±1.3 (4.8)	0.8±0.4 (1.6)	0.6±0.5 (1.5)	0.6±0.5 (1.5)	0.4±0.3 (1.1)	9.4±2.2 (13.6)	10.1±2.2 (14.6)	9.6±1.2 (12.8)	9.4±2.2 (13.6)
7	9.4±1.1 (11.5)	3.2±1.4 (5.9)	0.5±0.3 (1.1)	0.6±0.4 (1.4)	0.6±0.3 (1.1)	0.5±0.3 (1.1)	9.5±2.3 (14.1)	8.9±2.5 (13.9)	8.9±2.5 (13.9)	9.5±2.3 (14.1)
8	5.3±0.9 (7.1)	2.6±1.6 (5.6)	0.6±0.5 (1.6)	0.7±0.5 (1.8)	0.6±0.4 (1.4)	0.4±0.4 (1.2)	9.5±2.3 (11.5)	10.1±2.2 (14.6)	9.6±1.2 (12.8)	9.4±2.2 (13.6)

Table 6: Measured surface and sub-surface shift, Shift Error and Angular Error for all five Patients using four different atlases. Mean±standard deviation (maximum) of the shift and error has been reported.

Patient #	% Shift Recapture	
	Mean	Minimum
1	85	79
2	85	79
3	89	80
4	85	79
5	87	79
6	83	77
7	84	81
8	85	79

Table 7: % shift recaptured with the constrained linear inverse model using Atlas IV

Patient #	% Shift Recapture	
	Mean	Minimum
1	87	81
2	85	80
3	90	82
4	85	78
5	88	81
6	82	79
7	85	82
8	84	79

Table 8: % shift recaptured using a "leave-one-out" approach with the combined computational and constrained linear inverse model using Atlas IV

were deformed using the predicted displacements.

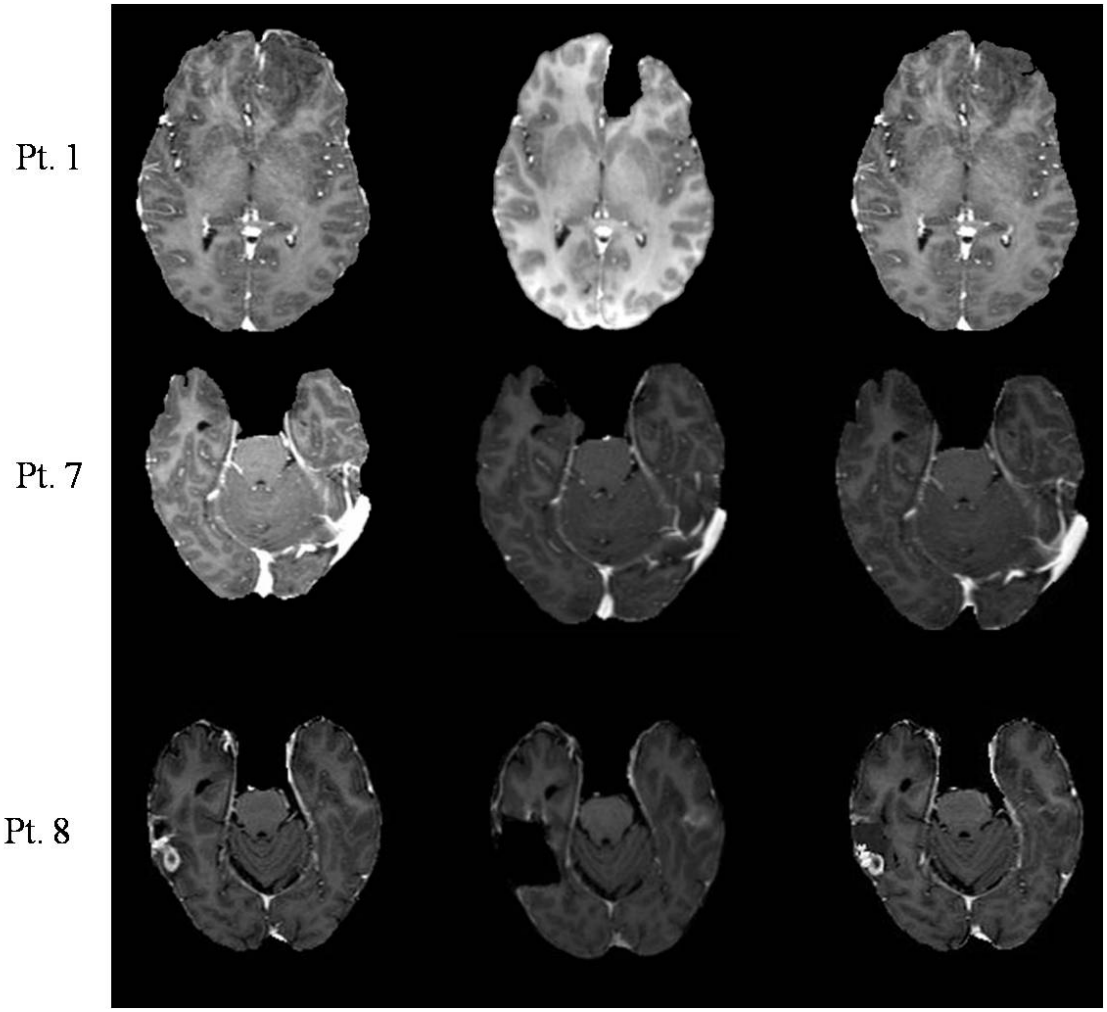

Figure 24: Model predictions for Patients 1, 7 and 8. First column shows a preoperative image slice for the patient, second column the corresponding postoperative image slice and the third column shows the image obtained using model predi ctions.

Figure 25 shows the fusion images for Patients 1, 7 and 8. The first column in the figure shows the fusion image obtained using the patients' preoperative image volume and the registered postoperative image volume. The amount of postoperative brain shift can be seen in these images. The second column in the figure shows the fusion image obtained using the postoperative image and the image predicted by the combined computational and linear inverse model. The amount of correction predicted by the model can be seen in these images.

Figure 26 shows the image updating results for a sub-surface point for Patients 1, 7

and 8. The first column shows a sub-surface point (represented as a black hollow circle) in the patient's preoperative image. The hollow black circle in the second column shows the position of the same point before brain shift and the solid black circle shows the true shifted position of the point. The white hollow circle in the second column shows the predicted shifted position of the point. For the sub-surface point shown in the figure, the model accounted for 81% of the measured shift for patient 1, 80% of the measured shift for patient 7 and 83% of the measured shift for patient 8.

Discussion

The results presented in this study demonstrate that the combined computational and linear inverse model is capable of predicting full volume displacements and can be used in a MUIGNS system. The framework reported here relies on predicting brain shift using a patient-specific atlas of model solutions that are consistent with the forces causing brain shift. This series of model solutions are then combined in a linear fashion using the sparse measured data. It should be noted that the deformation atlases are computed preoperatively and therefore significantly reduces the intraoperative computational time. Also, since the preoperative image volumes are acquired a day prior to surgery, the atlas of deformations can be computed a day prior to surgery using the parallelized computational model and the automatic boundary condition algorithm reported in [103].

Figure 25 demonstrates updating of preoperative images using displacements predicted by the combined computational and linear inverse model. In each of patient cases, the first column demonstrates a visible shift of the sub-surface structures and the second column demonstrates the shift correction predicted by the combined computational and linear inverse model. In all the eight cases presented, sub-surface points were chosen near the lateral ventricles and the tumor resection cavity to validate the sub-surface shift predicted by the model. Averaging over all the eight patient cases, the model recaptured 85% of the mean measured shift and 79% of the maximum measured shift. Also, a shift of 4-6mm of the tumor boundary and a shift of 3-6mm at the lateral ventricles was observed in the registration

studies and the model predictions. This is in agreement with the shift measurements reported in the literature [14, 107, 71]. Table 8 shows the % shift recaptured by the model, when the surface and sub-surface points were used to constrain the inverse model. As stated earlier, a "leave-one-out" approach was used to validate these shift predictions and these results suggest that the model performed slightly better when the inverse model was constrained using surface and sub-surface points. Averaging over all 8 patients, Table 8 shows that the model recaptured 86% of the mean measured shift and 80.3% of maximum measured shift. This is a marginal improvement over the results presented in Table 7.

Figure 27 shows the distribution of regression coefficients (α in Equation 22) for Patients 1, 7 and 8. Regression coefficients computed using the concatenated deformation atlas (Atlas IV reported in Section V) were used to generate the charts shown below. As stated earlier, Atlas IV consisted of a total of 501 model solutions(240 of the displacement solutions were modeled to simulated gravity-induced shift, 180 to model shift due to mannitol and 81 due to tissue swelling and mannitol combined). Averaging over all three patients, 40.5% of the non-zero regression coefficients belonged to gravity-induced shift, 40.6% to mannitol-induced shift and 5.3% to displacements modeled to simulate tissue swelling and mannitol. These findings suggest that gravity and mannitol-induced shift have an equal contribution in predicting the observed brain shift. We realize that these findings need to be validated in a bigger patient population before ascertaining the correlation between simulated boundary conditions and the observed brain shift. Nevertheless these results suggest that the atlas-based framework can be used to account for the complex loading conditions that occur during tumor resection therapies.

The method developed to produce updated MR images using displacements predicted by the finite element model was initially reported in [71]. This deformed image is based a porous media biomechanical model of the brain and is representative of the force environment causing brain shift. This is also a critical step in a MUIGNS system because it translates the deformation field into visual images that the neurosurgeons can relate to. We also developed a parallel algorithm to perform the image updating technique reported in [71] and using 16

processors it took less than a minute to deform a 256x256x180 MR image volume. With respect to tumor resection, tumor volume was identified from the patient's preoperative images and the entire tumor volume was removed from the model and the images produced using model displacements. In order for the model to produce image updates that mirror their intraoperative counterparts, the model has to account for the incremental removal of the tumor during surgery. This would require redigitization of the resection cavity as the surgery progresses, in order to accurately display the partial resection cavities in the image updates. In practice, this procedure is difficult to implement and might impede the surgical procedure. In order to circumvent this, we chose not to remove the tumor from the brain tissue during the image deformation procedure.

A few limitations of this study must be noted. First, we used the brain shift between preoperative and postoperative image volumes in this study. Since the postoperative MR image volumes were acquired a day after surgery, we understand that the shift used in this study is not representative of the intraoperative brain shift. Unfortunately, sub-surface intraoperative measurements were not available. The viscoelastic nature of the brain and the regeneration of CSF within the brain might have caused the brain to recover some of its intraoperative brain shift. Nevertheless, the results presented herein are encouraging and demonstrate that if the model were constrained with sparse intraoperative measurements the combined computational and linear inverse model framework can be used to predict introperative brain shift. Second, the model did not account for more direct interactions such as retractions and the brain tissue collapsing into the tumor resection cavity. It should be noted that retractors were not used in the cases reported in this work. However we hypothesize that surface loadings resulting from tissue retraction can be modeled in a forward manner as demonstrated in our previous work [73, 72].

Figure 28 shows the model predictions for Patient 2 reported herein. The first column represents the patient's preoperative image, second column shows the corresponding postoperative slice, third column the image predicted using the combined computational and linear inverse model. The fourth and fifth column shows the fusion images between the preoperative

and postoperative images, and the model predicted image and the preoperative image respectively. Though the model performed reasonably well in terms of shift recapture (the model recaptured 85% of the mean sub-surface shift for a measured sub-surface of 4.0±1.2mm), the fifth column in the figure shows that the image obtained using model predictions did not match well with the postoperative image. We observed normal brain tissue collapsing into the tumor resection cavity during surgery and hypothesize that a majority of the shift due to this collapse was not recovered when the postoperative images were obtained. Though this phenomenon was not observed in the other patient cases, we do realize its importance especially in terms of intraoperative brain shift and are working on enhancing the existing computational model to account for this surface collapse. Also, corresponding points could not be identified near the tumor resection margins and in the regions where the brain tissue collapsed and we do realize that shift predictions for this patient are incomplete.

Despite these model limitations, the computational time associated with running the inverse model and updating the preoperative images and the shift error analyses are encouraging and indicate that the linear inverse model reported herein combined with this parallel image updating technique is capable of predicting intraoperative brain shift in a real time fashion.

Conclusions

A framework to predict sub-surface shifts using a combined computational and linear inverse model has been utilized in a preliminary validation of our approach to brain shift correction. The framework reported relies on relatively inexpensive small scale computer clusters and can compute image updates on a time scale that is compatible with the surgical removal of tumor. The sub-surface error measurements and the qualitiative image comparisions presented in this work are encouraging. However the shift used in this study was based on postoperative images and we are currently working on relating the postoperative brain shift to the intraoperative brain shift and using the same work to validate the intraoperative brain shift predicted by the model. In addition we are working on enhancing the computa-

tional model to account for brain shift due to the tissue collapsing into the tumor resection cavity.

Acknowledgements

We thank the resident surgeons, the operating room staff and the radiology department at Vanderbilt University for their help in data collection. Most of the visualization algorithms were developed using Visualization Toolkit (http://www.vtk.org). Some segmentation and calculations were performed using Analyze AVW Version 6.0. This work was supported by the NIH-National Institute for Neurological Disorders and Stroke - Grant # R01 NS049251-01A1.

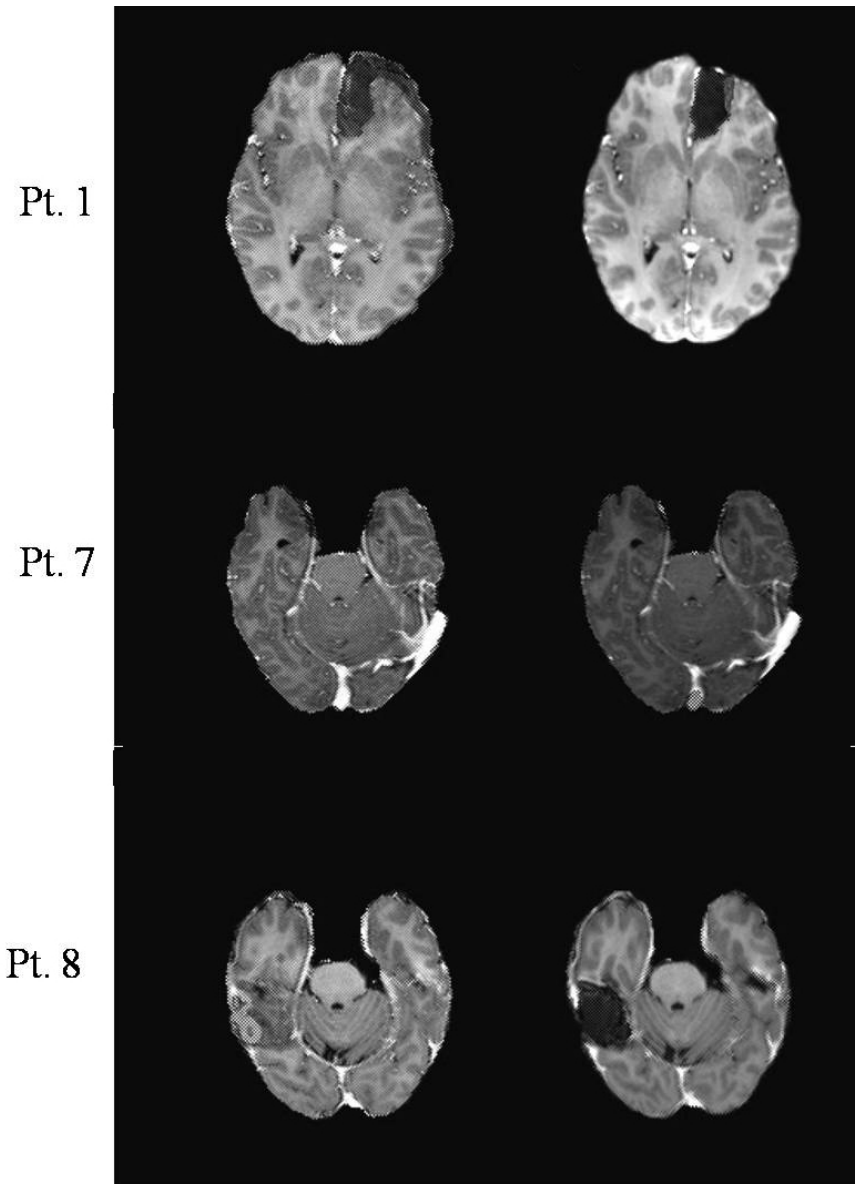

Figure 25: Fusion images for Patients 1, 7 and 8. Column 1: Fusion image between the patient's preoperative image and the postoperative image. This column shows the amount of brain shift. Column 2: Fusion image between the postoperative image and the image predicted using the combined computational and linear inverse model. This column shows the amount of shift correction predicted by the combined computational and linear inverse model.

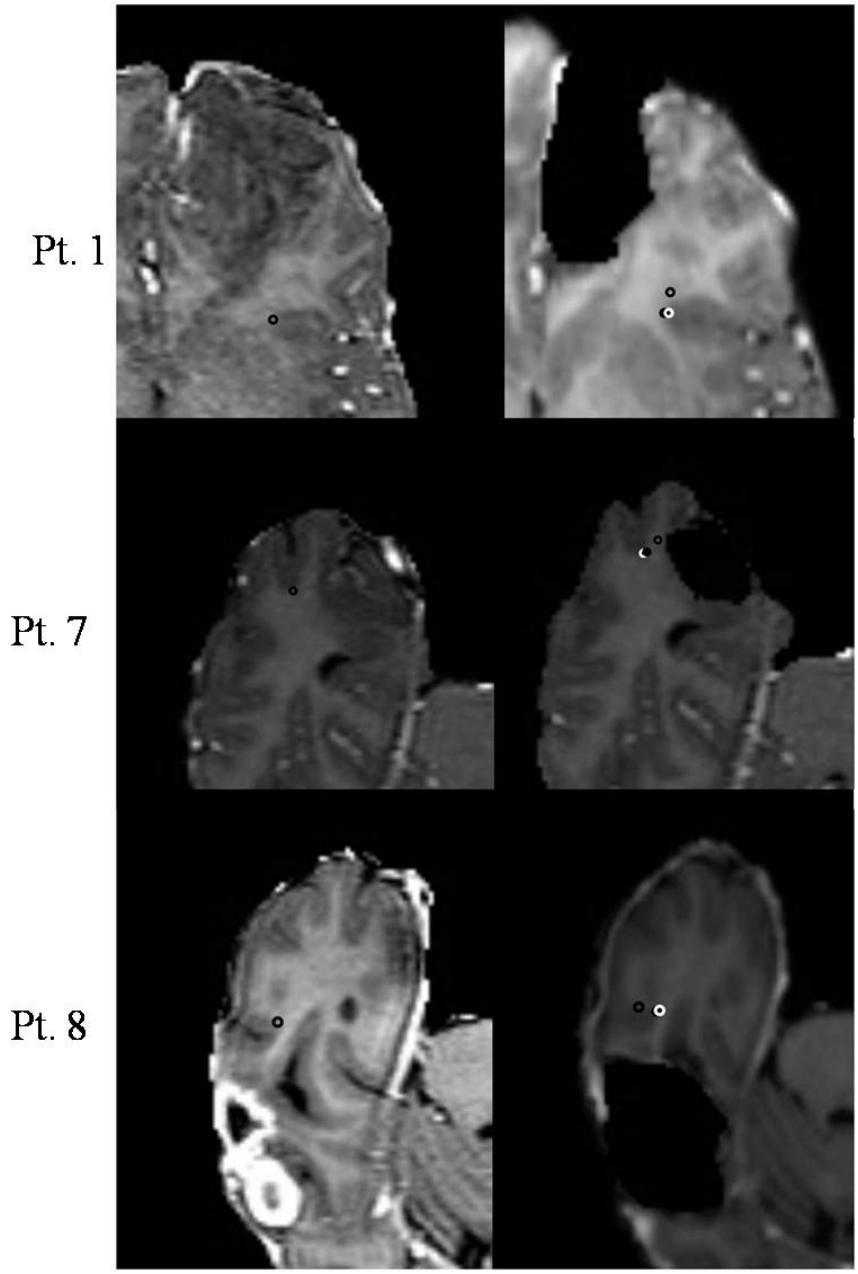

Figure 26: Fusion images for Patients 1, 7 and 8. Column 1: Fusion image between the patient's preoperative image and the postoperative image. This column shows the amount of brain shift. Column 2: Fusion image between the postoperative image and the image predicted using the combined computational and linear inverse model. This column shows the amount of shift correction predicted by the combined computational and linear inverse model.

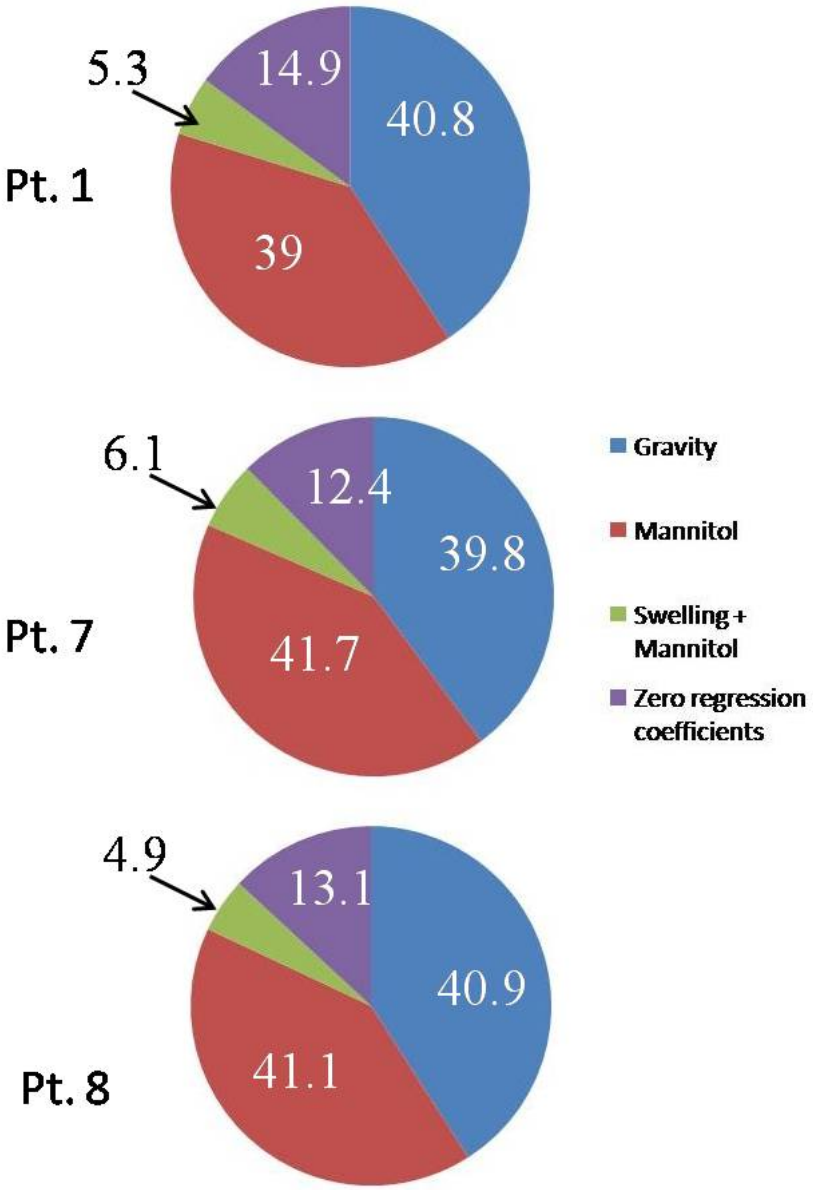

Figure 27: Distribution of non-zero regression coefficients for Patients 1, 7 and 8. Atlas IV (concatenated deformation atlas) was used to compute these distribution charts.

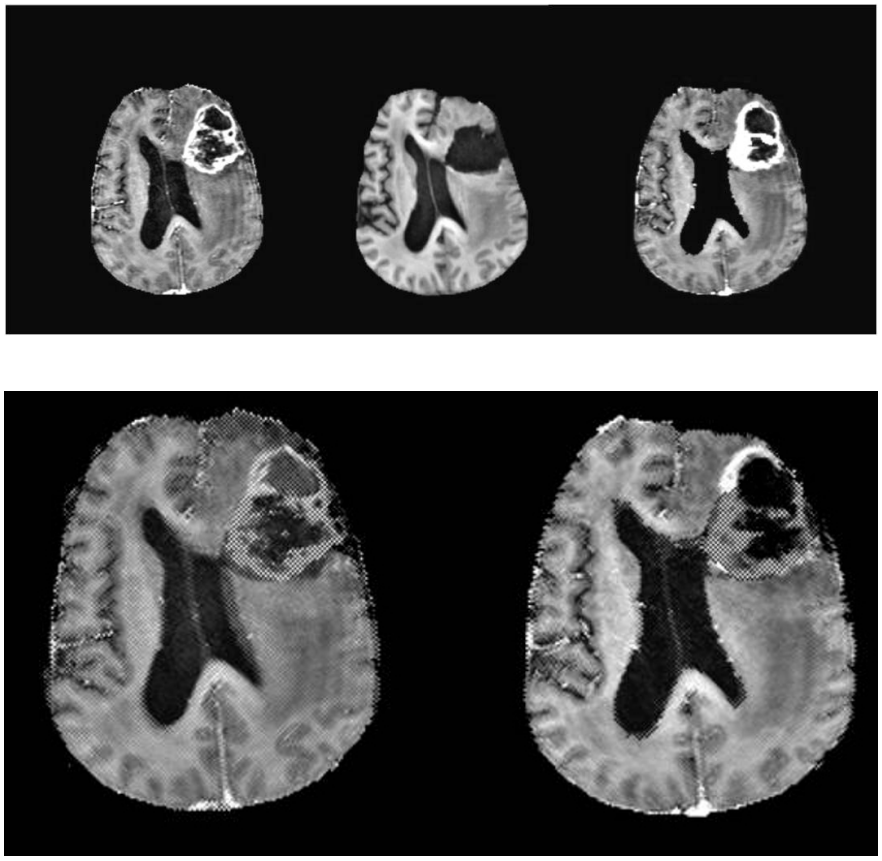

Figure 28: Model predictions for Patient 2. First row shows the model predictions for patient 2. Second row shows the fusion images. Row 1, Column 1: Preoperative image slice. Row 1, Column 2: Corresponding postoperative slice. Row 1, Column 3: Image obtained using model predicted displacements. Row 2, Column 1: Fusion image between preoperative and postoperative image. This column shows the amount of brain shift. Row 2, Column 5: Fusion image between the model predicted image and the postoperative image.

CHAPTER VI

SUMMARY

This work documents the development and quantification of an atlas-based framework to predict intraoperative brain shift using sparse data. Current image-guided systems assume that the brain is rigid and does not shift during surgery. However it has been shown the surface of the brain can deform upto a 1cm during tumor resection therapies. Model-updated image-guided systems correct for this shift and allow for accurate neuronavigation.

Typically, a patient-specific model is used in MUIGNS and the model is driven by intraoperative shift measured during surgery. The preoperative images are then deformed using the displacements predicted by the model thereby, producing images that mirror their intraoperative counterparts. Computational time associated with the model and the efficient integration of sparse intraoperative data are two important factors associated with any MUIGNS. The atlas-based model-updating framework proposed in this dissertation attemps to answer the above mentioned challenges by pre-computing a deformation atlas that accounts for all possible sources of intraoperative brain shift. Chapters III and IV present the development of the atlas-based framework. In this framework, a series of model deformations based on complex loading conditions such as brain shift due to gravity, volume changes due to drug reactions, tissue swelling due to edema is computed preoperatively and these model solutions are used to construct an atlas of deformations. This deformation atlas is then constrained using the measured sparse intraoperative data and volumetric brain shift is then calculated using an inverse model. The automatic boundary condition algorithm and the parallelized computational model presented in chapter IV faclitate the generation of deformation atlases on a reasonable time scale. Chapter V validates the framework using eight clinical cases.The parallel image-updating algorithm presented in this chapter completes the MUIGNS framework and demonstrates that the atlas-based framework is capable of meeting the real-time demands of neurosurgery.

Future work with respect to the work presented will include enhancements to the existing computational model to better account for falx cerebri and interhemispheric fissures in the brain. Senstivity studies also need to be performed to examine the sensitivity of the framework to the number of sparse measurement points and the number of model solutions used in the deformation atlas. Finally, more validation is required before using the proposed framework in a clinical setting.

REFERENCES

[1] T. K. Sinha. *Cortical Shift Characterization Using a Laser Range Scanner for Neurosurgery*. PhD thesis, Vanderbilt University, May 2005.

[2] T. K. Sinha, B. M. Dawant, V. Duay, D. M. Cash, R. J. Weil, and M. I Miga. A method to track cortical surface deformations using a laser range scanner. *IEEE Transactions on Medical Imaging*, 24(6):767–781, 2005.

[3] R. L. Galloway. The process and development of image-guided procedures. *Annual Review of Biomedical Engineering*, 3:83–108, 2001.

[4] P. L. Gildenberg. Stereotactic surgery - the past and the future. *Stereotactic and Functional Neurosurgery*, 70(2-4):57–70, 1998. STEREOTACT FUNCT NEUROSURG.

[5] R. L. Galloway and R. J. Maciunas. Stereotactic Neurosurgery. *Critical Reviews in Biomedical Engineering*, 18(3):207–233, 1990.

[6] D. W. Roberts, J. W. Strohbehn, J. F. Hatch, W. Murray, and H. Kettenberger. A frameless stereotaxic integration of computerized tomographic imaging and the operating microscope. *Journal of Neurosurgery*, 65(4):545–549, 1986.

[7] D. W. Roberts, A. Hartov, F. E. Kennedy, M. I. Miga, and K. D. Paulsen. Intraoperative brain shift and deformation: A quantitative analysis of cortical displacement in 28 cases. *Neurosurgery*, 43(4):749–758, 1998.

[8] C. Nimsky, O. Ganslandt, P. Hastreiter, and R. Fahlbusch. Intraoperative compensation for brain shift. *Surgical Neurology*, 56(6):357–364, 2001.

[9] A. Nabavi, P. M. Black, D. T. Gering, C. F. Westin, V. Mehta, R. S. Pergolizzi, M. Ferrant, S. K. Warfield, N. Hata, R. B. Schwartz, W. M. Wells, R. Kikinis, and F. A. Jolesz. Serial intraoperative magnetic resonance imaging of brain shift. *Neurosurgery*, 48(4):787–797, 2001.

[10] T. Hartkens, D. L. G. Hill, A. D. Castellano-Smith, D. J. Hawkes, C. R. Maurer, A. J. Martin, W. A. Hall, H. Liu, and C. L. Truwit. Measurement and analysis of brain deformation during neurosurgery. *IEEE Transactions on Medical Imaging*, 22(1):82–92, January 2003.

[11] H. J. Nauta. Error assessment during "image guided" and "imaging interactive" stereotactic surgery. *Computerized Medical Imaging and Graphics*, 18(4):279–87., 1994.

[12] D. L. G. Hill, C. R. Maurer, M.Y. Wang, R.J. Maciunas, J.A. Barwise, and J.M. Fitzpatrick. Estimation of intraoperative brain surface movement. *LNCS: CVRMED-MRCAS '97*, 1205:449–458, 1997.

[13] C. R. Maurer, D. L. G. Hill, R. J. Maciunas, J. A. Barwise, J. M. Fitzpatrick, and M. Y. Wang. Measurement of intraoperative brain surface deformation under a craniotomy. In *Medical Image Computing and Computer-Assisted Intervention - Miccai'98*, volume 1496 of *LECTURE NOTES IN COMPUTER SCIENCE*, pages 51–62. 1998.

[14] C. R. Maurer, D. L. G. Hill, A. J. Martin, H. Y. Liu, M. McCue, D. Rueckert, D. Lloret, W. A. Hall, R. E. Maxwell, D. J. Hawkes, and C. L. Truwit. Investigation of intraoperative brain deformation using a 1.5-t interventional mr system: Preliminary results. *IEEE Transactions on Medical Imaging*, 17(5):817–825, 1998.

[15] N. L. Dorward, O. Alberti, B. Velani, F. A. Gerritsen, W. F. J. Harkness, N. D. Kitchen, and D. G. T. Thomas. Postimaging brain distortion: magnitude, correlates, and impact on neuronavigation. *Journal of Neurosurgery*, 88(4):656–662, 1998.

[16] R. D. Bucholz, D. D. Yeh, J. Trobaugh, L. L. McDurmont, C. D. Sturm, C. Baumann, J. M. Henderson, A. Levy, and P. Kessman. The correction of stereotactic inaccuracy caused by brain shift using an intraoperative ultrasound device. In *LNCS: CVRMED-MRCAS '97*, volume 1205, pages 459–466. Springer-Verlag, 1997.

[17] P. J. Kelly, B. Kall, S. Goerss, and F. I. Earnest. Computer-assisted stereotaxic laser resection of intra-axial brain neoplasms. *Journal of Neurosurgery*, 64:427–439, 1986.

[18] S. J. Hassenbusch, J. S. Anderson, and P. K. Pillay. Brain tumor resection aided with markers placed using stereotaxis guided by magnetic resonance imaging and computed tomography. *Neurosurgery*, 28(6):801–805, 1991.

[19] M. N. Shalit, Y. Israeli, S. Matz, and M. L. Cohen. Intra-operative Computerized Axial Tomography. *Surgical Neurology*, 11:382–384, May 1979.

[20] L. D. Lunsford. A dedicated CT system for the stereotactic operating room. *Applied Neurophysiology*, 45:374–378, 1982.

[21] L. D. Lunsford, L. Leksell, and B. Jernberg. Probe holder for stereotactic surgery in the CT scanner. a technical note. *Acta Neurochirurgica*, 69(3-4):297–304, 1983.

[22] L. D. Lunsford and A. J. Martinez. Stereotactic exploration of the brain in the era of computed tomography. *Surgical Neurology*, 22(3):222–30., 1984.

[23] L. D. Lunsford. Intraoperative imaging of the brain. *Stereotactic Functional Neurosurgery*, 66(1-3):58–64, 1996.

[24] H. Okudera, K. Kobayashi, H. Gibo, T. Takemae, and K. Sugita. Development of the operating computerized tomographic scanner system for neurosurgery. *Acta Neurochirurgica (Wein)*, 111:61–63, 1991.

[25] W. E. Butler, C. M. Piaggio, C. Constantinou, L. Niklason, R. G. Gonzalez, G. R. Cosgrove, and N. T. Zervas. A mobile computed tomographic scanner with intraoperative and intensive care unit applications. *Neurosurgery*, 42(6):1304–1310, June 1998.

[26] P. McL. Black. Intraoperative computed tomographic scanning during transsphenoidal surgery: technical note. *Neurosurgery*, 32(6):1043, June 1993. Comment.

[27] J. F. Schenck, F. A. Jolesz, P. B. Roemer, H. E. Cline, W. E. Lorensen, R. Kikinis, S. G. Silverman, C. J. Hardy, W. D. Barber, E. T. Laskaris, and et al. Superconducting open-configuration MR imaging system for image-guided therapy. *Radiology*, 195:805–814, 1995.

[28] V. M. Tronnier, C. R. Wirtz, M. Knauth, G. Lenz, O. Pastyr, M. M. Bonsanto, F. K. Albert, R. Kuth, A. Staubert, W. Schlegel, K. Sartor, and S. Kunze. Intraoperative diagnostic and interventional magnetic resonance imaging in neurosurgery. *Neurosurgery*, 40(5):891–900, 1997.

[29] C. R. Wirtz, V. M. Tronnier, F. K. Albert, M. Knauth, M. M. Bonsanto, A. Staubert, O. Pastyr, and S. Kunze. Modified headholder and operating table for intra-operative mri in neurosurgery. *Neurol Res*, 20(7):658–61., 1998.

[30] M. Knauth, C. R. Wirtz, V. M. Tronnier, A. Staubert, S. Kunze, and K. Sartor. [intraoperative magnetic resonance tomography for control of extent of neurosurgical operations]. *Radiologe*, 38(3):218–24., 1998.

[31] V. Tronnier, A. Staubert, R. Wirtz, M. Knauth, M. Bonsanto, and S. Kunze. Mri-guided brain biopsies using a 0.2 tesla open magnet. *Minimally Invasive Neurosurgery*, 42(3):118–22., 1999.

[32] G. R. Sutherland, T. Kaibara, D. Louw, D. I. Hoult, B. Tomanek, and J. Saunders. A mobile high-field magnetic resonance system for neurosurgery. *J Neurosurg*, 91(5):804–13., 1999.

[33] C. R. Wirtz, M. Knauth, A. Staubert, M. M. Bonsanto, K. Sartor, S. Kunze, and V. M. Tronnier. Clinical evaluation and follow-up results for intraoperative magnetic resonance imaging in neurosurgery. *Neurosurgery*, 46(5):1112–1120, 2000.

[34] A. Nabavi, C. T. Mamisch, D. T. Gering, D. F. Kacher, R. S. Pergolizzi, W. M. Wells, R. Kikinis, P. M. Black, and F. A. Jolesz. Image-guided therapy and intraoperative mri in neurosurgery. *Minimally Invasive Therapy and Allied Technologies*, 9(3-4):277–286, 2000.

[35] Jr. Pergolizzi, R. S., A. Nabavi, R. B. Schwartz, L. Hsu, T. Z. Wong, C. Martin, P. M. Black, and F. A. Jolesz. Intra-operative mr guidance during trans-sphenoidal pituitary resection: preliminary results. *Journal of Magnetic Resonance Imaging*, 13(1):136–141, 2001.

[36] F. A. Jolesz, A. Nabavi, and R. Kikinis. Integration of interventional mri with computer-assisted surgery. *Journal of Magnetic Resonance Imaging*, 13(1):69–77., 2001.

[37] M. Hadani, R. Spiegelman, Z. Feldman, H. Berkenstadt, and Z. Ram. Novel, compact, intraoperative magnetic resonance imaging- guided system for conventional neurosurgical operating rooms. *Neurosurgery*, 48(4):799–807, 2001.

[38] G. R. Sutherland, T. Kaibara, C. Wallace, B. Tomanek, and M. Richter. Intraoperative assessment of aneurysm clipping using magnetic resonance angiography and diffusion-weighted imaging: Technical case report. *Neurosurgery*, 50(4):893–897, 2002.

[39] T. Kaibara, S. T. Myles, M. A. Lee, and G. R. Sutherland. Optimizing epilepsy surgery with intraoperative mr imaging. *Epilepsia*, 43(4):425–429, 2002.

[40] S.K. Warfield, F. Talos, A. Tei, A. Bharatha, A. Nabavi, M. Ferrant, P.M. Black, F. A. Jolesz, and R. Kikinis. Real-time registration of volumetric brain mri by biomechanical simulation of deformation during image guided neurosurgery. *Computing and Visualization in Science*, 5(1):3–11, 2002.

[41] R. M. Comeau, A. Fenster, and T. M. Peters. Intraoperative us in interactive image-guided neurosurgery. *Radiographics*, 18(4):1019–1027, 1998.

[42] D. G. Gobbi, R. M. Comeau, and T. M. Peters. Ultrasound/mri overlay with image warping for neurosurgery. In *LNCS: Medical Image Computing and Computer-Assisted Intervention: MICCAI '00*, volume 1935, pages 106–114. Springer-Verlag, 2000.

[43] R. M. Comeau, A. F. Sadikot, A. Fenster, and T. M. Peters. Intraoperative ultrasound for guidance and tissue shift correction in image-guided neurosurgery. *Medical Physics*, 27(4):787–800., 2000.

[44] A. Gronningsaeter, G. Unsgard, S. Ommedal, and B. A. J. Angelsen. Ultrasound-guided neurosurgery: A feasibility study in the 3-30 mhz frequency range. *British Journal of Neurosurgery*, 10(2):161–168, 1996.

[45] A. Gronningsaeter, T. Lie, A. Kleven, T. Morland, T. Lango, G. Unsgard, H. O. Myhre, and R. Marvik. Initial experience with stereoscopic visualization of three- dimensional ultrasound data in surgery. *Surgical Endoscopy-Ultrasound and Interventional Techniques*, 14(11):1074–1078, 2000.

[46] A. Gronningsaeter, A. Kleven, S. Ommedal, T. E. Aarseth, T. Lie, F. Lindseth, T. Lango, and G. Unsgard. Sonowand, an ultrasound-based neuronavigation system. *Neurosurgery*, 47(6):1373–1379, 2000.

[47] F. Lindseth, T. Lango, J. Bang, and T. A. N. Hernes. Accuracy Evaluation of a 3D Ultrasound-based Neuronavigation System. *Computer Assisted Surgery*, 7:197–222, 2002.

[48] G. Unsgaard, S. Ommedal, T. Muller, A. Gronningsaeter, and T. A. N. Hernes. Neuronavigation by intraoperative three-dimensional ultrasound: Initial experience during brain tumor resection. *Neurosurgery*, 50(4):804–812, 2002.

[49] L. M. Bates and R. A. Robb. Investigation of ultrasound image based correction ofintraoperative brain shift. In *Proceedings of the IEEE 2nd International Symposium on Bioinformatics and Bioengineering Conference*, pages 254–261. IEEE, 2001.

[50] D. W. Roberts, M. I. Miga, A. Hartov, S. Eisner, J. M. Lemery, F. E. Kennedy, and K. D. Paulsen. Intraoperatively updated neuroimaging using brain modeling and sparse data. *Neurosurgery*, 45(5):1199–1206, 1999.

[51] M. I. Miga. *Development and quantification of a 3D brain deformation model for model-updated image-guided stereotactic neurosurgery.* PhD thesis, Thayer school of Engineering, Dartmouth College, september 1998.

[52] A. Wittek, R. Kikinis, S.K. Warfield, and K. Miller. Brain shift computation using a fully nonlinear biomechanical model. *Lecture Notes in Computer Science*, pages 583–590, 2005.

[53] K. Miller. Constitutive model of brain tissue suitable for finite element analysis of surgical procedures. *Journal of Biomechanics*, 32(5):531–537, 1999.

[54] O. Skrinjar, A. Nabavi, and J. Duncan. Model-driven brain shift compensation. *Medical Image Analysis*, 6(4):361–373, December 2002.

[55] P. J. Edwards, D. L. Hill, J. A. Little, and D. J. Hawkes. A three-component deformation model for image-guided surgery. *Medical Image Analysis*, 2(4):355–67., 1998.

[56] A. Hagemann, K. Rohr, H. S. Stiehl, U. Spetzger, and J. M. Gilsbach. Biomechanical modeling of the human head for physically based, nonrigid image registration. *IEEE Transactions on Medical Imaging*, 18(10):875–84., 1999.

[57] M. Ferrant, A. Nabavi, B. Macq, F. A. Jolesz, R. Kikinis, and S. K. Warfield. Registration of 3-d intraoperative mr images of the brain using a finite-element biomechanical model. *IEEE Transactions on Medical Imaging*, 20(12):1384–1397, 2001.

[58] M. Bro-Nielsen. Fast finite elements for surgery simulation. *Stud.Health Technol.Inform.*, 39:395–400, 1997. UI - 97384280LA - engPT - Journal ArticleDA - 19970904IS - 0926-9630SB - TCY - NETHERLANDS.

[59] P.J. Edwards, D.L.G. Hill, J.A. Little, and D.J. Hawkes. Deformation for image guided interventions using a three component tissue model. *Med.Image Anal.*, 2(4):355–367, 1998.

[60] O. Skrinjar, D. Spencer, and J. Duncan. Brain shift modeling for use in neurosurgery. In *LNCS: Medical Image Computing and Computer-assisted Intervention: MICCAI '98*, volume 1496, pages 641–649. Springer-Verlag, 1998.

[61] O.M. Skrinjar and J.S. Duncan. Real time 3d brain shift compensation. *Information Processing in Medical Imaging, Proceedings*, 1613:42–55, 1999. Book in seriesBS60GLECT NOTE COMPUT SCI.

[62] C.A. Kemper. Incorporation of diffusion tensor mri in non-rigid registration for image-guided neurosurgery. Master's thesis, Harvard University, May 2003.

[63] K. Miller and K. Chinzei. Mechanical properties of brain tissue in tension. *Journal of Biomechanics*, 35(4):483–490, 2002.

[64] A. Wittek, K. Miller, R. Kikinis, and S.K. Warfield. Patient-specific model of brain deformation: Application to medical image registration. *Journal Of Biomechanics*, pages 919–929, 2006.

[65] K. Miller and K. Chinzei. Constitutive modelling of brain tissue: experiment and theory. *J.Biomech.*, 30(11-12):1115–1121, Nov 1997. UI - 98117495LA - engPT - Journal ArticleDA - 19980310IS - 0021-9290SB - IMCY - UNITED STATESJC - HJF.

[66] S. Hakim, J.G. Venegas, and J.D. Burton. The physics of the cranial cavity, hydrocephalus and normal pressure hydrocephalus: mechanical interpretation and mathematical model. *Surgical Neurology*, 5(3):187–210, 176.

[67] T. Doczi. Volume regulation of the brain tissue - a survey. *Acta Neurochir*, 121:1–8, 1993.

[68] M.A. Biot. General theory of three-dimensional consolidation. *J.Appl.Phys.*, 12:155–164, Feb 1941.

[69] T. Nagashima, T. Shirakuni, and I.S. Rapoport. A two-dimensional finite element analysis of vasogenic brain edema. *Neurol Med Chir*, 30:1–9, 1990.

[70] K. D. Paulsen, M. I. Miga, F. E. Kennedy, P. J. Hoopes, A. Hartov, and D. W. Roberts. A computational model for tracking subsurface tissue deformation during stereotactic neurosurgery. *IEEE Transactions on Biomedical Engineering*, 46(2):213–225, 1999.

[71] M. I. Miga, K. D. Paulsen, J. M. Lemery, S. D. Eisner, A. Hartov, F. E. Kennedy, and D. W. Roberts. Model-updated image guidance: Initial clinical experiences with gravity-induced brain deformation. *IEEE Transactions on Medical Imaging*, 18(10):866–874, 1999.

[72] L. A. Platenik, M. I. Miga, D.W. Roberts, K. E. Lunn, F. E. Kennedy, A. Hartov, and K. D. Paulsen. In vivo quantification of retraction deformation modeling for updated image-guidance during neurosurgery. *IEEE Transactions on Biomedical Engineering*, 49(8):823–835, August 2002.

[73] M. I. Miga, D. W. Roberts, F. E. Kennedy, L. A. Platenik, A. Hartov, K. E. Lunn, and K. D. Paulsen. Modeling of retraction and resection for intraoperative updating of images. *Neurosurgery*, 49(1):75–84, 2001.

[74] M. Ferrant, A. Nabavi, B. Macq, F. A. Jolesz, R. Kikinis, and S. K Warfield. Serial registration of intraoperative mr images of the brain. *Medical Image Analysis*, 6:337–359, 2002.

[75] K. E. Lunn, K. D. Paulsen, D. W. Roberts, F. E. Kennedy, A. Hartov, and L.A Platenik. Nonrigid brain registration: synthesizing full volume deformation fields from model basis solutions constrained by partial volume intraoperative data. *Computer Vision and Image Undestanding*, 89:299–317, 2003.

[76] K.E. Lunn, K.D. Paulsen, D. R. Lynch, D. W. Roberts, F. E. Kennedy, and A. Hartov. Assimilating intraoperative data with brain shift modeling using the adjoint equations. *Medical Image Analysis*, 9:281–293, 2005.

[77] C. Davatzikos, D. Shen, E. Mohamed, and Kyriacou. E. A framework for predictive modeling of anatomical deformations. *IEEE Transactions on Medical Imaging*, 20(8):836–843, 2001.

[78] D. L. G. Hill, C. R. Maurer, R. J. Maciunas, J. A. Barwise, J. M. Fitzpatrick, and M. Y. Wang. Measurement of intraoperative brain surface deformation under a craniotomy. *Neurosurgery*, 43(3):514–526, 1998.

[79] P. M. Black, T. Moriarty, E. Alexander, P. Stieg, E. J. Woodard, P. L. Gleason, C. H. Martin, R. Kikinis, R. B. Schwartz, and F. A. Jolesz. Development and implementation of intraoperative magnetic resonance imaging and its neurosurgical applications. *Neurosurgery*, 41(4):831–842, 1997.

[80] L. D. Lunsford, R. Parrish, and L. Albright. Intraoperative imaging with a therapeutic computed tomographic scanner. *Neurosurgery*, 15(4):559–61., 1984.

[81] M. I. Miga, T. K. Sinha, D. M. Cash, R. L. Galloway, and R. J. Weil. Cortical surface registration for image-guided neurosurgery using laser range scanning. *IEEE Transactions on Medical Imaging*, 22(8):973–985, August 2003.

[82] K. D. Paulsen, M. I. Miga, F. E. Kennedy, P. J. Hoopes, A. Hartov, and D. W. Roberts. A computational model for tracking subsurface tissue deformation during stereotactic neurosurgery. *Ieee Transactions on Biomedical Engineering*, 46(2):213–225, 1999.

[83] M. J. Letteboer, P.W.A Willems, M. A. Viergever, and W. J. Niessen. Brain shift estimation in image-guided neurosurgery using 3-d ultrasound. *IEEE Transcations on Biomedical Engineering*, 52(2):268–276, 2005.

[84] M. I. Miga, K. D. Paulsen, P. J. Hoopes, F. E. Kennedy, A. Hartov, and D. W. Roberts. In vivo quantification of a homogeneous brain deformation model for updating preoperative images during surgery. *IEEE Transactions on Biomedical Engineering*, 47(2):266–273, 2000.

[85] M. Miga, K. Paulsen, F. Kennedy, J. Hoopes, A. Hartov, and D. Roberts. Initial in-vivo analysis of 3d heterogeneous brain computations for model-updated image-guided neurosurgery. In *Medical Image Computing and Computer-Assisted Intervention - Miccai'98*, volume 1496 of *LECTURE NOTES IN COMPUTER SCIENCE*, pages 743–752. 1998.

[86] K. E. Lunn, A. Hartov, E. Hansen, H. Sun, D. Roberts, and K. Paulsen. A quantitative comparision of edges in 3d intraoperative ultrasound and preoperative mr images of the brain. *Lecture Notes in Computer Science: Medical Image Computing and Computer-Assisted Intervention*, 2208:1081–1090, 2001.

[87] H. Sun, H. Farid, K. Rick, A. Hartov, D. W. Roberts, and K. D. Paulsen. Estimating cortical surface motion using steropsis for brain deformation models. In *LNCS: Medical Image Computing and Computer Assisted Intervention: MICCAI '03*, volume 2878, pages 794–801. Springer-Verlag, 2003.

[88] H. Sun, D. W. Roberts, , H. Farid, Z. Wu, A. Hartov, and K. D. Paulsen. Cortical surface tracking using a stereoscopic operating microscope. *Neurosurgery*, 56-1:86–97, 2005.

[89] P Dumpuri, R.C Chen, and M.I Miga. Model updated image guidance: A statistical approach to Gravity Induced Brain Shift. *Lecture Notes in Computer Science: Medical Image Computing and Computer-Assisted Intervention*, 2879(1):375–382, 2003.

[90] T. K. Sinha, R.J. Weil, D. M. Cash, R. L. Galloway, and M. I. Miga. Intraoperative cortical surface characterization using laser range scanning: Preliminary results. *Neurosurgery*, 2005. Submitted.

[91] H. J. Reulen, R. Graham, and I. Klatzo. Role of pressure gradients and bulk flow in dynamics of vasogenic brain edema. *J. Neurosurgery*, 46:24–35, 1977.

[92] M. Miga, K. Paulsen, F. Kennedy, A. Hartov, and D. Roberts. Model-updated image-guided neurosurgery using the finite element method: Incorporation of the falx cerebri. In Taylor and Colchester, editor, *Lecture Notes in Computer Science for 2nd International Conference on Medical Image Computing and Computer-Assisted Intervention*, volume 1679, pages 900–909. Springer Verlag, New York, 1999.

[93] M. I. Miga, K. D. Paulsen, P. J. Hoopes, F. E. Kennedy, A. Hartov, and D. W. Roberts. In vivo modeling of interstitial pressure in the brain under surgical load using finite elements. *Journal of Biomechanical Engineering-Transactions of the Asme*, 122(4):354–363, 2000.

[94] Satish Balay, Kris Buschelman, William D. Gropp, Dinesh Kaushik, Matthew G. Knepley, Lois Curfman McInnes, Barry F. Smith, and Hong Zhang. Petsc web page, 2001. http://www.mcs.anl.gov/petsc.

[95] Satish Balay, Kris Buschelman, Victor Eijkhout, William D. Gropp, Dinesh Kaushik, Matthew G. Knepley, Lois Curfman McInnes, Barry F. Smith, and Hong Zhang. Petsc users manual. Technical Report ANL-95/11 - Revision 2.3.0, Argonne National Laboratory, 2004.

[96] Satish Balay, Victor Eijkhout, William D. Gropp, Lois Curfman McInnes, and Barry F. Smith. Efficient management of parallelism in object oriented numerical software libraries. In E. Arge, A. M. Bruaset, and H. P. Langtangen, editors, *Modern Software Tools in Scientific Computing*, pages 163–202. Birkha user Press, 1997.

[97] D. R. Lynch. *Numerical Partial Differential Equations for Environmental Scientists and Engineers*. Springer, 2nd edition, 2004.

[98] W.E. Lorensen and H.E. Cline. Marching cubes: A high resolution 3d surface construction algorithm. *ACM Computer Graphics*, 21(4):163–169, Jul 1987.

[99] J.M. Sullivan, G. Charron, and K.D. Paulsen. A three-dimensional mesh generator for arbitrary multiple material domains. *Finite Elements in Analysis and Design*, 25(3-4):219–241, 1997. JournalAPR 17WW939FINITE ELEM ANAL DESIGN.

[100] C. Nimsky, O. Ganslandt, S. Cerny, P. Hastreiter, G. Greiner, and R. Fahlbusch. Quantification of, visualization of, and compensation for brain shift using intraoperative magnetic resonance imaging. *Neurosurgery*, 47(5):1070–1079, 2000.

[101] M. I. Miga, J. M. Fitzpatrick, R. L. Galloway Jr., and K. D. Paulsen. Incorporation of surface-based deformations for updating images intraoperatively. *Medical Imaging 2001: Visualization, Display, and Image-guided Procedures*, 2(24):169–178, 2001.

[102] G. J. Rubino, C. Lycette1, K. Farahani, D. McGill, B. Van de Wiele, and J. P. Villablanca. Interventional magnetic resonance imaging guided neurosurgery - the ucla experience with the first 100 cases. Technical Report ElectoMedica Neuro, Siemens HealthCare Systems, 2000.

[103] P Dumpuri, R.C Thompson, B.M. Dawant, A. Cao, and M.I Miga. An atlas-based method to compensate for brain shift: Preliminary results. *Medical Image Analysis*, 11(2):128–145, 2006.

[104] M. I. Miga, D. W. Roberts, A. Hartov, S. Eisner, J. Lemery, F. E. Kennedy, and K. D. Paulsen. Updated neuroimaging using intraoperative brain modeling and sparse data. *Stereotactic and Functional Neurosurgery*, 72(2-4):103–106, 1999. Times Cited: 0 Cited Reference Count: 12 Cited References: DORWARD NL, 1998, J NEUROSURG, V88, P656 HILL DLG, 1998, NEUROSURGERY, V43, P514 KHALIL TB, 1977, J BIOMECH, V10, P119 MIGA M, 1998, LECT NOTES COMPUT SC, V1496, P743 MIGA MI, 1998, INT J NUMER METH ENG, V43, P955 NAGASHIMA T, 1990, NEUROL MED CHIR, V30, P1 NAGATSU T, 1993, ADV NEUROL, V60, P165 PAULSEN KD, 1999, IEEE T BIO-MED ENG, V46, P213 ROBERTS DW, IN PRESS NEUROSURGER ROBERTS DW, 1998, NEUROSURGERY, V43, P749 SULLIVAN JM, 1997, FINITE ELEM ANAL DES, V25, P219 WARD CC, 1975, P 19 STAPP CAR CRASH, P641 1 311RA STEREOTACT FUNCT NEUROSURG.

[105] R. Li. Automatic placement of regions of interest in medical images using image registration. Master's thesis, Vanderbilt University, May 2001.

[106] B. M. Dawant, S. L. Hartmann, J. P. Thirion, F. Maes, D. Vandermeulen, and P. Demaerel. Automatic 3-d segmentation of internal structures of the head in mr images using a combination of similarity and free-form transformations: Part i, methodology and validation on normal subjects. *Ieee Transactions on Medical Imaging*, 18(10):909–916, 1999. English OCT IEEE TRANS MED IMAGING.

[107] H. K. Dickhaus, K. Ganser, A. Staubert, M. M. Bonsanto, C. R. Wirtz, V. M. Tronnier, and S. Kunze. Quantification of brain shift effects by mr-imaging. *Proc. 19th An. Int. Conf. IEEE Eng. Med. Biol. Soc.*, 2:491–494, 1997.